Universitá degli Studi di Napoli "Federico II"

Facoltá di Scienze Matematiche, Fisiche e Naturali

Corso di Laurea in Fisica

Anno Accademico 2015/2016

Tesi di Laurea Specialistica

The Semiconductor Multiplication System for Photoelectrons in a Vacuum Silicon Photomultiplier Tube (VSiPMT) and Related Front End Electronics

Relatore:
Prof. Giancarlo Barbarino
Dr. Felicia Barbato

Candidato:
Elisabetta Nocerino
Matricola:
N94/257

A nonna Maria

Contents

Introduction

Photon detection is a key factor to study many physical processes in several areas of fundamental physics research (i.e. particle and astroparticle physics, biomedicine, nuclear physics), industrial applications (i.e. medical equipment, environmental measurement equipment, quantum computing), medical equipment and check-ups (i.e. PET, Radioimmunoassay and Enzyme immunoassay as luminescent, fluorescent, Chemiluminescent Immunoassay) and any other business (Fiberoptics communication, Remote sensing for security and safety, Environmental sensing for pollution detection, Defence). This impressive range of applications requires an equally impressive amount of detectors that can fulfill the various requirements that are best suited to the specific case.
In this thesis we will focus on Astroparticle Physics applications. Astroparticle Physics is a relatively new field of research emerging at the intersection of particle physics, astronomy, and cosmology. It aims to answer fundamental questions related to the story of the Universe such as: What is the Universe made of? What is the origin of cosmic rays? What is the nature of gravity? Et similia.
To answer these questions, physicists are developing experiments to detect, track, and/or identify messengers from the Universe by means of various photoetectors.
The detection of low levels of light became possible almost one century ago when in the year 1913 Elster and Geiter invented the photoelectric tube only few years after Einstein formulated 1905 the photoelectric workfunction [1]. It took more than 20 years until the first photomultiplier tube (PMT) was invented in the RCA laboratories and became in 1936 a commercial product. Single photons were detectable from that moment on. Further innovations have led to highly sophisticated devices available nowadays.
PMTs have two severe handicaps: they don't allow the photon counting and the complicated mechanical structure inside the vacuum container dissipates a lot of power. This forced to search for an alternative to PMTs. A very succeseful alternative is provided by solid state silicon-based photodetectors: PIN, APD and SiPM. These three devices are still currently used in many big experiments for high-energy physics (CLEO, L3, BELLE, BABAR, GLAST).
PIN photodiodes take their name from the description of the internal structure of

the silicon, actually it stands for ”p-intrinsic-n”. PIN photodiodes anyway are not really suitable for very low level light detection. This devices indeed have no internal gain, so for each photon trigger only one electron-hole pair is generated. Since their internal noise corresponds to several hundreds electrons, a higher number of photon per pulse is necessary in order to be detectable.
The Avalanche PhotoDiodes (APDs), used in big experiments like CMS, are an improvement with respect to the PIN since they have an internal gain. This feature allows a better signal to noise ratio. Anyway in this configuration, the internal gain is low (50 ÷ 100 magnification factor) and at least 20 incoming photons per pulse are necessary in order to easily detect the signal [2].
At the beginning of this millennium the Geiger-mode avalanche photodiode (G-APD) has been developed. This device can detect single photons with a resolution which is impossible to reach for a PMT and therefore some people call it Silicon PhotoMultiplier, SiPM. The pulse height spectrum measured with a G-APD shows a very good resolution, so even the single photon can be detected.
This thesis is focused on the study and characterization of various SiPM families in the wider context of the development of new scientific instrumentation for future missions of exploration and observation of the universe: the VSiPMT[1], an original design for an innovative light detector invented in Naples to enlarge indirectly the SiPM sensitive surface and to overcome PMTs limits.
It consists of two parts:

- Motivations and Background: as the title suggests, this part contains the current detector's technology state of art and the motivations behind the necessity of new instrumentations for astroparticle physics, notions about Semiconductor Physics, the theoretical background behind the SiPM's operation priciple and a description of the VSiPMT.

- Measurements and Data Analysis: this part contains a detailed description of all the measurements made for the characterization of the SiPMs and their results, the temperature issue and the proposed solution, a full characterization of the latest VSiPMT prototype manufactured by Hamamatsu Photonics, a world leader company in photodetector manufacturing.

[1]Acronym for Vacuum Silicon PhotoMultiplier Tube

Part I

Motivations and Background

Chapter 1

On the Traditional Photodetectors and Their Limits

There are several mechanisms of interaction between particles and matter. On these processes is based the operating principle of photodetectors. According to it, the energy lost by particles in interaction with matter is converted into electrical signals, that are used to get informations about the interacting particle.
Since in this thesis we are going to present an alternative to the standard photodetectors, we are interested in those phenomena related to light emission such as Cherenkov[1] effect, Air Fluorescence[2] and Scintillation[3], so the structure of a PMT or a hybrid detector consists of two primary elements:

- a medium in which takes place the excitation of the molecules and atoms that produces photons;
- the photodetector which, in general, consists of two sections:
  - a photocathode, constituted by a photosensitive material that converts the photons produced by the scintillator into photoelectrons by means of photoelectric effect;
  - an electron multiplier (fig. 1.1).

[1]Cherenkov radiation looks like a very short flash ($5 \div 20$ ns) generated by the cascade of relativistic charged particles (shower) produced when a very high-energy gamma ray strikes the atmosphere.

[2]The passage of charged particles in an extensive air shower through the atmosphere results in the ionization and excitation of the gas molecules (mostly nitrogen). Some of this excitation energy is emitted in the form of visible and UV radiation.

[3]A scintillator is a material that exhibits scintillation, the property of luminescence, when excited by ionizing radiation. Luminescent materials, when struck by an incoming particle, absorb its energy and re-emit the absorbed energy in the form of light (i.e. scintillate).

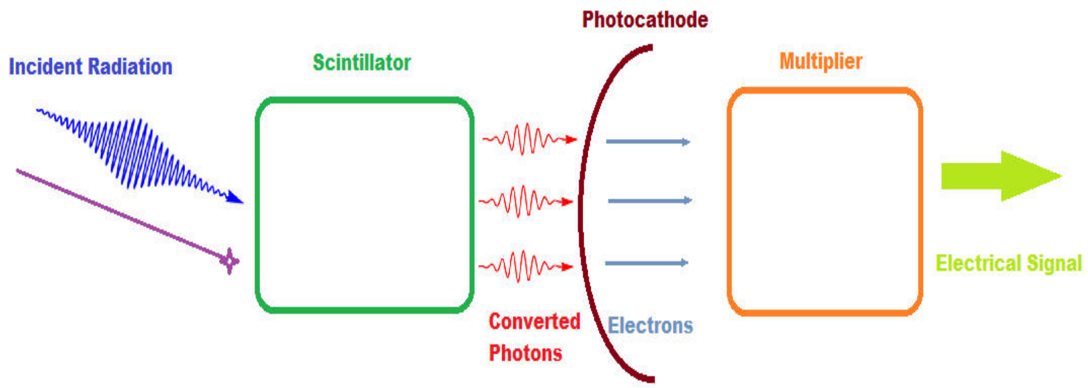

Figure 1.1: Schematic view of a Photodetector

The medium referred above can be a scintillator or also atmosphere, huge volumes of water, ice or liquefied gas, even at cryogenic temperatures. The passage of a charged particle causes the excitation of the atoms of the medium that, then, emit photons by de-excitation.
By reading a detection volume with a photodetector, an electrical signal is produced proportional to the amount of light received. This allows to obtain an estimate of the number of particles that have passed through the detector.
This photomultiplier is the key active element of the detector, since it converts photons into electrical signals that can be interpreted; consequently the current technological development is focused on it, especially in terms of linearity, gain and sensitivity (quantum efficiency and response to individual photoelectrons). The mostly used categories of photodetectors in the field of Astroparticle Physics are: the vacuum tubes, the hybrid photodetectors and the solid state photodetectors.

1.1 Vacuum Tubes (PMTs)

Vacuum Photomultiplier Tubes (VPMT) are currently the most used detectors. They are typically constructed with an evacuated glass housing, containing a photocathode, several dynodes, and an anode. Incident photons strike the photocathode material, which is usually a thin vapor-deposited conducting layer on the inside of the entry window of the device. Electrons are ejected from the surface as a consequence of the photoelectric effect. These electrons are directed by the focusing electrode toward the electron multiplier, where electrons are multiplied by the process of secondary emission.
The electron multiplier consists of a number of electrodes called dynodes (fig. 1.2).

Each dynode is held at a more positive potential than the preceding one. A primary electron leaves the photocathode with the energy of the incoming photon minus the work function of the photocathode. A small group of primary electrons is created by the arrival of a number of initial photons that is proportional to the energy of the incident radiation. The primary electrons move toward the first dynode because they are accelerated by the electric field. They each arrive with a kinetic energy imparted by the potential difference. Upon striking the first dynode, more low energy electrons are emitted, and these electrons are in turn accelerated toward the second dynode and so on ... The geometry of the dynode chain is such that a cascade occurs with an exponentially-increasing number of electrons being produced at each stage (the amplification factor is between 10^5 and 10^7). This large number of electrons reaching the anode results in a sharp current pulse that is easily detectable.

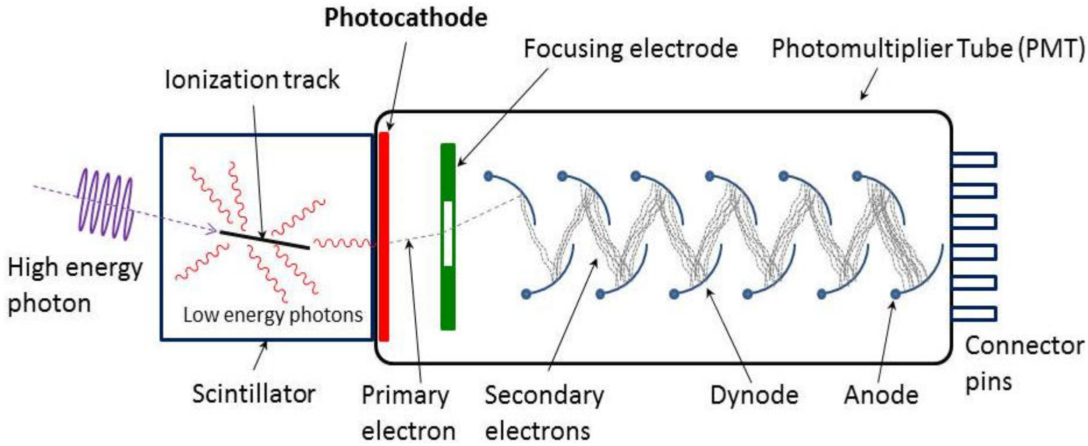

Figure 1.2: Schematic view of a VPMT

The necessary distribution of voltage along the series of dynodes is created by a voltage divider chain (fig. 1.3). The photocathode is held at a negative high voltage, while the anode is very close to ground potential. The capacitors across the final few dynodes act as local reservoirs of charge to help maintain the voltage stable on the dynodes while electron avalanches propagate through the tube.
VPMT presents many good features like the ability to detect low light, high gain, low noise, high frequency response and large area of collection. However it also has several limits:

- the multiplication of electrons on the first dynode is affected by fluctuations that make difficult the single photon counting;

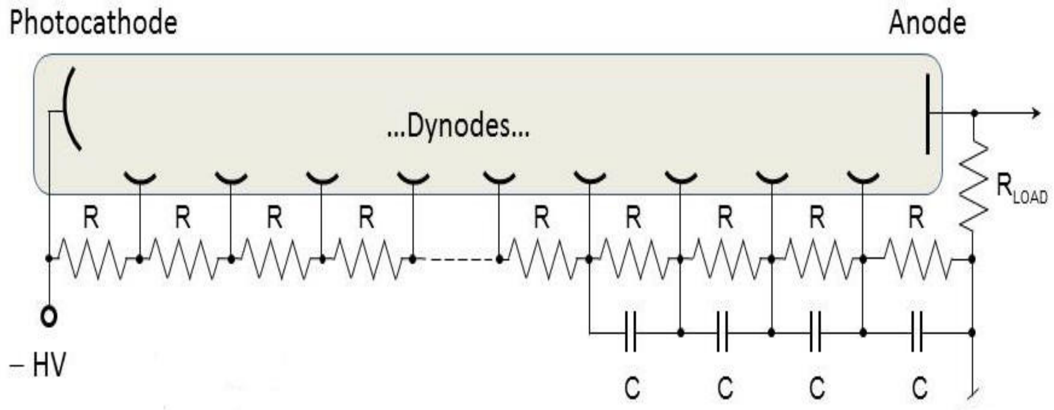

Figure 1.3: Illustrative design of the voltage divider chain of a VPMT

- gain is inversely proportional to linearity[4] because of the space charge distribution on the dinodes, therefore linearity decreases with increasing gain; furthermore linearity of signals is affected by several factors related to the structure of the device such as power supply stability, the divider current and the cathode resistivity;
- also the time response is affected by significant fluctuations and it is not very fast ($\sim$ ns) because of the transit time of electrons through the tube that has a spread depending on structural features of the device such as the number of dynodes, the photocathode diameter and the overall voltage;
- its sensitivity to magnetic fields limits its range of applications;
- the mechanical structure of dynodes is extremely complex as well as expensive;
- it is inefficient in terms of power consumption, since it requires a HV supply on the cathode ($\sim$ kV) and a PD between one dinode and the next which, moreover, must be calibrated very carefully because it could prejudice the correct operation of the detector;
- it presents a bad operation at cryogenic temperatures;

[4]Proportionality between the early amount of photoelectrons generated by the incident flux of photons and the final flux reached by the cathode.

- there are many sources of noise that can affect the signal and lead to the generation of dark currents and afterpulses: thermionic emission from photocathode and dynodes, ohmic leakage between the anode and other electrodes inside the tube, photocurrent produced by scintillation from glass envelope, field emission current, ionization current from residual gases, radiation from radioisotopes contained in the glass envelope, cosmic rays and environmental gamma rays.

In order to overcome the problems linked to the dynode chain, research for new photomultipliers were focused on the use of semiconductors in recent years. The progress of these devices has led to the use of reverse p-n junctions to realize solid state detectors and, then, to the developement of hybrid photomultipliers.

1.2 Solid-State Photodetectors

A considerable alternative to PMTs are the solid-state photodetectors, a new constantly developing technology. These devices differ from the vacuum tubes because of the working principle. In this case, the amplification mechanism occurs within a solid-state (semiconductor) material, rather than in a vacuum tube [3, 4, 37]. Currently the most used are APDs, avalanche photodiodes, P-I-N photodiodes, and the SiPMs, Silicon PhotoMultipliers.
Solid-state detectors deserve a separate discussion. Before going into details of the key topics of this thesis we believe it is appropriate to introduce some basic notions about Semiconductor Physics, since it is the necessary theoretical basis for understanding the fundamental mechanisms that determine the operating priciples of the devices of our interest.

1.3 PN Junctions: a Bit of Semiconductor Physics

The ability to conduct current of a material is quantified by its electrical conductivity σ $[\Omega^{-1} \cdot cm^{-1}]$ (or its resistivity ρ $[\Omega \cdot cm]$, which identifies the inattidudine to conduct). The conductors have low ρ ($10^{-6} \div 10^{-5}[\Omega \cdot cm]$ for silver, copper and aluminum), the insulators have high ρ (glass has $\rho = 10^{10}$, diamond $\rho = 10^{14}$, sulfur even $\rho = 10^{17}$ $[\Omega \cdot cm]$).
In electronic application there is need for materials having a behavior not so well defined, but ductile and versatile. This is due to the fact that the electronic devices must be able to allow the current flow in certain conditions, inhibiting it in other and modulate it when necessary.
A wide range of materials exist, characterized by intermediate values of ρ, called semiconductors. In particular, we consider silicon (Si), a material which has an

interesting property: its resistivity can be changed ad hoc (even significantly) in a controlled manner [5].
A semiconductor in which other atomic species (dopant or impurities) have been introduced ad hoc is called extrinsic or doped. Otherwise is called intrinsic or undoped. The intrinsic silicon can be considered almost an insulator; its resistivity is equal to about 2.5 x $10^5[\Omega \cdot cm]$ at T = 300 K. This is related to the fact that in a cm^3 of material contains only 1.45 x 10^{10} free electrons and holes[5], versus 5 x 10^{22} atoms. In electronics is adopted extrinsic silicon, doped with boron (B), arsenic (As), phosphorus (P) and antimony (Sb).
Silicon is the most widely used material in the production of semiconductor devices. It proceeds from silica, an extremely common material (in nature it is found in sand, quartz, clay); indeed it constitutes 25% of the earth's crust. It has a very good attitude to the formation of surface layers of silicon dioxide (SiO_2), which serves for several uses such as the selective introduction of dopant, the thin oxide gate realization in MOS transistors and circuit protection. The fabrication of silicon wafers is a standardized process, even for large diameters (20 cm).
No other semiconductor material enjoys these properties.
Silicon belongs to the group IV of the Periodic Table of Elements, so Si atom is tetravalent. It has 4 valence electrons in the outhermost atom's energy shell (n = 3), to form covalent bonds with adjacent atoms in the lattice. Its electron configuration is the following:

$$1s^2 2s^2 2p^6 3s^2 3p^2 \tag{1.1}$$

1.3.1 Electronic Band Structure

The electrons of a single, isolated atom occupy atomic orbitals. Each orbital forms at a discrete energy level. When multiple atoms join together to form into a molecule, their atomic orbitals combine to form molecular orbitals, each of which forms at a discrete energy level. As more atoms are brought together, the molecular orbitals extend larger and larger, and the energy levels of the molecule will become increasingly dense [7]. Eventually, the collection of atoms form a solid where the energy levels are so close that they can be considered to form a continuum called a **band**.
In the crystal lattice of the silicon, where the grating period is 5.43 $\mathring{A}$, we have two energy bands, each of which characterized by N levels energy and 4 x N quantum states. The lower band is called the valence band; in it the 4 x N quantum states are all allocated by electrons. The upper band is called the conduction band; in it 4 x N quantum states are all empty (fig. 1.4). The middle range is called bandgap,

[5] Negative and positive charge carriers

because the corresponding energy levels do not exhibit quantum states allocable by electrons, and has amplitude E_G.

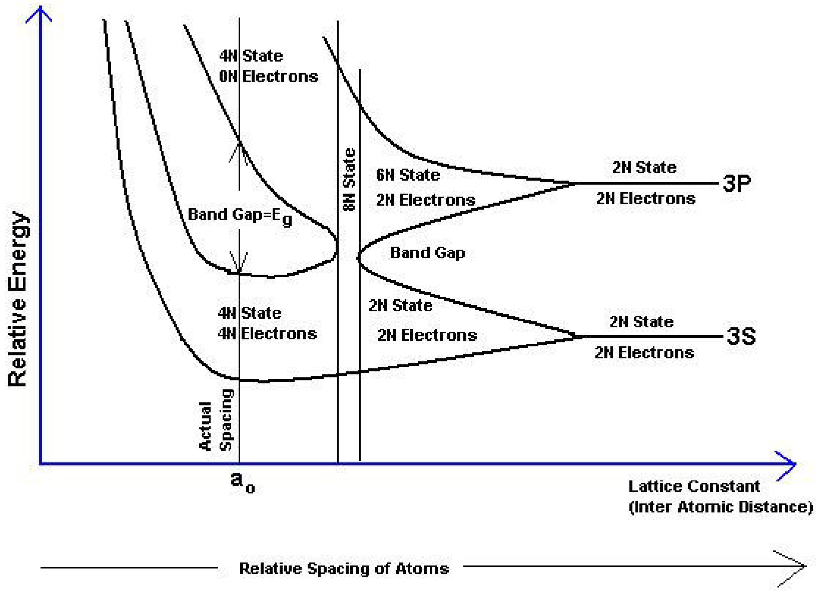

Figure 1.4: Si energy band diagram

Figure 1.5 (left) depicts the 2-D representation of the covalent bonds between the silicon atoms in the crystal lattice.

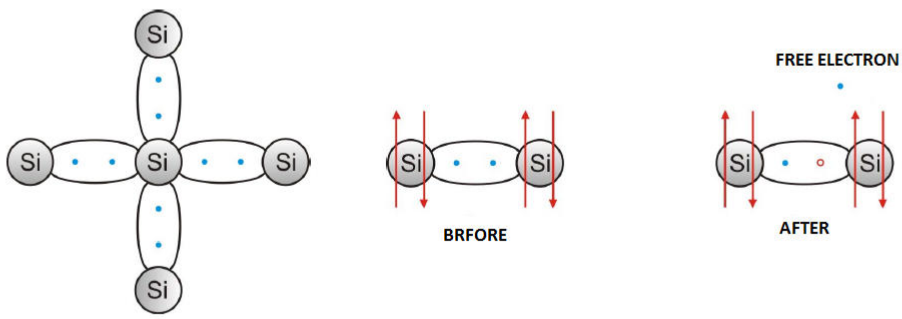

Figure 1.5: 2-D model of a silicon crystal lattice (left). Release of the electron from the covalent bond (right)

At temperatures T → 0 K, atoms are fixed in their lattice positions and valence electrons are all involved in covalent bonds between 2 silicon atoms, and cannot take part in the conduction phenomenon even in the presence of a local electric

field E. As temperature increases (T > 0 K) atoms vibrate around their lattice sites. Vibrating atoms can be described as a quasi-particle called **phonon**. These phonons interact with electrons involved in covalent bonds (it is said that they "collide"). In such collisions the electrons receive an average energy of the order of several tens of meV at T = 300 K. This energy is not evenly distributed and, in some cases, it may be sufficient to free an electron from the covalent bond (fig. 1.5 right), and let it to take part in the conduction (conduction electrons). The electron leaves behind a non saturated covalent bond (a vacancy or a **hole**) which is modeled as a fictitious particle with a positive charge equal to the elementary charge q = 1.602 x 10^{-19} C. The concentration of free electrons and holes in the lattice increases with temperature T.
From the band model point of view, to say that a valence electron is engaged in a covalent bond means that it is allocated in a low energy state or, equivalently, that it is included in the valence band. The bandgap E_G is the minimum energy above which an electron can be released from bonds. To say that an electron is released means that energy was provided sufficient to let the electron occupy a quantum state in the conduction band. Typically, the transition is not direct (band-band), but indirect: occurs through quantum states allowed in the bandgap, said G-R centers, resulting from impurities and lattice defects (inevitably present).
So for T $\rightarrow$ 0 K all the 4 x N quantum states in the valence band are full (all the electrons are engaged in covalent bonds) and the 4 x N quantum states in the conduction band are empty (there are no free electron).
The importance of the parameter E_G in defining the properties of a semiconductor is clear. Its value depends on the particular material and on the temperature (at T = 300 K typical values for insulators and conductors are respectively $E_G > 3$ eV and $E_G \sim 0.1$ eV); for silicon E_G (T $\rightarrow$ 0 K) = 1.17 eV and E_G (T $\rightarrow$ 300 K) = 1.124 eV. Thus the increase of the concentration of free electrons and holes with increasing temperature, depends not only on the increase of the vibrational energy of the atoms, but also on the reduction of the bandgap (that is energy required to release electrons from the bonds).

1.3.2 Direct and Indirect Bandgap

A free electron moving in a crystal lattice, unlike what would happen in a vacuum, is subject to lattice forces (due to interaction with lattice atoms). To treat this problem we will appeal to the laws of classical mechanics for a charged particle in vacuum, considering the **effective mass $\mathbf{m}_k$**[6] instead of the actual mass m_e, and the charge -q.

[6] Is a quantity that is used to simplify band structures by constructing an analogy to the behavior of a free particle with that mass. For silicon is $m_k = 0.26 \cdot m_e$

For the free electron in vacuum the dispersion relation[7] holds, which binds the kinetic energy to the momentum:

$$E_{kin} = \frac{1}{2}\frac{p^2}{m_e}. \tag{1.2}$$

For a free electron within the crystal it is possible to write a similar equation considering the effective mass m_k and the **crystal momentum** (or quasimomentum) instead of the momentum.
It is a momentum-like vector associated with electrons in a crystal lattice. It is defined by the associated wave vectors k of this lattice, according to

$$\bar{p} = \hbar \cdot k, \tag{1.3}$$

where $\hbar$ is the reduced Planck's constant. It is possible to demonstrate that in the interactions between electrons, holes, and other quasi-particles (such as photons and phonons) energy and momentum of the crystal are conserved.
It is seen that the energy levels E_C (inferior edge of the counduction band) and E_V (superior edge of the valence band) are not constant but vary with the crystallographic direction and with the quasimomentum.
Directions [1 0 0] and [1 1 1] are preferred for the description of the properties of materials, so it is usual to illustrate the trend of E_C and E_V with respect to the quasimomentum along the latter (fig. 1.6).

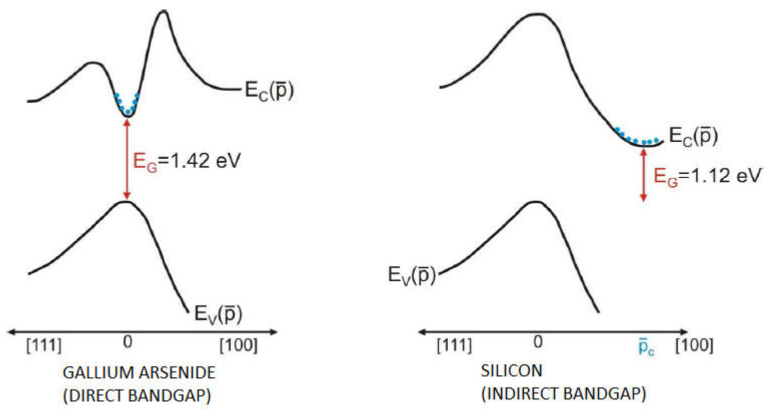

Figure 1.6: Trend of E_C and E_V with respect to the quasimomentum along the crystallographic directions [1 0 0] and [1 1 1] for gallium arsenide and silicon

In figure 1.6 band structures of silicon and gallium arsenide are compared. E_V has a maximum in $\bar{p} = 0$ for both gallium arsenide and silicon, while E_C has a

[7]Describes the effect of dispersion in a medium on the properties of a wave traveling within that medium

minimum in $\bar{p} = 0$ for the gallium arsenide, and in $\bar{p} \neq 0$ for silicon in the direction [1 0 0].
E_V and E_C trends are parabolic in the neighborhood of the maximum and minimum and the kinetic energy of a free electron is null when it lies on the minimum of E_C (condition that never occurs as we will see later). Free electrons are allocated in quantum states in the vicinity of the minimum E_C, and not far from the edge $E_C(\bar{p})$. The bandgap energy corresponds to the distance:

$$E_G = min[E_C(\bar{p})] - max[E_V(\bar{p})]. \tag{1.4}$$

Materials such as gallium arsenide where the minimum of E_C and the maximum E_V interface for the same quasimomentum are called **direct bandgap** semiconductors, otherwise (such as silicon) they are called **indirect bandgap** semiconductors.
It is clear that the following dispersion relations can be written for a free electron in a crystal if we suppose that free electrons are all immediatly near to the edge of $E_C(\bar{p})$:

$$E_{kin}(GaAs) = E - min[E_C(\bar{p})] = \frac{1}{2}\frac{\bar{p}^2}{m_k}, \tag{1.5}$$

$$E_{kin}(Si) = E - min[E_C(\bar{p})] = \frac{1}{2}\frac{(\bar{p} - \bar{p}_c)^2}{m_k}. \tag{1.6}$$

From these equations is inferred that a free electron in silicon has $E_{kin} = 0$ if $\bar{p} = \bar{p}_c$. But this condition cannot be achieved, because there are not quantum states allocable by electrons on the minimum of the conduction band. In both cases we have:

$$\frac{d^2E}{d\bar{p}^2} = \frac{1}{m_k}, \tag{1.7}$$

so this effective mass varies with the curvature of E_C. If the curvature is narrow (as for GaAs) then the second derivative is big and m_k is small, otherwise (as for Si) m_k is bigger:

$$m_k(Si) > m_k(GaAs). \tag{1.8}$$

1.3.3 Statistics of Semiconductors: Fermi Dirac Distribution and the Mass Action Law

A crystal is said to be in thermodynamic equilibrium when it is under steady conditions and in the absence of electrical loads (d.d.p.) or optical stresses.

The concentration of available quantum states in the conduction band for the energy level E has the following expression:

$$N(E) = \gamma\sqrt{E - E_C}[cm^{-3} \cdot eV^{-1}] \; for \; E \geq E_C, \tag{1.9}$$

where $\gamma = 4\pi\sqrt[3]{\frac{2m_n}{h^2}}$. The quantity m_n is defined as the **electron's density of states effective mass** and, for silicon is $m_n = 1.1 \; m_e$. In the immediate vicinity of the lower edge of the conduction band there are few quantum states allocated by electrons, while their concentration increases with increasing energy [8].
The concentration of available quantum states in the valence band for the energy level E has the following expression:

$$N'(E) = \gamma'\sqrt{E_V - E}[cm^{-3} \cdot eV^{-1}] \; for \; E \leq E_V, \tag{1.10}$$

where $\gamma = 4\pi\sqrt[3]{\frac{2m_p}{h^2}}$. The quantity m_p is defined as the **hole's density of states effective mass** and, for silicon is $m_n = 1.93 \; m_p$.
If the crystal is in thermodynamic equilibrium, one can introduce the **Fermi-Dirac distribution F(E)** (fig. 1.7), which expresses the probability that a quantum state with energy E is allocated by an electron.

$$F(E) = \frac{1}{1 + exp\left(\frac{E-E_F}{KT}\right)}, \tag{1.11}$$

where E_F is the **Fermi Level** and K is the Boltzmann's constant.

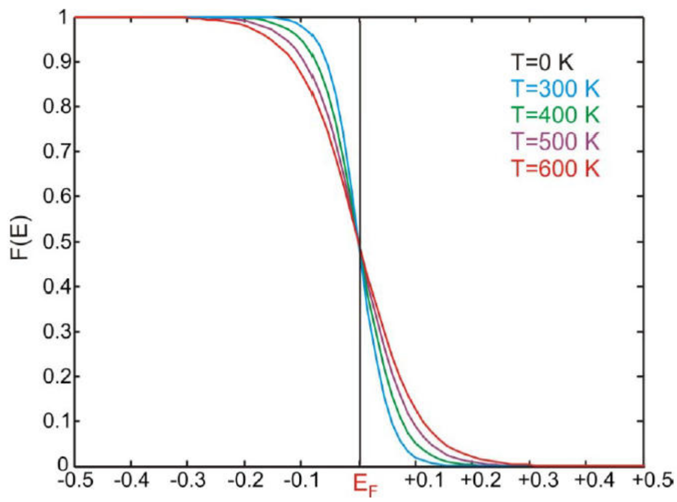

Figure 1.7: Fermi Dirac distribution with respect to temperature variations

The Fermi level, is the energy level for which the probability of occupation of a quantum state is $\frac{1}{2}$ regardless the value of T. It is clear that, for E > E_F, the probability an electron occupies quantum state increases with temperature, while for E < E_F this probability decreases.
This is reasonable if we take into account the fact that the energy of electrons increases with T, and thus is more likely for electrons to occupy quantum states at higher energy levels.
For T → 0 K the occupation probability is null for E > E_F and 1 for E < E_F.
A similar equation exsists for holes:

$$F'(E) = 1 - F(E) = \frac{1}{1 + exp\left(\frac{E_F - E}{KT}\right)}, \tag{1.12}$$

that defines the probability that a quantum state at the energy level E is not occupied by an electron.
In intrinsic silicon at T = 300 K we have the following relation:

$$n = p = n_i = 1.45 \cdot 10^{10} cm^{-3}, \tag{1.13}$$

where p [cm^{-3}] is the hole's concentration, n [cm^{-3}] is the free electron concentration and n_i [cm^{-3}] is the intrinsic concentration of charge carriers in the lattice. This brings to a resistivity equal to $\rho = 2.5 \cdot 10^5 [\Omega \cdot cm]$.
On the basis of definitions given below, it is possible to know the total concentration of free electrons and holes expressed in terms of the energy gap between the Fermi level and the edge of the conduction and the valence band respectively with the semiconductor (pure or doped) in termodynamic equilibrium[8]:

$$n = N_C \cdot exp\left(-\frac{E_C - E_F}{KT}\right), \tag{1.14}$$

$$p = N_V \cdot exp\left(-\frac{E_F - E_V}{KT}\right), \tag{1.15}$$

where N_C is the effective density of states in the conduction band (it is 2.8 x 10^{19} cm^{-3} for silicon at 300K temperature), and N_V is is the effective density of states in the valence band (it is 1.04 x 10^{19} cm^{-3} for silicon at 300K temperature). By means of these definitions is now possible to locate the position of the Fermi level

[8]These expressions come from the fact that the concentration of free electrons (holes) for a energy interval dE, with E belonging to the conduction (valence) band, is given by the concentration of quantum states can be allocated in the energy range dE (N(E) · dE) times the probability that they are occupied (F(E)): $\int_{E_C}^{E_0} N(E)F(E)dE$ for electrons and $\int_{E_{V_{inf}}}^{E_V} N'(E)F'(E)dE$ fro holes

between the valence and conduction bands [6], it is almost in the middle of the bandgap for a pure semiconductor but depends also on the temperature:

$$E_{F_i} = \frac{E_C + E_V}{2} - \frac{KT}{2} \cdot ln \frac{N_C}{N_V}, \tag{1.16}$$

Temperature Dependence

Experimentally it is found that N_C and N_V have a positive temperature coefficient according to:

$$N_C(T) = N_C(300K) \sqrt[3]{\frac{T}{300K}}, \tag{1.17}$$

$$N_V(T) = N_V(300K) \sqrt[3]{\frac{T}{300K}}, \tag{1.18}$$

In intrinsic silicon at T = 300 K in termodynamic equilibrium we have the following relation:

$$n = p = n_i, \tag{1.19}$$

so by substitution with equations 1.14 and 1.15 we obrain the following expression for n_i:

$$n_i^2 = N_C N_V \cdot exp\left(-\frac{E_G}{KT}\right), \tag{1.20}$$

With regard to the lattice temperature T dependence, it is clear that n_i has a positive temperature coefficient which takes into account two mechanisms:

- increase of the atoms vibrational energy and, therefore, increse of the average energy conferred to electrons in covalent bonds;
- bandgap reduction and, therefore, reduction of the minimum energy required to release electrons from bonds.

This dependence is expressed as follows:

$$n_i(T) = A_0 \cdot T^{\frac{3}{2}} exp\left(-\frac{E_{G_0}}{2KT}\right), \tag{1.21}$$

where

$$A_0[cm^{-3} \cdot K^{-\frac{3}{2}}] = \sqrt{N_C(300K) N_V(300K) \cdot \left(\frac{1}{300K}\right)^3 \cdot exp\left(\frac{\gamma}{K}\right)} \tag{1.22}$$

contains all the temperature sensitive terms, and $E_{G_0} = E_G(T) + \gamma T$ is a coefficient which comes out from the bandgap decay law[9].
If we consider the experimental intrinsic concentration for silicon n_i(300K) = 1.45 x $10^{-10} cm^{-3}$, the dependence of n_i on the temperature is shown in figure 1.8.

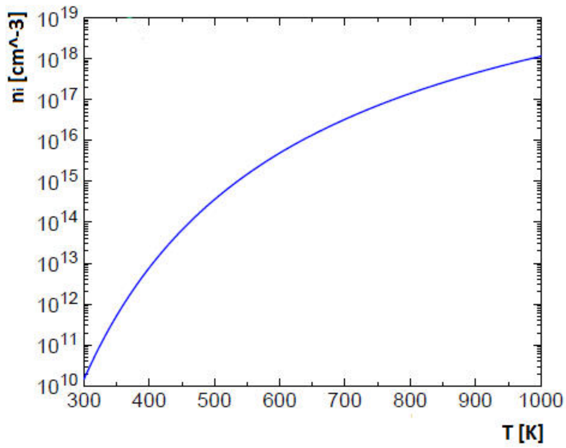

Figure 1.8: Intrinsic concentration trend with respect to temperature variations

It is useful to express the concentrations of free electrons n and holes p in terms of the intrinsic concentration n_i by means of the Shockley equations:

$$n = n_i \cdot exp\left(-\frac{E_F - E_i}{KT}\right), \tag{1.23}$$

$$p = n_i \cdot exp\left(-\frac{E_i - E_F}{KT}\right), \tag{1.24}$$

so we can easily derive the **mass action law**:

$$p \cdot n = \left[n_i \cdot exp\left(-\frac{E_F - E_i}{KT}\right)\right] \cdot \left[n_i \cdot exp\left(-\frac{E_i - E_F}{KT}\right)\right] = n_i^2, \tag{1.25}$$

This product is independent on the Fermi level, which, as will be seen hereinafter, is an indicator of the material doping level; so the product is independent of the type and level of doping. Indeed it is equal to n_i which is a mere function of temperature.
The mass action law expresses the fact that if one tries to increase the concentration of a certain polarity carriers throug doping, the system reacts by reducing the opposite polarity carriers, so as to preserve the consistency of the product.

[9] $E_G(T) = E_G(0) - \frac{\alpha T^2}{\beta + T}$ where α = 4.73 x 10_{-4} [eV/K^2] and β = 636 K for silicon

The law of mass action also describes the fact that higher is the doping, more unlikely is to break covalent bonds. So the quantity of minority carriers (the less abundant charge carriers obtained only through the breaking of covalent bonds) decreases as the doping.
In general this law is important because in an extrinsic semiconductor at fixed temperature, being known the concentration of the majority carriers (is almost equal to that of the dopant), one can achieve the concentration of the minority carriers.

1.3.4 Doping

It is possible to intentionally contaminate a semiconductor with foreign atoms to give a suitable conductivity to the material, through the enrichment of free charge carriers of a certain polarity; in this case, the semiconductor is said extrinsic, impure, or doped. The entire development of semiconductor devices was based on doping.
When silicon (tetravalent atom) is doped with trivalent atomic species (boron, gallium and indium), the concentration of holes is increased (and the concentration of electrons decreases according to the law of mass action).
In this case holes are the **majority carriers**, electrons are the **minority carriers** and the silicon is said **P-type doped**.
When silicon is doped with pentavalent atomic species (arsenic and phosphorus, but also antimony), in a controlled manner the concentration of electrons increases (and the concentration of holes decreases).
In this case electrons are the majority carriers, holes the minority carriers and silicon is said **N-type doped**.
Dopant atoms ar put into the lattice in substitution of silicon atoms. Typical dopant concentrations are in the range $10^{14} \div 10^{20}$ cm^{-3}. This means that there are very few impurities compared to silicon atoms (5 x 10^{22} cm^{-3}); therefore there is a negligible disturbance of the lattice structure and so band structure is not changed appreciably.
Let us consider N-type silicon doped with arsenic (atomic number 33). The stable configuration is reached because arsenic has 5 valence electrons, 4 to form covalent bonds with adjacent silicon atoms (so the octet is reached) and 1 quasi-free[10] that is characterized by an ionization energy equal to $E_{DI} \sim meV$ (fig. 1.9).
At T = 300 K, in intrinsic silicon, only 1.45 x 10^{10} cm^{-3} electrons are released from covalent bonds by vibrational energy. Since the ionization energy of the quasi-free

[10] Arsenic atom is modeled as a hydrogen atom, so the ionization energy required to release the sigle electron that does not participate in the octet is $E_{DI} = \frac{13.6}{(11.9)^2} \cdot \frac{m_n}{m_e} = 54$ meV $\ll E_G$ = 1.12 eV

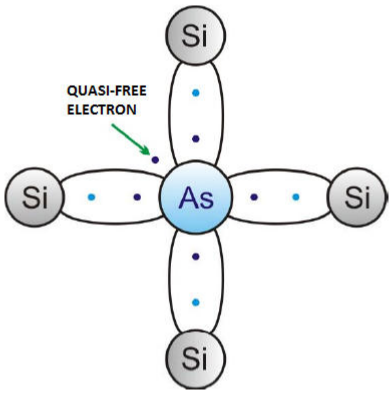

Figure 1.9: 2-D lattice model for silicon doped with arsenic

electrons is in the order of a few tens of meV, their interaction with T = 300 K vibrating atoms provide for sure enough energy to release them all.
In this case we say that the dopant is activated. This means that if in the silicon are introduced in a controlled way 10^{18} cm^{-3} arsenic atoms (also called **donors**), at T = 300 K, there are 10^{18} cm^{-3} free electrons in the lattice.
In the energy band model we have quantum states can be allocated in the band gap at a distance $E_{DI} = E_C$ - E_D[11] $\sim$ meV from the lower limit of the conduction band, and also called **donor's activation energy**.
It can be assumed that all these quantum states are roughly at the same energy level E_D because of the fact that the impurities are very few in the host lattice, so they do not interact between them (there is no intersection between their orbitals) and so in this case the Exclusion Principle does not apply (fig. 1.10).

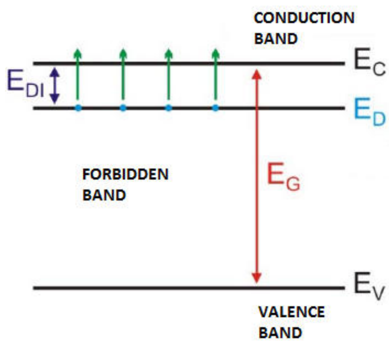

Figure 1.10: Band model for a N-type silicon lattice

[11]E_D is the energy owned by donor's electrons

Let us consider P-type silicon doped with boron (atomic number 5). The stable configuration is reached because arsenic has 3 valence electrons to form covalent bonds with adjacent silicon atoms. In this case the octet is not reached since the fourth covalent bond is not formed. Only a few tens of meV is required to make an electron disappears from a Si-Si bond, close to the boron atom, and reappear in the not saturated covalent bond (fig. 1.11).

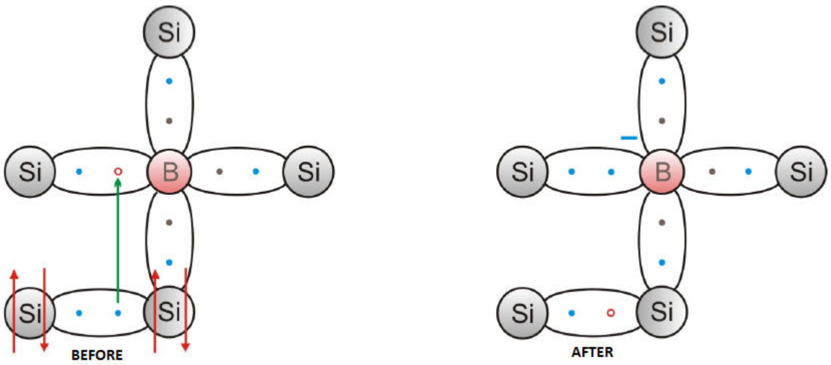

Figure 1.11: 2-D lattice model for silicon doped with boron

Since the trivalent elements accept an electron from a Si-Si covalent bond they are called **acceptors**. In the energy band model we have quantum states that can be allocated in the band gap at a distance[12] $E_{AI} = E_A - E_V \sim$ meV from the lower limit of the conduction band, and also called **acceptor's activation energy**.
It can be assumed that all these quantum states are roughly at the same energy level E_A. At $T \rightarrow 0$ K all quantum states introduced by the acceptors are empty; with increasing T more and more electrons are accepted from the valence band, resulting in the creation of holes; at $T = 300$ K all the quantum states are allocated by electrons (fig. 1.12).

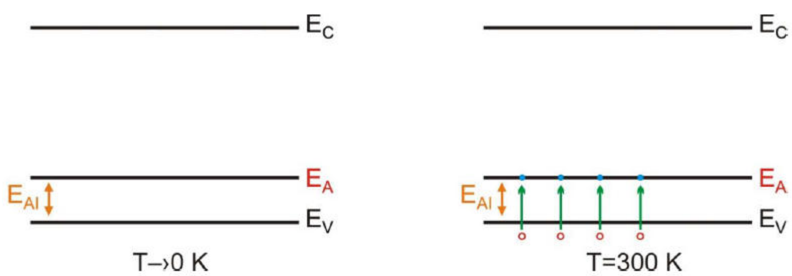

Figure 1.12: Band model for a P-type silicon lattice

[12] E_A is the energy owned by acceptor's hole

The Fermi level E_F is indicative of the type and concentration of dopant in a semiconductor. It is seen that in the intrinsic silicon is located slightly below the center of the band gap.
In N-type silicon, a remarkable quantity of electrons is introduced in the conduction band, therefore it is reasonable to think that the function F(E) shifts towards higher energies, and so E_F increases. By contrast, if silicon is P-type, there are fewer free electrons than in intrinsic silicon, and, in addition, the covalent bonds are depleted of electrons; this results in a reduction of F(E) and, therefore, of E_F. (fig. 1.13)

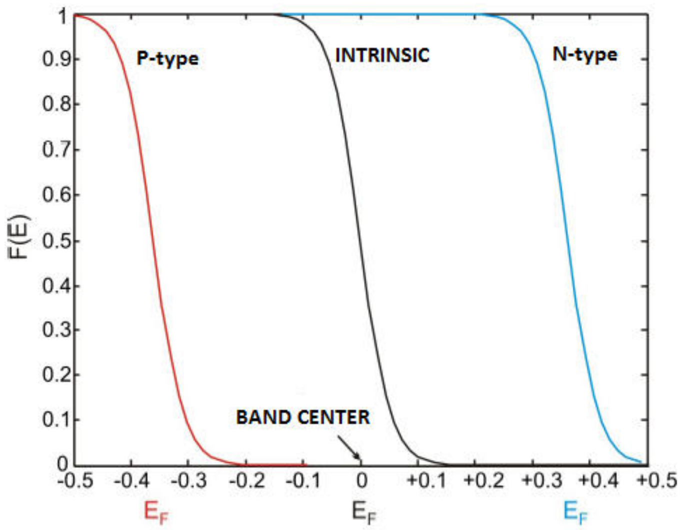

Figure 1.13: Fermi level in doped semiconductors

If in a semiconductor occurs the following condition, for which it is heavily doped:

$$E_C - E_F \leq 3kT \ \textit{For N-type} \ , \quad E_F - E_V \leq 3kT \ \textit{For P-type} \tag{1.26}$$

it is called **degenerate**. In a degenerate semiconductor impurities within the host lattice are so many that their orbitals begin to interact, the Exclusion Principle comes in, quantum states can not be all at a same energy level and a band of allowed energy levels in the forbidden band is created. This leads to a reduction of the bandgap (fig. 1.14) with respect to the E_G value for a non-degenerate semiconductor (a phenomenon called **band gap narrowing or BGN**). The new value is given by:

$$E_{G_{eff}} = E_G - \Delta E_{G,BGN} \tag{1.27}$$

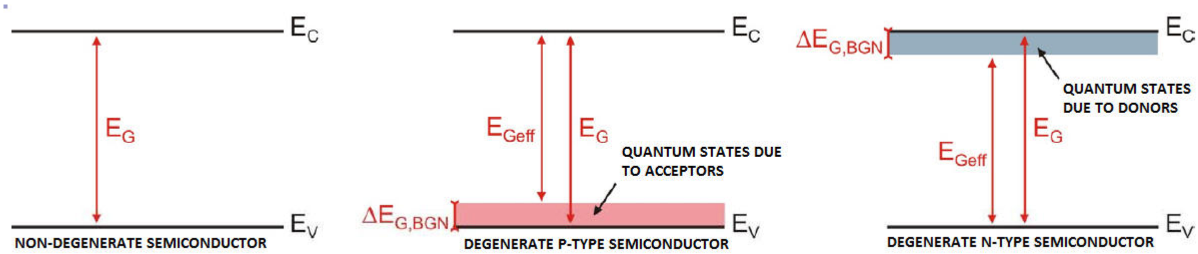

Figure 1.14: Phenomenology of the band gap narrowing

Temperature Dependence

Let us consider a doped silicon sample in thermodynamic equilibrium with donor concentration equal to $N_D = 10^15$ cm^{-3}. The temperature dependence of the concentration of the majority n_{no} in the temperature range 0 to 600 K is given by:

$$n_{no}(T) = n_D(T) + n_V(T); \tag{1.28}$$

where n_D is the concentration of electrons due donor atoms and n_V is the concentration of electrons due to the breaking of covalent bonds.
In general $n_V < n_i$, because, when a semiconductor is doped, less covalent bonds break. For $N_D = 10^{15}$ cm^{-3}, n_V is not negligible only for T > 500 K. At lower temperatures we can say that $n_{no} \sim n_D$(T) (fig. 1.15).

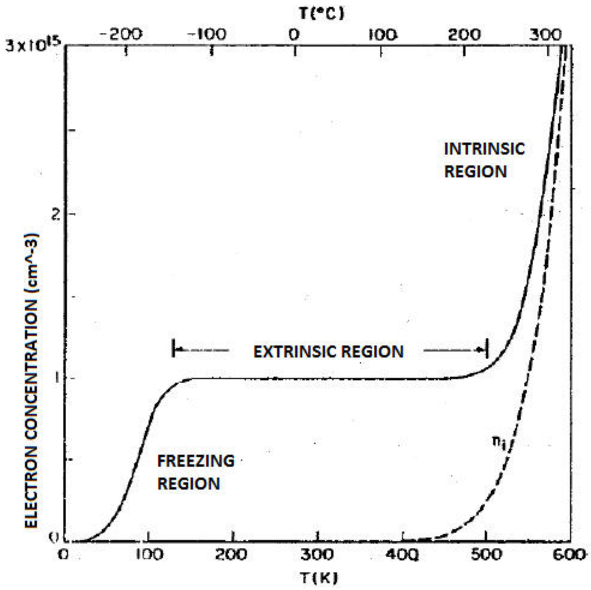

Figure 1.15: Temperature dependence of the electron concentration

For T $\leq$ 120K we are in the freeze-out regime (or freezing region) where the concentration of the majority carriers is give by:

$$n_{no} \sim N_D \cdot (1 - F(E_D)), \tag{1.29}$$

where N_D is the concentration of quantum states at the energy level E_D and (1 - F(E_D)) is the probability that these states are not filled with electrons. For T > 120K every donor has given a free electron to the lattice son the electron concentration is equal to the donor atoms concentration: $n_D(T) = N_D$. For 120 K $\leq$ T $\geq$ 500 K we are in the extrinsic region where the majority concentration is almost equal to donor atoms concentration: $n_{no}(T) \sim N_D$. For 500 K $\leq$ T $\geq$ 600 K we have $n_{no}(T) = n_D(T) + n_V(T)$ and for T > 600 K we have $n_V \sim n_i \gg N_D$ so $n_{no}(T) \sim n_i(T)$ and it is called intrinsic region.
Moreover we can see that the gap E_C - E_F in estrinsic region (where all impurities are activated) increases with temperature according to the following relation:

$$E_C - E_F = kT \cdot ln\frac{N_C(T)}{N_D}. \tag{1.30}$$

We expect this kind of effect because as T increases the semiconductor approaches the intrinsic region, where the Fermi level is close to the band center.
If T increases the band gap decreases while if N_D increases, the increase of the gap E_C - E_F becomes slower. Intuitively, for a higher N_D more covalent bonds have to break to bring the semiconductor to the intrinsic region, which means that **a higher temperature is needed to achieve the same value of E_C-E_F** (fig. 1.16).

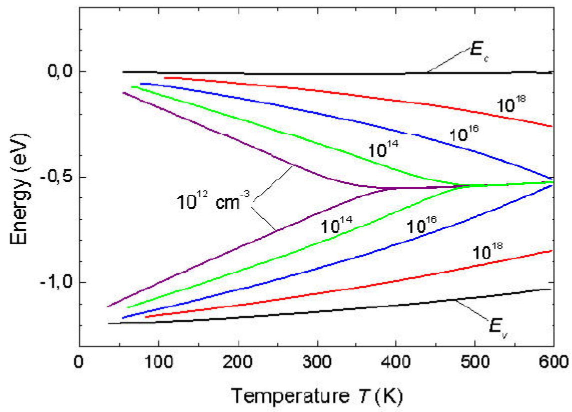

Figure 1.16: Dependence of the bandgap by temperature and concentration of donor atoms

1.3.5 Transport and Generation-Recombination Phenomena

Two transport phenomena occur in semiconductors: **drift** and **diffusion**.
When an electric field E is applied across a semiconductor material, a current is produced due to the flow of charge carriers, it is called drift current and, for electrons, its density is given by:

$$J_{n,drift} = -qnv_n, \tag{1.31}$$

where q is the elementary charge, n is the electron concentration and $v_n = -\mu_n \mathbf{E}$ is the electron drift velocity (μ_n is the electron mobility[13]). For holes a similar relation holds:

$$J_{p,drift} = qpv_p, \tag{1.32}$$

where q is the elementary charge, p is the hole concentration and $v_p = \mu_p \mathbf{E}$ is the hole drift velocity (μ_p is the hole mobility). The total drift current density is given by the sum of these two contributions.
Diffusion is the other transport mechanism, is related to the thermal agitation and is due to the change in concentration of the carrier particles in a semiconductor region; the carriers tend to flow from the higher concentration zone to a lower concentration zone since it becomes uniform. Diffusion current densities for electrons and holes are given by:

$$J_{n,diff} = qD_n \frac{dn}{dx}, \quad J_{p,diff} = -qD_p \frac{dp}{dx}, \tag{1.33}$$

where D_n (36 cm^2/s for silicon at T= 300K) and D_p (12 cm^2/s for silicon at T= 300K) are the diffusion coefficients[14] (or diffusivity) for electrons and holes respectively.
The conduction of current in a semiconductor device is due to both these phenomena. So the total current densities for electrons and holes is given by the sum of drift and diffusion current densities. In particular, we can obtain **Einstein Relations** for electrons and holes from the total current densities expressions in thermodynamic equilibrium conditions:

$$J_n = qn\mu_n \mathbf{E} + qD_n \frac{dn}{dx} = 0, \quad J_p = qp\mu_p \mathbf{E} - qD_p \frac{dp}{dx} = 0, \tag{1.34}$$

[13]This parameter characterizes how quickly an electron can move through a semiconductor, when pulled by an electric field.

[14]It is a proportionality constant between the molar flux due to molecular diffusion and the gradient in the concentration of the species

Einstein relations link the two significant constants that characterize transport of free carriers in a semiconductor by drift (mobility) and diffusion (diffusivity).

$$D_n = \mu_n \frac{kT}{q}, \quad D_p = \mu_p \frac{kT}{q}. \tag{1.35}$$

This equation is an early example of a fluctuation-dissipation relation, which is a powerful tool in statistical physics for predicting the behavior of systems that obey detailed balance [15].

Carrier **generation** and **recombination** are processes by which electrons and holes are created and eliminated. It occurs when an electron makes transition from the valence band to conduction band, as a result of interaction with other electrons, holes, photons, or the vibrating crystal lattice itself. These processes must conserve both quantized energy and momentum, and the vibrating lattice plays a large role in conserving momentum as photons carry very little momentum in relation to their energy.

Recombination and generation are always happening in semiconductors, both optically and thermally, and their rates are in balance at equilibrium. The product of the electron and hole densities is a constant at equilibrium (for the mass action law), maintained by recombination and generation occurring at equal rates. When there is a surplus of carriers, the rate of recombination becomes greater than the rate of generation, driving the system back towards equilibrium. Likewise, when there is a deficit of carriers, the generation rate becomes greater than the recombination rate, again driving the system back towards equilibrium. As the electron moves from one energy band to another, the energy and momentum that it has lost or gained must go to or come from the other particles involved in the process.

Depending on which particles are involved in the process, there are different generation ricombination phenomena. They can be direct if the transition occurs directly between valence and conduction bands (band-band generation/recombination); they can be indirect if this transition occurs through quantum states allocable in the bandgap, said generation-recombination (G-R) centers or traps, due to impurities in the lattice (Shockley-Read-Hall process); they can be thermal if the process occurs through interactions with phonons; they can be radiative if the process involves photons. During radiative recombination, a form of spontaneous emission, a photon is emitted with the wavelength corresponding to the energy released. Because the photon carries relatively little momentum, radiative recombination is significant only in direct bandgap materials.

When photons are present in the material, they can either be absorbed, generating a pair of free carriers, or they can stimulate a recombination event, resulting in a generated photon with similar properties to the one responsible for the event. Absorption is the active process in semiconductor photodetectors, so is of particular interest in this thesis.

More precisely, let us suppose that a direct bandgap semiconductor is subjected to a light radiation characterized by frequency ν such that photons meet the **absorption condition**:

$$h\nu > E_G. \tag{1.36}$$

In that case the covalent bond is broken due to the energy provided by the incident photon (the electron absorbs the photon). The transition in the band diagram is vertical (fig. 1.17): photon absorption does not imply variations in the electron's quasimomentum.

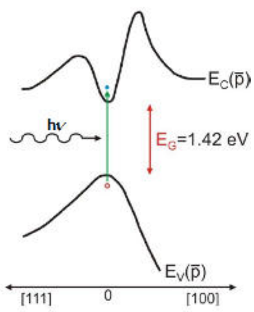

Figure 1.17: Direct radiative generation in a direct bandgap semiconductor

If the same appens to an indirect bandgap semiconductor, the transition requires a significant variation of electron's quasimomentum (fig. 1.18). But since photons do not change electron's quasimomentum, an interaction with the lattice is needed. Being necessary interaction with phonons in addition to photon absorption, the direct radiative generation occurs rarely with respect to direct bandgap semiconductors, which therefore lend themselves more to optical applications.

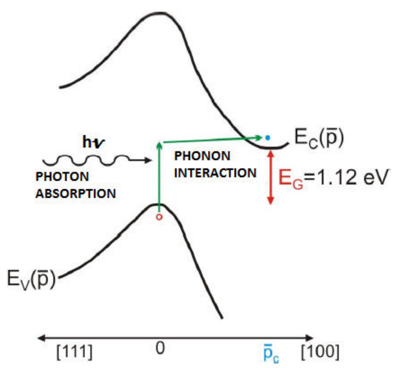

Figure 1.18: Direct radiative generation in an indirect bandgap semiconductor

But it is possible to obtain indirect radiative generation, even with an electromagnetic radiation whose photons do not respect the absorption condition, if the silicon sample is impure and contains traps (or G-R centers); the electron absorbs the energy of two (or more) photons and interacts with phonons, in this way smaller variations in the electron's quasimomentum are required to overcome the bandgap through G-R centers (fig. 1.19).

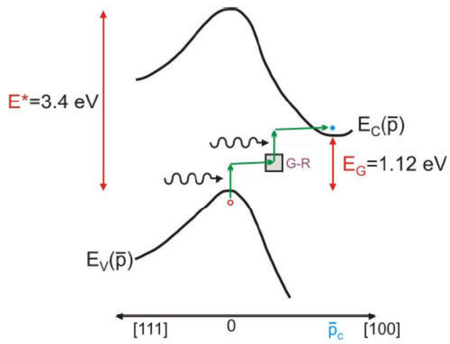

Figure 1.19: Indirect radiative generation in an indirect bandgap semiconductor

Similar considerations hold for the recombination mechanism.

1.3.6 P-N Junction

The P-N junctions are crucial devices in electronics since they are elementary building blocks of most semiconductor devices. A P-N junction is obtained by interfacing an N-type semiconductor with a P-type semiconductor[15], the contact point is called "metallurgical junction" x_j.
Let us suppose to be in the ideal case, at first charge carriers behave as if they are in two separate crystals in thermodynamic equilibrium. Then, at the boundary, it begins a diffusion mechanism which brings free charge carriers to migrate to the regions in which they are minority (minority carrier injection); large part of these injected carriers is lost by recombination. Both $J_{n,diff}$ and $J_{p,diff}$ are reduced over time. After a certain time interval space charge distributions are changed (fig. 1.20).
The crystal is still electrically neutral, but the quantity of free carriers was reduced because of recombination.
A fixed space charge region depleted from mobile carriers, called **space charge region SCR**, is created (fig.1.21) where only the fixed ions (donors or acceptors) remain. The resulting charge dipole induces the presence of a electric field E (called **built-in electric field**) directed as -x; the amplitude of dipole charge and

[15]A P^+ implantation in a N doped semiconductor is performed by means of a planar process

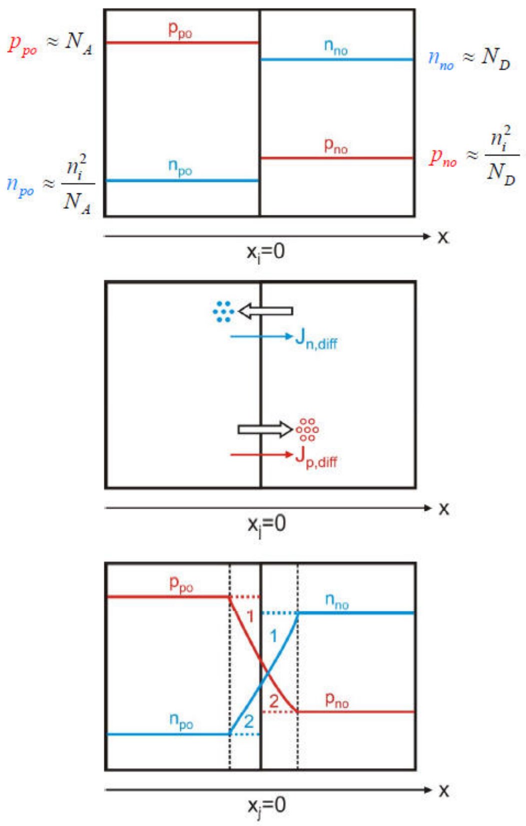

Figure 1.20: Free charge diffusion at the metallurgic junction in a P-N juncion

field increases as the diffusion proceeds. The field E, in turn, generates drift currents which tend to oppose the diffusion currents, gradually reducing the minority injection and bringing the system to equilibrium (steady-state condition).
Out of the SCR there are the neutral regions where charge carriers behave as if they are in two separate crystals in thermodynamic equilibrium. In this conditions the P-N junction is said to be open circuited and, being the structure macroscopically neutral, there must be the neutrality condition:

$$x_p \cdot qN_A = x_n \cdot qN_D, \tag{1.37}$$

where q N_A and q N_D are the space charge densities ρ for the P side and the N side respectively, x_p and x_n are the thicknesses of the depletion regions for the P side and the N side respectively. From this equation is evident that if one of the two samples is much more doped than the other, for example if $N_A \gg N_D$, the depletion region will extend only throughout the N-type region.
The trend of the built-in electric field through the depletion region, depicted in

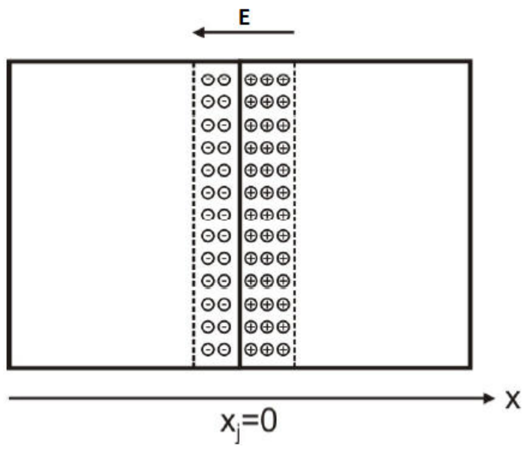

Figure 1.21: Space charge region

figure 1.22, is found integrating the Poisson equation:

$$E(x) = x \cdot \frac{\rho}{\epsilon_S}. \tag{1.38}$$

Typical values for built-in electric fields are in the range $10^3 \div 10^5$ V/cm. Linked to this electric field there is a built-in potential given by:

$$\frac{d\Psi}{dx} = -E(x) \quad \rightarrow \quad \Psi(x) = V_{bi} = x_n^2 \cdot \frac{qN_D}{2\epsilon_S} + x_p^2 \cdot \frac{qN_A}{2\epsilon_S}, \tag{1.39}$$

which is not accesisible from the outside. This expression, together with the neutrality condition, allows to calculate the thickness of the depletion region:

$$W = \sqrt{\frac{2\epsilon_S}{q} V_{bi} \left(\frac{1}{N_D} + \frac{1}{N_A}\right)}. \tag{1.40}$$

It is possible to derive V$_{bi}$ as a function of the lattice temperature and of the charge carriers concentrations in the neutral zone by means of the Boltzmann statistics:

$$V_{bi} = \frac{kT}{q} ln \frac{N_A N_D}{n_i^2(T)}. \tag{1.41}$$

From this equation is evident that V$_{bi}$ decreases as temperature increases because of $n_i^2(T)$ at the denominator of the logarithm. This behavior is due to the fact that the concentration of the minority increases, the diffusion decreases and then also the system reaction to the diffusion decreases.
Let us now consider the band structure of the P-N junction. In the P-type crystal the Fermi level is closer to the valence band, while in the N-type crystal it is closer to the conduction band. After the P-N junction is created, in the transient before

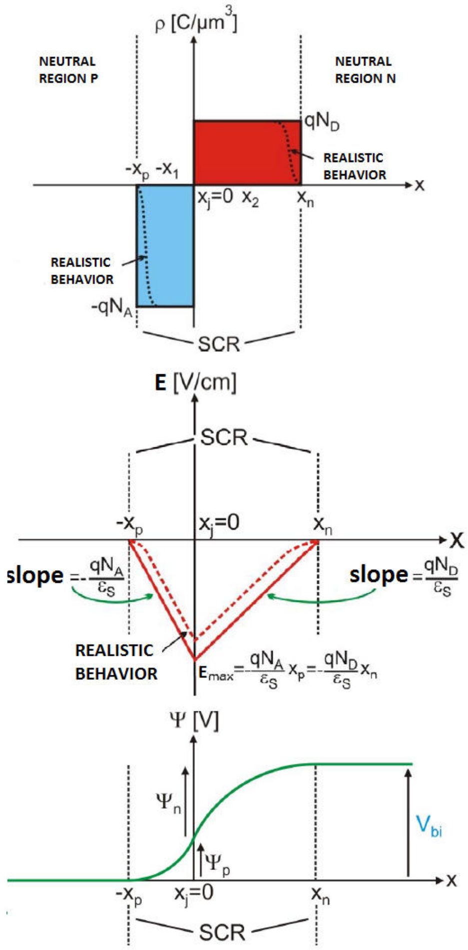

Figure 1.22: P-N junction characteristic quantities

the system reach the thermodynamic equilibrium, the potential energy of free electrons, i.e., the edge of the conduction band $E_C(x)$, can no longer be uniform, because of the presence of the quadratic potential $\Psi(x)$[16]. In particular in the P side we have the minimum of the potential energy (0) and in the N side we have the maximum ($-qV_{bi}$).
Since the system is at equilibrium, the Fermi level should be uniform throughout the material. Furthermore, far from the junction, there are two simple P-type and N-type semiconductors, so $E_{F_P} - E_V$ and $E_C - E_{F_N}$ must be constant in the two sides respectively. Since even the bandgap E_G has to be constant throughout the system, this results in a band bending close to the junction point (fig. 1.23) according to the following equations:

[16]The potential energy of a charged particle varies as $-q\Psi(x)$

$$E_C(x) = E_{C_P} - q\Psi(x), \quad E_V(x) = E_{V_P} - q\Psi(x) \tag{1.42}$$

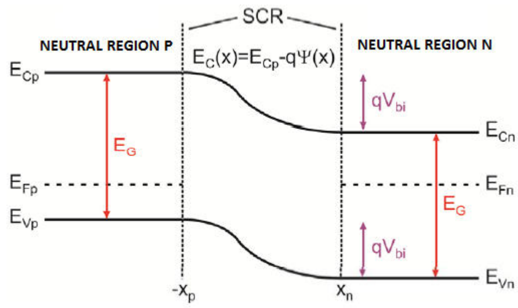

Figure 1.23: Band bending at the metallurgical junction in a P-N junction

This bending results in the creation of a potential barrier of height V_{bi}, which prevents the minority carriers injection.
The free electrons that drift from the neutral region P to N are few (because they are the minority carriers); they lose and regain kinetic energy in the SCR because of lattice collisions and the presence of the built-in field E.
The free electrons that diffuse from the neutral region N to P are few (because of the potential barrier); the situation is such that the flow of drift (P $\rightarrow$ N) and diffusion (N $\rightarrow$ P) electrons are balanced (fig. 1.24); in general $J_{n,drift}$ and $J_{n,diff}$ are high (in modulus are the same) since E and the gradient dn/dx in the SCR are high.

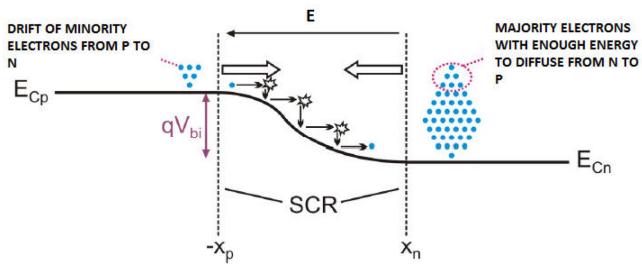

Figure 1.24: Drift and diffusion at the metallurgical junction in a P-N junction

1.3.7 Forward Biasing

When a junction is connected to a potential difference (PD) V, such as V > V_γ[17], with the positive terminal connected to the P-type side and the negative terminal connected to the N-type side, the junction is called **forward biased**.
V is opposed to V_{bi}, and then the potential barrier, which contrasted the carriers spread in the open circuit junction, is reduced to $V_{bi}-$ V; the P $\rightarrow$ N drift and N $\rightarrow$ P diffusion probabilities increase, and a remarkable carriers injection from both sides of the junction occurs.
Electrons diffusion from N to P through the depletion region towards the positive terminal, where their concentration is low, is the dominant phenomenon (fig. 1.25).

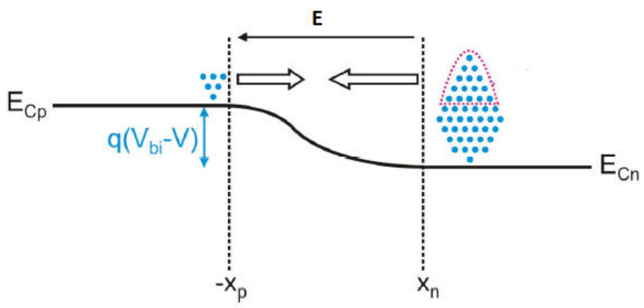

Figure 1.25: Electron diffusion for the PN junction in forward biasing

During the diffusion they will recombine with holes (majority carriers in P); holes reduction due to this recombination are supplied by the PD positive terminal. The N $\rightarrow$ P flow of electrons (i. e. the current) is kept constant because of the PD negative terminal.
As for the characteristic quantities for the PN junction, the following mechanisms occur in forward biasing (fig. 1.26):

- the SCR and the charge dipole are reduced;
- the built-in electric field E and, consequently, the built-in potential V_{bi} are reduced;
- the band bending is reduced.

Since the system is no more in thermodinamic equilibrium the Fermi level is no more uniform in the two sides:

[17]It is a treshold voltage beyond which the junction leads sufficiently high currents to be useful in electronics applications. Typical values for silicon are $V_\gamma = 0.5 \div 0.6$ V

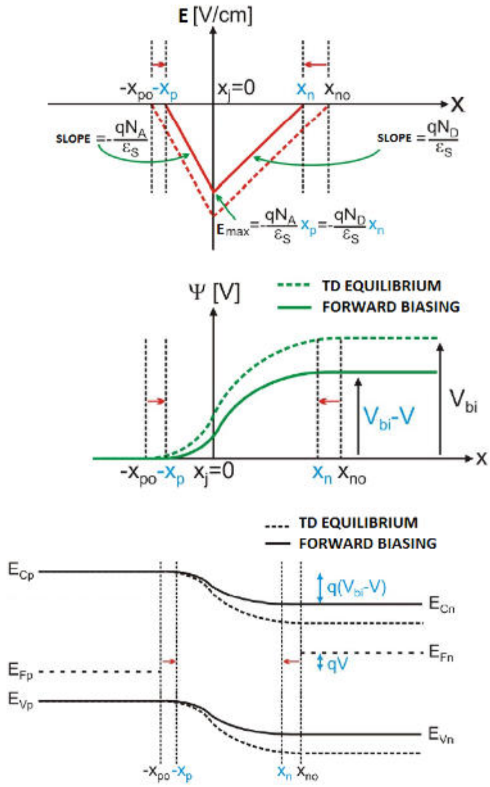

Figure 1.26: Characteristic quantities for the PN junction in forward biasing

$$E_{F_N} - E_{F_P} = qV \tag{1.43}$$

The total current flowing through the junction is described by the Shockley equation:

$$I = I_S \left[exp\left(\frac{qV}{\eta kT}\right) - 1 \right], \tag{1.44}$$

where η is the ideal factor of the diode and is about 1 for germanium and about 2 for silicon; I_S is the inverse saturation current, which describes the diffusion flow of the minority carrier. Because at 25°C temperature kT/q $\sim$ 0,025V, it is clear that in forward biasing for a PD of the order of 0.1V, the 1 can be neglected with respect to the exponential term, so the current increases exponentially with the voltage [9]. Figure 1.27 shows this trend.

Temperature dependence

In terms of current density J[A/μm^2] we have:

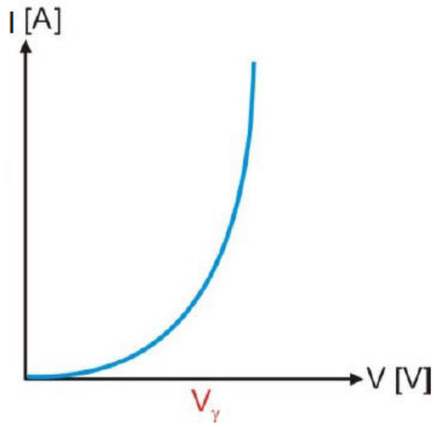

Figure 1.27: Exponential trend of the current as a function of the voltage in a forward biased PN junction

$$J = J_S \cdot exp\left(\frac{qV}{kT}\right). \tag{1.45}$$

Considering only the temperature dependence of the exponential, it might mistakenly infer that J has a negative temperature coefficient (for a fixed V). But in fact the reverse saturation current density J_S has in turn a temperature dependence since it depends on the intrinsic concentration n_i, which have a positive temperature coefficient as we said before:

$$J = CT^{\alpha} \cdot exp\left(\frac{V - V_{G_0}}{V_T}\right), \tag{1.46}$$

where C is a numeric coefficient which takes account of the non temperature dipendent quantities, α = 4- - m with m>0, $V_{G_0} = E_{G_0}$ and $V_T = \frac{kT}{q}$. From this equation it is possible to evaluate the temperature coefficient for the voltage at a fixed current:

$$\frac{dV}{dT} = -\frac{V_{G_0} - V + V_T\alpha}{T}, \tag{1.47}$$

The fact that the voltage (fixed the current) has a a negative temperature coefficient is equal to say that the current (fixed the voltage) has a positive temperature coefficient (fig. 1.28).

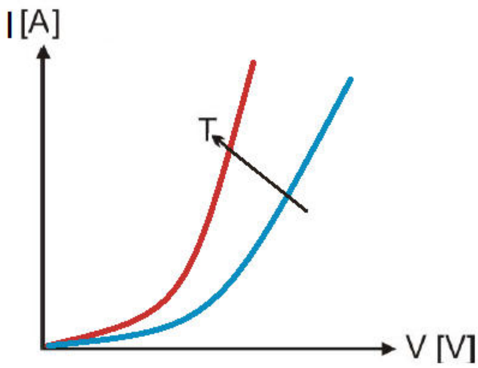

Figure 1.28: Temperature dependence of the current as a function of the voltage in a forward biased PN junction

1.3.8 Reverse Biasing And Impact Ionization Theory

If the N-region of the junction is connected to the positive terminal of a PD and the P-region to the negative terminal, the junction is said to be **reverse biased**. In this condition, the majority carriers, attracted by the PD the terminals, are removed from the metallurgical junction; this results in a SCR enlargement. The voltage applied V_R raises the potential barrier to V_{bi}+ V_R and the electric field within the depletion region increases. The few holes of the N-region are extracted and migrate quickly through the junction towards the P-side. The same happens for the electrons, that migrate from P to N because of the electric field. So there is a minority carriers flux crossing the junction (fig. 1.29); this current, I_S, is the reverse saturation current we have seen before. This current is a constructive parameter and depends on the characteristics of the particular semiconductor material, the nature and concentration of impurities and on the temperature.

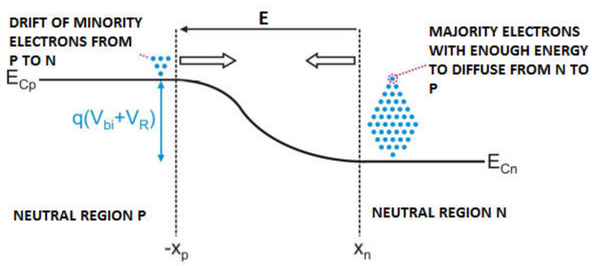

Figure 1.29: Electron drift for the PN junction in reverse biasing

In addition to the saturation current, there is another current due to the thermal generation of electron-hole pairs within the depletion region. Indeed, because of the strong electric field, these charges produced by thermal agitation, rapidly are extracted and migrate to the regions out of the SCR. It is clear that the thermal generation probability increases as the width of the depletion region.
Since the system is no more in thermodinamic equilibrium the Fermi level is no more uniform in the two sides:

$$E_{F_N} - E_{F_P} = -qV_R \tag{1.48}$$

The reverse biased P-N junction is not able to tolerate any entity for V$_R$. For a certain value of V$_R t$ the current between the cathode and the anode undergoes a sudden increase in value, which can lead to the destruction of the component (fig. 1.30). The trigger voltage of this mechanism is called **breakdown voltage** (V$_{BD}$).

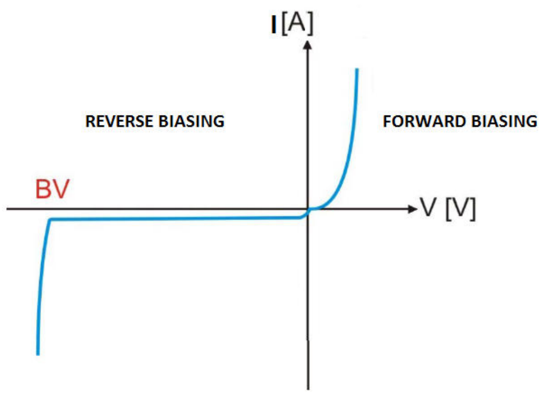

Figure 1.30: Trend of the current as a function of the voltage in a forward and reverse biased PN junction

As for the characteristic quantities for the PN junction, the following mechanisms occur in reverse biasing (fig. 1.31):

- the SCR and the charge dipole are enlarged;
- the built-in electric field E and, consequently, the built-in potential V$_{bi}$ are enlarged;
- the band bending is enlarged.

The physical phenomenon on which is based the breakdown for avalanche multiplication is the **impact ionization**. It is the process by which one energetic charge

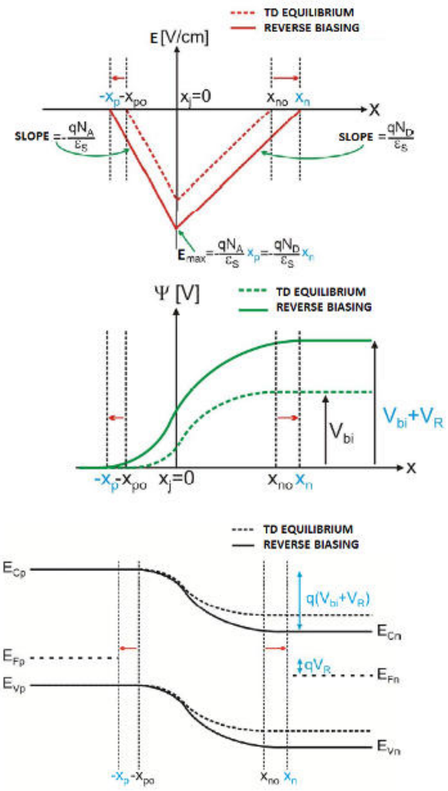

Figure 1.31: Characteristic quantities for the PN junction in reverse biasing

carrier can lose energy by the creation of other charge carriers. In particular, an electron (or hole) with enough kinetic energy can knock a bound electron out of its bound state (in the valence band) and promote it to a state in the conduction band, creating an electron-hole pair.

If V_R is very high, and so the built-in electrical field E, in their mean free path electrons can acquire kinetic energy $> E_G$. Impacting with covalent bonds, they are then able to create free electron-hole pairs, which, in turn, can impact the lattice and create other couples [10]; this results in a so called **avalanche breakdown** (fig. 1.32).

A P-N junction can work in the breakdown regime by means of avalanche multiplication. This mechanism is relevant for this thesis since it is fundamental to the understanding of the operation of avalanche photodiodes (APD) and Silicon Photomultipliers.

The avalanche multiplication phenomenon in semiconductor junctions was studied for the first time by K. G. McKay in 1953, which proposed a model inspirated to the Townsend discharge model [13].

It is possible to define the ionization rate of electrons in a semiconductor junction,

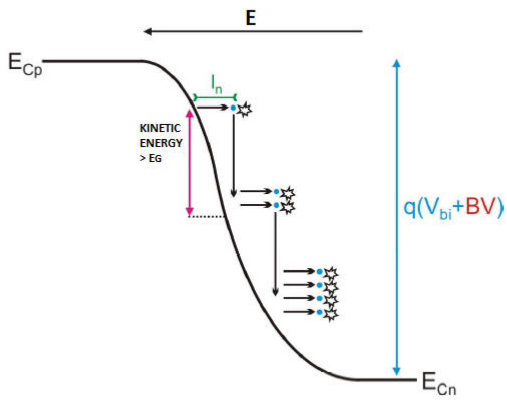

Figure 1.32: Schematic development of a breakdown avalanche

α, as the number of electron-hole pairs per centimeter produced by the electron interaction with the lattice. This coefficient obviously depends on the electron's velocity: $\alpha = \alpha(v_e)$. Similarly is defined the ionization rate for holes, β.
In first approximation, we will consider $\alpha = \beta$. Let us suppose to have a junction whose depletion region has width W, and choose the reference frame as in figure 1.33; n_0 is the initial number of electrons at the edge of the depletion region x = 0.

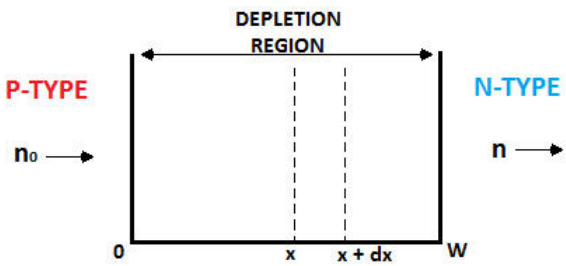

Figure 1.33: Reference frame for the multiplication coefficient calculation

These electrons, while they move through the SCR from x = 0 to x = W, generate more electrons by ionization; if n_1 is the number of electrons generated by ionization between 0 and a certain distance x, the number of electrons generated by ionization between x and x + dx is given by:

$$dn_1 = (n_0 + n_1)\alpha dx = n\alpha dx, \tag{1.49}$$

where n is the total number of electrons collected by the anode. Integrating in the whole depletion region, taking into account that in x = 0 $n_1 = 0$ and in x = W n = $n_0 + n_1$, we have:

$$\int_0^{n-n_0} \frac{dn_1}{n} = \int_0^W \alpha dx, \quad \rightarrow \quad 1 - \frac{n_0}{n} = \int_0^W \alpha dx. \tag{1.50}$$

Multiplication coefficient M is defined as the ratio between the total number of electrons collected after multiplication and the number of initial electrons: M $\equiv \frac{n}{n_0}$. By substitution in the previous equation we obtain:

$$M = \frac{1}{1 - \int_0^W \alpha dx}. \tag{1.51}$$

This is an approximate formula which is obtained by placing $\alpha = \beta$. In fact, the ionization coefficient of holes is smaller than the ionization coefficient of electrons, thus the probability that a hole generates an avalanche is lower with respect to an electron. This affects the multiplication factor, and it is an aspect to take into account in manufacturing detectors which base their operation on the avalanche multiplication.
The ionization rate depends on the speed of carriers which, in turn, is linked to the value of the electric field (through mobility). The ionization rate, therefore, depends on the electric field: $\alpha = \alpha$(E(x)). Equation 1.51, moreover, shows that if the integral in the denominator is equal to 1 then M $\rightarrow \infty$: this means that exists a value of the electric field for which M diverges. This electric field value is the one linked to the breakdown voltage and, when M diverges, the system switches from the avalanche regime to the **Geiger regime**.
The relation between M and the voltage applied to the junction is given by an empiric equation:

$$M = \frac{1}{1 - \left(\frac{V_R}{V_{BD}}\right)^n}, \qquad |V_R| < |V_{BD}| \textit{ for the avalanche regime} \tag{1.52}$$

where n is a coefficient which depends on temperature (typical values for silicon are $2 \div 6$).
Phenomenologically speaking, while the avalanche grows electrons and holes begin to migrate towards the boarders of the SCR, where they are collected. Thus two competing processes occur: generation of carriers for ionization and their recombinations when collected. If the recombination rate is higher than the generation rate, the number of carriers begins to decrease and the avalanche runs out spontaneously. If the electric field is such that the generation rate exceeds the recombination rate, the number of carriers continue to rise and the corresponding current increases exponentially; only effects due to spatial charge distribution may eventually extinguish the avalanche, if they are able to locally reduce the electric field [14].

So finally, in an avalanche junction the applied reverse voltage is lower than the the breakdown voltage and the average number of carriers generated by ionization, $\ll \infty$, is calculated from 1.51; while, in a Geiger junction the reverse voltage applied is higher than the the breakdown voltage and the number of carriers grows exponentially. To make a Geiger junction usable, an external mechanism that allows to turn off the avalanche is mandatory.

1.3.9 Transition Capacitance

The depletion region of a open circuit P-N junction, consists of positive and negative fixed charges at a distance equal to the width W of the SCR. So it is similar to a plane capacitor. Denoting by A the cross section of junction, the total charge in the depletion region is Q = qN_DW_NA in the N side and -Q = -qN_AW_PA in the P side. The width of the SCR is a function of V_{bi}. When the junction is polarized, V_{bi} changes, then W changes, and consequently there is a charge accumulation.
It is useful to define a incremental capacity, which relates the voltage increase with the the accumulated charge increase. It is defined as the **transition capacitance** and is given by:

$$C_T \equiv \frac{dQ}{dV}. \tag{1.53}$$

For an open circuit junction the width of the SCR is given by:

$$W = \sqrt{\frac{2\epsilon V_{bi}(N_A + N_D)}{qN_AN_D}}. \tag{1.54}$$

If an external PD V occurs it becomes:

$$W = \sqrt{\frac{2\epsilon(V_{bi} - V)(N_A + N_D)}{qN_AN_D}}. \tag{1.55}$$

So the transition capacitance can be obtained as a function of dopant concentrations:

$$C_T = \frac{\epsilon A}{W} = \frac{A}{\sqrt{(V_{bi} - V)}}\sqrt{\frac{qN_AN_D}{2\epsilon(N_A + N_D)}}. \tag{1.56}$$

Notice that if V<0 (reverse biasing case) W increases and C_T decreases (typ. $\sim$ pF)

1.4 Junctions as Radiation Detectors

A simple P-N junction can operate as a radiation detector, if at the two sides are applied two metal contacts: the radiation that passes through the depletion region may transfer enough energy to the material to generate electron-hole pairs. The drift of these carriers under the action of the electric field generates a current. This current lasts as long as carriers reach the limit of the depletion region, when they recombine on the electrodes.
The average energy required for a ionizing particle to create a pair is $\sim$ 3 eV in silicon, and weakly dependent on temperature and on the nature of incident radiations. Notice that this energy is much greater than the bandgap (1.12 eV for silicon), so most of it is spent on vibrations of the crystal lattice.
However, using a non-biased junction as a detector is not the ideal solution.
First, the electric field in the depletion region (also called active zone when used as detectors) is not intense enough to ensure an efficient collection of carriers, and thus a part of them is lost for recombination before it can reach the electrodes. Furthermore, the active region is small.
This creates two issues: only low energy particles can stay in the material (and this limits the measurement possibilities), and it is difficult to produce enough pairs to form a signal that can be distinguished from noise (due to thermal generation of pairs within the SCR; the high conductivity of the neutral regions favors the passage of this background current).
This results in an inefficient, very noisy detector which is also hard to implement in an electronic amplification circuit.
Reverse biased junction is the solution because of the enlargement of the active zone (in silicon, $\sim$5mm for a reverse biased junction versus $\sim 75\mu$m for a non-biased junction). Because of the recombination, in the depletion region the intrinsic concentration of the charge carriers is equal to that of the intrinsic silicon (1.45 x 10^{10} cm^{-3} at T=300K) which involves a very high resistivity (2.5 x 10^5 $\Omega \cdot cm$). The high resistivity causes a higher voltage drop across the depletion region and an increase of the electric field inside it ($E \geq 10^5$ V/cm). This results in an increase of the impact ionization coefficient which leads to the production of an output current signal large enough to not need a particularly complex additional external amplifier (fig. 1.34).
Thanks to the many advantages they offer (low average energy required for pairs production, small size, low costs) in the 50s semiconductors are been widely used in the detection of radiation, both ionizing (beta, fast electrons and heavy ions) and electromagnetic (photons) [11].
In the following sections we will describe the most used configurations.

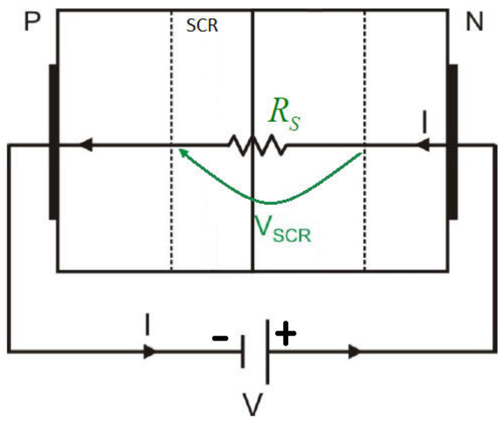

Figure 1.34: Resisitivity of the depletion region in a reverse biased p-n junction

1.5 P$^+$-N, P-N$^+$ Junctions and Photodiodes

In the P-N$^+$ configuration (fig. 1.35), the N-side is much more doped than the P-side, so the depletion region is almost all located in the P-side.

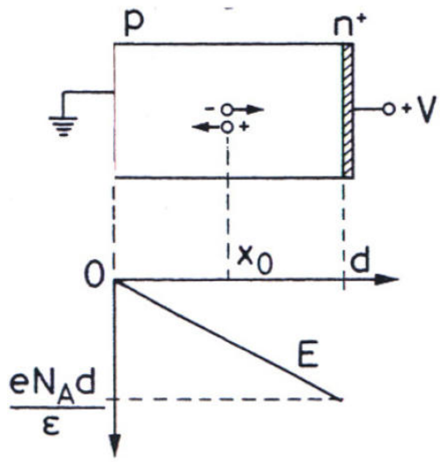

Figure 1.35: P-N$^+$ junction with the electric field trend into the depletion region [12]

The supply voltage is selected so that the active area fully covers the P side. In this case the detector is completely depleted, with a remarkable reduction of noise (since there are no more neutral regions).
A radiation impinging the depletion region creates electron-hole pairs. The charges migrate under the action of the electric field inducing a variation in the electrodes charge. This variation is given by:

$$dQ = \frac{q}{d}dx, \tag{1.57}$$

where dx is the distance traveled and d is the distance between electrodes. Appropriately integrating this quantity, it is possible to calculate the total charge collected on the two electrodes for one electron and one hole:

$$Q_{TOT} = -\frac{q}{W}x_0\left(1 - \frac{W}{x_0}\right) + \frac{q}{W}x_0, \quad \rightarrow \quad Q_{TOT} = q, \tag{1.58}$$

and not 2q as expected (Ramo's law). The total charge collected after the passage of a particle depends on the number of pairs created, on the particle trajectory and on variations of the electric field within the active area; it is therefore very difficult to calculate.
For the P$^+$-N type similar considerations hold and lead to the same result.
Very often, this second type is used as the photodetector, and it is called a **photodiode** (fig. 1.36). Light pours in the detector through the P$^+$ side, which for this reason is provided with a no-reflecting window (typically Si_3N_4 is used as window material) to reduce the loss of photons by reflection.

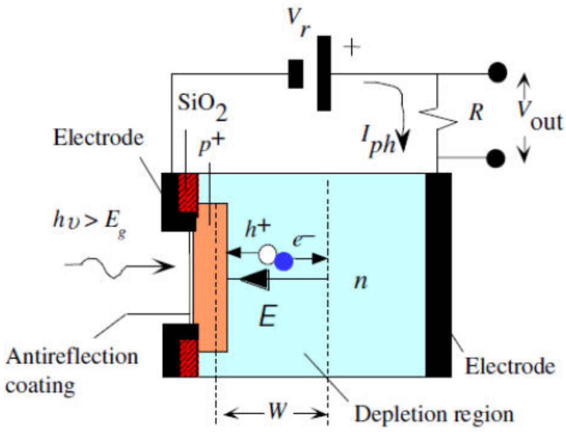

Figure 1.36: Schematic view of a photodiode

Then photons are absorbed and, to produce electron-hole pairs, their energy must be greater than E_G, so $h\nu = \frac{hc}{\lambda} > E_G$.
This costraint introduces a cutoff wavelength, above which the photons are no longer absorbed by the detector:

$$\lambda_G(\mu m) = \frac{1.24\,\mu m\,eV}{E_G\,eV} \tag{1.59}$$

For silicon, E_G= 1.12eV and therefore would be $\lambda_G = 1.11\mu$m. But in fact, since the silicon is a indirect bandgap semiconductor, the photon absorption must occur

even through the lattice vibrations. If θ is the frequency of lattice vibrations and the phonon energy is hθ, the photon will be absorbed only if $h\nu > E_G \pm h\theta$ holds. However, usually θ is neglectet since, in silicon, it is very small (<0.1eV).
Another important feature in photodiodes is the material's absorption coefficient: when the photons penetrate the detector, their number decreases exponentially with time. Therefore, light intensity at a distance x from the semiconductor's surface is given by:

$$I(x) = I_0 exp(-\alpha x), \tag{1.60}$$

where α is the absorption coefficient, a parameter which depends on the particular material. Its inverse is called "penetration depth" and is the distance within 63% of incident photons are absorbed. In manufacturing a photodiode, it must be chosen a material whose penetration depth is of the same size of the depletion region in correspondence to the wavelength to be detected. Indeed, if the absorption coefficient is too large, photons are absorbed in the P^+ layer where there is no electric field and then the pairs generated quickly recombine. If, instead, the absorption coefficient is too small, a few photons are absorbed in the depletion region and thus a few pairs are generated, this results in a small signal that cannot be distinguished from noise.
In particular, silicon is an excellent visible light detector.
For the photodiodes quantum efficiency QE is defined the ratio of the number of pairs produced and collected and the number of incident photons[18]:

$$QE = \frac{\textit{e-h pairs}}{\textit{Incident photons}} < 1. \tag{1.61}$$

Another fundamental quantity is the spectral responsivity of the photodiode, defined as the relationship between the photocurrent generated and the incident optical power. Figure 1.37 shows the plot of the spectral response of a silicon photodiode as a function of the wavelength, and is compared with that of an ideal photodiode with QE = 1.

[18] QE is always less than 1 because of carriers recombination, photon reflections on the detector's surface and effects due to α

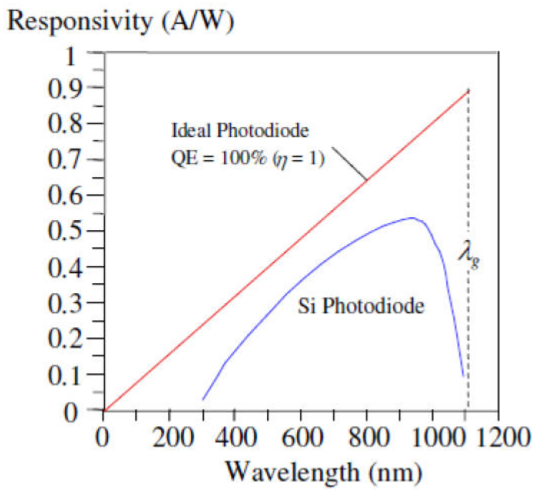

Figure 1.37: Comparison between the spectral response of a realistic photodiode and an ideal photodiode

Advantages compared to PMTs:

- Excellent linearity of output current as a function of incident light;
- Spectral response from 190 nm to 1100 nm (silicon), longer wavelengths with other semiconductor materials;
- Low noise;
- Ruggedized to mechanical stress;
- Low cost;
- Compact and light weight;
- Long lifetime;
- High quantum efficiency (typically 60 $\div$ 80%);
- No high voltage required.

Disadvantages compared to PMTs:

- Small area;
- No internal gain;
- Much lower overall sensitivity;

- Photon counting only possible with specially designed, usually cooled photodiodes, with special electronic circuits;
- Response time for many designs is slower;
- Latent effects.

1.6 Si(Li) And P-I-N Detectors

In some applications, the detection of long wavelength photons, the width of a standard photodiode the depletion region is often not enough. A different configuration is used, consisting of two high doped layers separated by an intrinsic layer. Usually this structures are obtained by treating silicon doped layers with lithium atoms by means of the doping for overcompensation technique (therefore the detector is said Si(Li): lithium drifted silicon).
The resulting P-N junction is then reverse biased and brought to high temperature to raise the mobility of donor atoms: driven by the electric field, donors move slowly in the P layer and their concentration increases until it is equal to acceptors concentration (this operation is also called compensation, and the material obtained is called a compensated semiconductor).

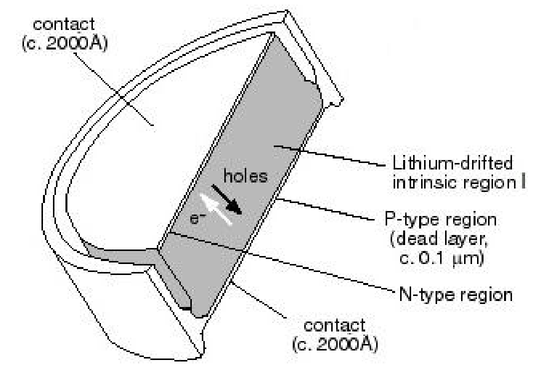

Figure 1.38: Schematic view of a Si(Li) detector

The result of this process is shown in figure 1.38, a large compensated material layer (very similar to a intrinsic semiconductor) is located between a N^+ layer, (obtained by overcompensation) which is used as electrode, and P, (the non compensated layer) on which is deposited a metal layer to make the second electrode.
In the ideal case there is no space charge density within the compensated layer I, therefore, its internal electric field is constant; in the absence of polarization the contact potential value is fixed to E_{bi}. When a reverse voltage is applied the electric field becomes:

$$E = E_{bi} + \frac{V_R}{W}, \tag{1.62}$$

and it continues to be constant throughout the region, unlike the case of simple P-N junction. Depletion region of N^+ and P layers can be neglected since these are very thin with respect to I, then the width of the active area is equal to the width of I layer.
The transition capacitance does not depend on the applied voltage, unlike the P-N junction.
The mechanism for particle detection is the same as in the P-N junction: the radiation penetrates into the compensated layer producing pairs which are separated by the electric field and collected at the electrodes.
The difference is in the width of the active region (even 10 mm) that makes this device very suitable for accurate energy measurements and detection of beta particles.
Semiconductors in such a configuration are used as photodetectors. They are called **P-I-N photodiodes** (fig. 1.39). In this case also the P layer is highly doped and on it is placed a window coated with anti-reflection material, through which light penetrates. The wide depletion region enables these photodetectors to obtain a much more high quantum efficiency; but, of course, carriers generated in the I layer have to travel a greater distance before they reach the electrodes. This makes the P-I-N photodiodes slower compared to P-N junction detectors.

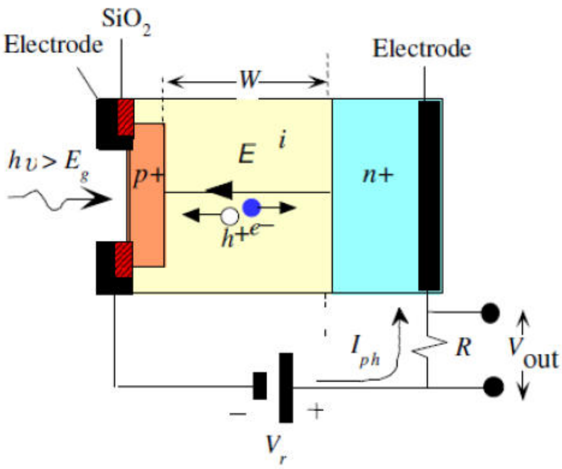

Figure 1.39: Schematic view of a P-I-N photodiode

Avantages and limits of this device with respect to PMTs are similar to P-N junction detectors.
The most serious defect of P-I-N and P-N junction photodiodes is that the pho-

tocurrent produced is very small; this necessitates the use of a complex front end electronics to amplify these signals, which is often undesirable.
A huge step forward in the development of semiconductor detectors was the idea to make P-N junctions work in their breakdown regime, building structures in which electrons and holes during their drift are accelerated to the point that they can trigger a Geiger avalanche.
The use of a semiconductor detector with an internal gain has two huge advantages with respect P-I-N and P-N junction: remarkably increases the charge collection, and then the signal amplitude, so no amplification circuit is needed, and have a faster response.
Such devices are called **SPAD** (single-photon avalanche diode also known as **G-APD**) and will be described in detail in next sections, being the basic element of the **Silicon Photomultiplier**, that is the core of this thesis.

1.7 Avalanche Photodiodes: APDs

APDs are high-speed and high sensitivity silicon devices. These features make APDs suitable for a wide variety of applications requiring a high sensitivity also in low level light detection [18]. Such a device consists of a pn junction with a reverse bias voltage which allows to activate the internal avalanche mechanism that determines the gain. The middle panel of figure 1.40 shows schematically the typical p^+ - p - n construction of an APD. The structure is externally reverse-biased by V_{bias}, which, together with the intrinsic electric field of the p-n junction, creates an electric field whose strength profile is schematically shown in the top panel. The field is maximum at the metallurgical junction.
Referring to the figure, light is incident on the p^+ side. If the energy of light is greater than the band gap energy E_G of the semiconductor used to manufacture the APD (typically silicon with E_G = 1.1 eV), an intrinsic photoelectric effect can occur producing e-h pairs. Owing to its indirect band structure, the photon absorption process in silicon also involves a phonon[19]. The characteristic depth of photon absorption depends on the type of the semiconductor and the wavelength of light. The bottom panel of figure 1.40 shows schematically that the flux Φ of red photons attenuates less with depth compared to the flux of blue photons. More specifically, photon flux $\Phi(\lambda, z)$ as a function of depth z is given by the following equation

$$\Phi(\lambda, z) = \Phi(\lambda, 0) \cdot e^{-\alpha z}. \tag{1.63}$$

[19] A quantized lattice vibration

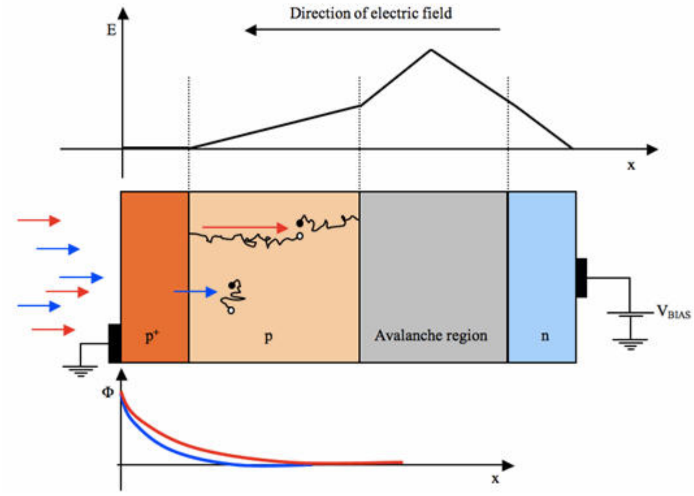

Figure 1.40: Structure and operation of asingle APD cell, colored arrows represent photons

Here, $\Phi(\lambda, 0)$ is the incident flux and α is the absorption coefficient, which depends on the type of the material and the wavelength of light (fig. 1.41).

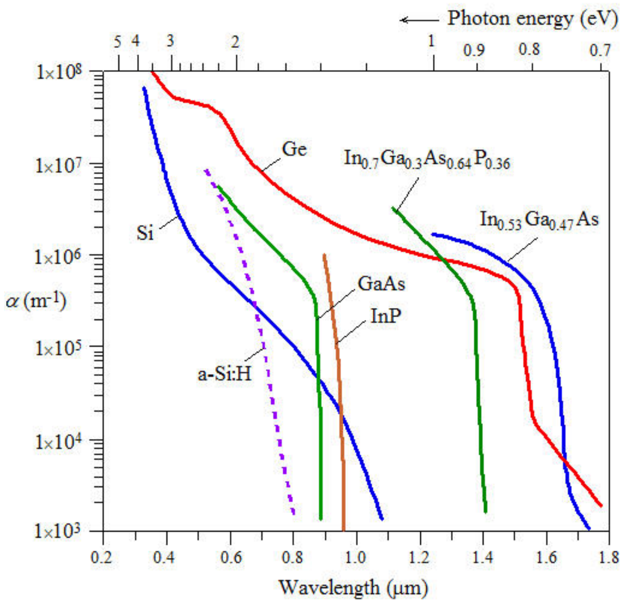

Figure 1.41: Absorption coefficient as a function of wavelength of light (bottom abscissa) or energy (top abscissa) for several semiconductors

Equation 1.63 shows that the production of e-h pairs decreases exponentially with depth; 63% of the incident photons are absorbed over a distance $\delta = \frac{1}{\alpha}$, known as the penetration depth. In the case of silicon, δ is approximately 0.08 μm and 3 μm at $\lambda = 400$ nm and $\lambda = 600$ nm, respectively. As λ increases to the threshold value $\lambda_{th} = \frac{hc}{E_G}$, $\alpha \Rightarrow 0$ (or $\delta \Rightarrow \infty$) and the material becomes progressively more transparent to the incoming radiation. However, as λ decreases, $\alpha \Rightarrow \infty$ (or $\delta \Rightarrow 0$) and the incoming radiation is absorbed near the surface. The dependence of α with respect to λ is a crucial parameter in the design of an APD.
If an e-h pair is produced in a heavily doped p^+ region where the electric field is very weak, the pair is likely to recombine. For indirect band gap semiconductors like silicon, the recombination is mostly non-radiative and requires a phonon. The need for a phonon makes the lifetime of the pair longer than that for a pair produced in a direct band gap semiconductor (e.g., GaAs). Suppose that as a result of light illumination, an e-h pair forms close to or in the depletion region where the electric field is strong enough to separate the pair and make the electron move toward the n region and the hole toward the p^+ region (fig. 1.40). In the depletion region, the likelihood of e-h recombination is extremely small because the region lacks mobile charge carriers and, therefore, the injection produces an electrical signal in the circuit containing the detector. Light has been detected!
The quantum efficiency, $\eta(\lambda)$, is defined as the ratio of the number of photo-generated e-h pairs per unit time, $n_e - h$, that produce an electrical signal to the number of incident photons on a photo-sensitive surface per unit time, n_λ.

$$\eta(\lambda) = \frac{n_e - h}{n_\lambda}. \tag{1.64}$$

The rate at which the photo-produced charge carriers enter the depletion region is the photocurrent I_{ph} and is given by the following equation:

$$I_{ph} = \frac{e \cdot \eta \cdot \lambda \cdot P_0}{hc}. \tag{1.65}$$

Here, P_0 is the incident light power (assumed monochromatic light), e is the fundamental charge, h is Planck's constant, and c is the vacuum speed of light. The magnitude of the current flowing through the APD, I_{APD}, depends on I_{ph} and on the strength of the electric field in the avalanche region. The field determines the degree of impact ionization in the avalanche region and, therefore, the gain M making $I_{APD} = MxI_{ph}$. Because the strength of the electric field depends on V_{bias}, a relationship exists between M and V_{bias}. This relationship is one of the most important characteristics of an APD, and it is schematically shown in figure 1.42.

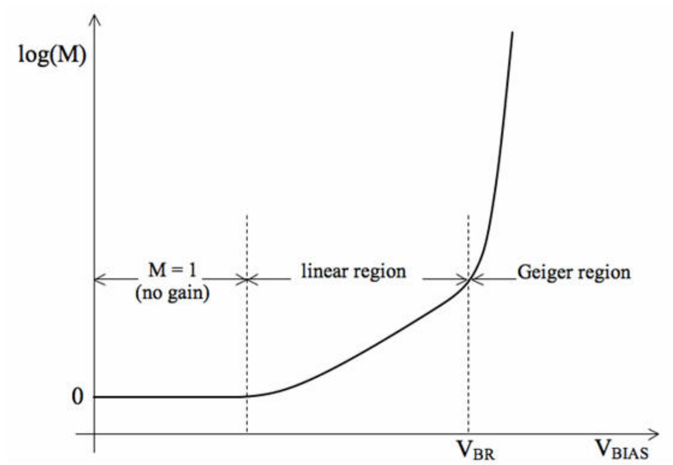

Figure 1.42: Gain versus reverse bias voltage for a hypothetical APD

There are three distinct regions on the log(M) versus V_{bias} plot. "No gain" or M = 1 is the characteristic of the first region. Here, $I_{APD} = I_{ph}$ and the APD operates as a photodiode. The electric field in the avalanche region is too weak to energize charge carriers to the minimum energy required for impact ionization of the lattice atoms.

In the linear region, log(M) is linearly proportional to V_{bias}. Here, $M > 1$ because the charge carrier injected into the avalanche region gains enough kinetic energy to ionize a lattice atom. Therefore, one carrier (say an electron) becomes three after ionization: two electrons and one hole. These can now again be energized to cause further ionization events, an avalanche ensues. In the linear region, the avalanche eventually ceases; the electrons and holes produced by impact ionization are collected at the electrodes and their number is M, or the gain.

The likelihood of impact ionization depends on the strength of the electric field. Let α and β be ionization coefficients representing the number of ionization events per unit length for electrons and holes, respectively. In the case of silicon (Si), $\alpha > \beta$ for any value of E implying that impact ionization due to an electron is more likely to occur than impact ionization due to a hole. Let $k \equiv \frac{\alpha}{\beta}$ (impact ionization ratio); for Si, k $\sim$ 0.01 for E $\sim$ 1.5 x 10^5 V/cm and about 0.4 for E $\sim$ 6.0 x 10^5 V/cm , which means that the likelihood of impact ionization by electrons and holes converge with increasing strength of E (fig. 1.43).

The third region of figure 1.42 will be explored in the next section.

In priciple the higher is the reverse bias voltage, the higher is the internal gain. However, the APD has a maximum gain whose value depends on the photocurrent. As the internal gain introduces only a multiplication factor, the output signal will be proportional to the amount of light entering the Silicon bulk.

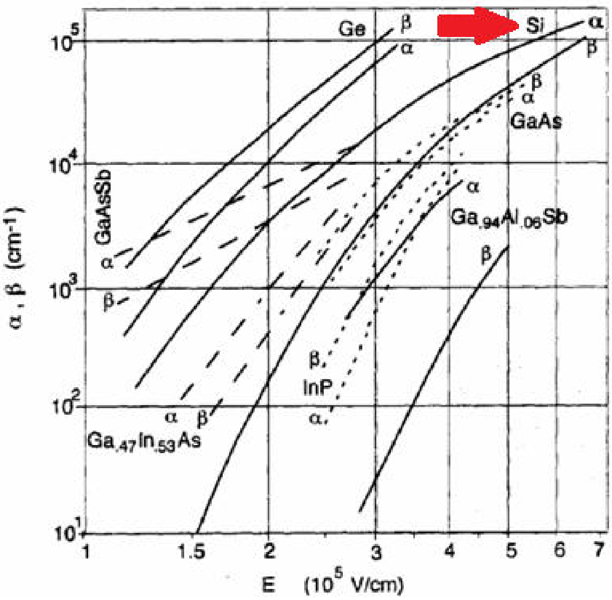

Figure 1.43: Ionization coefficients as a function of electric field strength for several semiconductors

Because of their internal amplification, APDs have many interesting features, but also several drawbacks:

- Low gain ($\sim$ 100) due to a limit on the photocurrent. If the reverse bias voltage is increased too much, a voltage drop occurs because the current flows through the device internal resistance, producing a decrease in the voltage applied to the avalanche layer; this results in an output photocurrent not proportional to the amount of incident light.

- Gain decreases as the environment temperature increases, because of thermal vibrations in the crystal lattice which prevent ionization electrons to travel a mean free path that they can acquire enough energy to trigger an avalanche.

- APDs generates noise in the multiplication process, there are some statistical fluctuations due to non-uniformities in the ionization. These fluctuations increase with gain. Since the gain exhibits a dependence on the energy of the incoming photon, and thus from its wavelenght, the excess noise differs according to the incident light wavelenght. At the same time, the photocurrent generated by a light pulse is also amplified by the gain. All these facts are clear indication that best signal-to-noise ratio exists only for certain gain values.

1.8 Silicon Photomultipliers: SiPMs

The silicon photomultiplier (fig. 1.44), often called "SiPM" (or even G-APD or MPPC in the Hamamatsu nomenclature) in literature, is a solid state radiation detector with extremely high sensitivity, high efficiency, and very low time jitter, capable of detecting individual photons. It is based on reversed biased p/n diodes, it can directly detect light from near ultra violet to near infrared, and it is employed in all those applications where low light/radiation level must be measured and quantified with high precision.

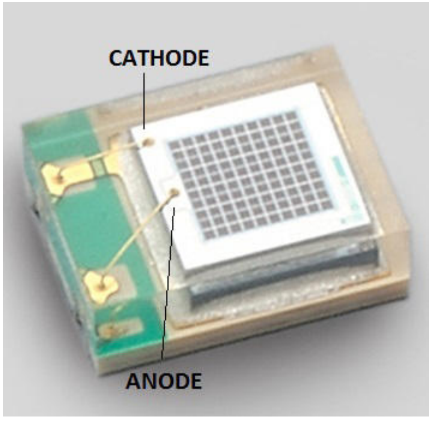

Figure 1.44: Picture of a Hamamatsu 1x1 SiPM in a SMD package

Light is made of photons (quanta of light). SiPMs are designed to have high gain and high detection efficiency so that even a single photon impinging on a SiPM pixel can be detected producing an output current pulse with a very low time jitter (<100 ps). The structure of a SiPM allows "parallel" photon detection, meaning that more photons can be detected at the same time enabling photon counting.
Indeed, the geometrical structure of a SiPM consists of a rectangular array, or a matrix, of small-sized sensitive elements called micro-cells (or pixels) all identical and connected in parallel (fig. 1.45). Each micro-cell is a Geiger-Mode avalanche photo-diode (GM-APD) working beyond the breakdown voltage (V_{BD}) and it integrates a resistor for passive quenching Rq.
An external power source reverse-biases the array to a voltage V_{bias} that is up to a few volts above the breakdown voltage of a G-APD. An important characteristic quantity for SiPMs is the breakdown voltage (V_{BD}), that is the minimum (reverse) bias voltage that leads to self-sustaining avalanche multiplication in GM-APDs and, depending on the design of a pixel, V_{BD} is in the 30 V to 70 V range. In other words, it is the minimum bias for which a current output pulse can be obtained.
However, for V_{bias}=V_{BD} both the detection efficiency and the gain of SiPMs are

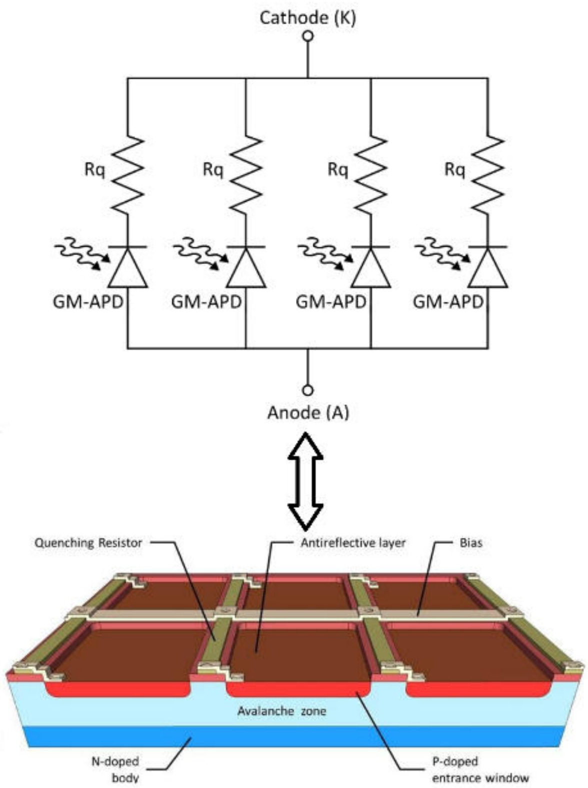

Figure 1.45: Detail of the matrix of microcells and schematic of the parallel arrangement of GM-APDs with series quenching resistor in a SiPM

(by definition) still null as we will see later. Only for $V_{bias} > V_{BD}$ output current pulses are actually observed. The difference between V_{bias} and V_{BD} is commonly referred to as overvoltage (V_{OV}), which is one of the most important operational parameters of an SiPM. By definition:

$$V_{OV} = V_{bias} - V_{BD}. \tag{1.66}$$

In principle, the higher the overvoltage, the higher the SiPM performances. In reality, since the detection efficiency tends to saturate with V_{OV} while the noise keeps on increasing (even more than linearly) with V_{OV}, there exist an upper limit to the optimum SiPM bias voltage.

1.8.1 SiPM's Architecture

Figure 1.46 illustrate a common architecture of a G-APD array. The accompanying figure 1.47 shows schematically the distribution of the dopant ions or space charge

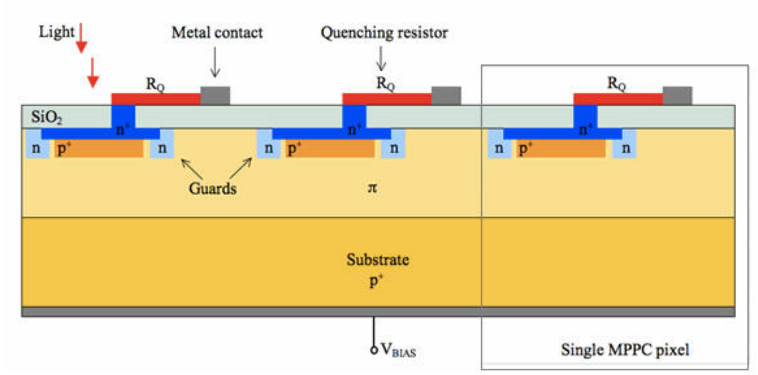

Figure 1.46: Architecture of a silicon photomultiplier (side view). The depicted structure of a single pixel is known as "reach-through" structure, popular with manufacturers

(left panel) and the resulting strength of the electric field (right panel) as a function of depth.

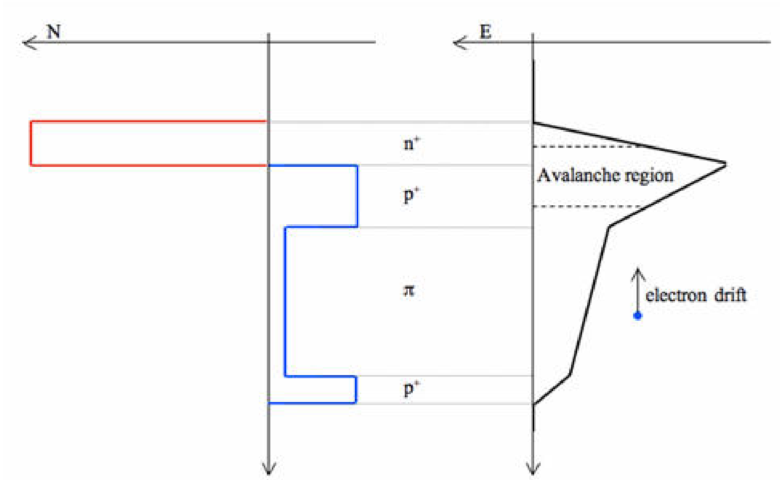

Figure 1.47: Schematic distribution of dopant ions (left) and the resulting electric field (right) for a pixel in the structure shown above

Following the direction of light (red arrows in the leftmost pixel of figure 1.46) they first encountered a very thin (typ. $\sim$10 nm) anti-reflection coating. The coating improves light transmittance to the next layer, a transparent silicon dioxide (SiO_2), which acts as the window and an insulation between the metal contacts above and semiconductor below. A typical thickness of the insulation is $\sim$0.15 μm. Further below, there is a heavily doped n^+ layer, which is connected to the metal contact above through the quenching resistor Rq (made of polysilicon). The thickness

of the n^+ layer ranges from 0.1 μm to 1.5 μm. Immediately below, there is a heavily doped p^+ layer with a typical thickness of few μm. A depletion region where conditions for an avalanche can exist forms at the junction of the n^+ and p^+ layers. The width of the depletion region depends on the applied V_{bias}; for Geiger mode operation, it is $\sim$1 μm.
In this "reach through" architecture, a photon creates an e-h pair in the thick (typ. $\sim$300 μm) and lightly doped π layer. As figure 1.47 shows, the electric field in this region can separate the pair and direct the electron towards the depletion region and the hole toward the substrate, a thin ($\sim$3 μm) p^+ layer that makes an ohmic contact with the metal contact below. Upon reaching the depletion region, the electron can initiate an avalanche, while the hole upon reaching the metal contact cancels with an electron coming from the metal contact.
The area of a pixel that is sensitive to light is smaller than its geometrical area. The ratio of the two is known as the fill factor, FF. The values of FF range from about 30% to 80%. A SiPM is a square array of pixels with the number of pixels ranging from 100 (10 x 10) to 14400 (120 x 120). The typical geometrical areas of the pixels (in μm^2) are 25 x 25, 50 x 50, and 100 x 100. Multiplying the geometrical area of a pixel by the number of pixels yields the total geometrical area of the detector; two values are typical: 1 x 1 mm^2 and 3 x 3 mm^2. Multiplying the geometrical area by the appropriate fill factor gives the total light-sensitive area of the detector.

1.8.2 Physics Behind G-APD Operation

As we said previously, a G-APD is an APD (whose principle of operation is widely explained before) working in Geiger mode.
When a single photon strikes and penetrates a pixel, the photon can excite an electron into the conduction band and thus create a mobile electron-hole (e-h) pair. The internal electric field separates the pair and directs the electron (or hole) into the depletion region (or avalanche region) where, through impact ionization, the charge carrier initiates a current avalanche. As the current builds up, the voltage on Rq increases, whereas the voltage on the APD decreases. The lower voltage on the APD reduces the probability of impact ionization; thus, the current avalanche reaches a maximum and then declines (or it is being quenched!). The resulting signal is a fast current pulse with a rise time of $\sim$1 ns, a peak value proportional to $\frac{V_{OV}}{Rq}$, and a fall-off time on the order of tens of ns. In the fall-off phase, the voltage on the APD increases reaching the pre-avalanche value once the avalanche is completely quenched. An avalanche can produce a number of additional e-h pairs (that is the device's gain M) depending on V_{OV} equal to 10^5 to 10^6. If the same pixel absorbs two or more photons simultaneously, the resulting current pulse has the same amplitude and duration as that due to a single photon. However, if distinct pixels absorb photons simultaneously, the resulting pulse is

a superposition of the single-photon pulses; its amplitude is proportional to the number of independently "fired" pixels.
The main difference between APDs and G-APDs is the fact that the output signal of a G-APD is not proportional to the amount of input light. Indeed we are in the third region of figure 1.42, where the avalanche caused by injection of a single charge carrier does not stop, it is self-sustained. As a result, a current flows through the G-APD and its value depends on the overvoltage, V_{OV}. The steepness of the curve in this region implies that the magnitude of the current is very sensitive to V_{OV}. The strong electric field in the avalanche region maintains e-h plasma where both electrons and holes comparably ionize the lattice atoms (i.e. $\alpha \sim \beta$). In a steady state, the number of newly created pairs is equal to the number of pairs collected at the electrodes. If it is desired to extinguish the avalanche, V_{bias} must be reduced to at least V_{BD}; doing so "quenches" the avalanche.

1.8.3 Operation Principles

The operation principle of a SiPM can be modeled by means of the equivalent circuit of a GM-APD (shown in fig. 1.48).

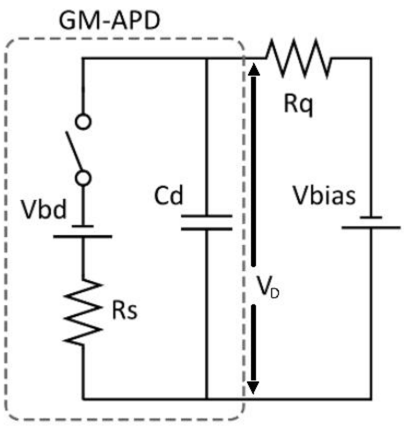

Figure 1.48: The equivalent circuit of a GM-APD with series quenching resistor and external bias. The region of the circuit delineated by the dashed rectangle represents an APD operating in Geiger mode. The switch is in the OFF position when the APD is in the "ready" state, while it goes to the ON state the instant a charge initiates an avalanche. So the switch models the turn-on (photon absorptionor dark event) and turn-off (quenching) probabilities

Cd (typ. $\sim 0.1pF$) is the junction capacitance in reverse bias, Rs (typ. $\sim 1k\Omega$) models the equivalent RC circuit resistance that takes account of the characteristic time needed for the signal creation, Rq (typ. $\sim 150k\Omega$) is the quenching resistor

(Rq $\gg$ Rs) and the switch models the ionization event.
The externally applied V_{bias} is greater than V_{BD} putting the APD in Geiger mode. In series with the APD and V_{bias} is Rq and, at any instant of time, the diode current is given by:

$$i(t) = \frac{V_{bias} - V_D}{Rq}. \tag{1.67}$$

There are three fundamental operation modes in a GM-APD: quiescent mode and recovery phase, when the circuit is in the OFF condition, discharge phase, when the circuit is in the ON condition.

OFF Condition

In quiescent mode, the diode is reversed biased to $V_{bias} = V_{BD} + V_{OV}$. The OFF condition is characterized as follows (fig. 1.49):

- the switch is open (no ionization event occurs);
- the junction capacitance Cd is fully charged to the voltage V_{bias}
- no current flowing in the diode since $V_D = V_{bias} \rightarrow$ i(t) = 0 by equation 1.67;

The voltage V_D creates an electric field in the depletion region that is strong enough to initiate a self-sustained avalanche if a charge carrier is injected into the region.

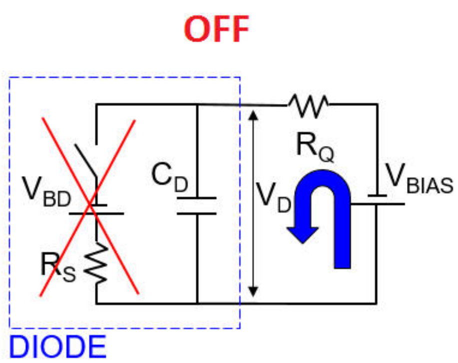

Figure 1.49: The equivalent circuit of a GM-APD in the OFF condition

ON Condition

In the discharge phase the ionization occurs at the time t_i. The ON condition is characterized as follows (fig. 1.50):

- the switch is closed;
- Cd discharges to V_{BD} through the fictive resistor Rs, between t_i and t_{max}, with the characteristic time constant $\tau \sim Rs \cdot Cd$ (typ. $\sim 100ps$);
- the diode current grows to:

$$I_{MAX} = \frac{V_{bias} - V_{BD}}{Rq + Rs}. \tag{1.68}$$

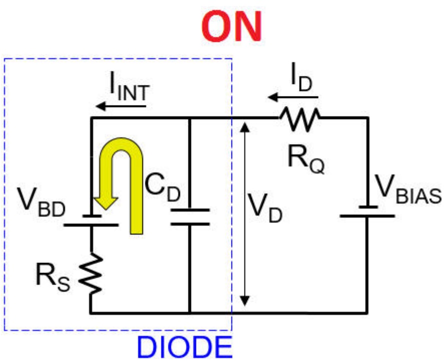

Figure 1.50: The equivalent circuit of a GM-APD in the ON condition

OFF Condition Again

The voltage V_D during the discharge decreases and approaches an asymptotic value given by the following equation[20]:

$$V_D = V_{bias} - \frac{Rq(V_{bias} - V_{BD})}{Rq + Rs} = V_{bias} - \frac{V_{OV}}{1 + \frac{Rs}{Rq}}. \tag{1.69}$$

As V_D decreases, the electric field in the depletion region becomes too weak to maintain Geiger mode and the self-sustained avalanche it's been quenched. This is the **recovery phase** characterized as follows:

- the switch goes open;

[20]Since Rq $\gg$ Rs, the equation shows that V_D tends to V_{BD}

- Cd recharges from V_{BD} to V_{bias} through Rq, for times greater than t_{max}, with the characteristic time constant $\tau \sim Rq \cdot Cd$ (typ. $\sim$ 15 ns);
- the diode current decreases to $\sim$ 0 A.

At the end of the charging process, the APD is in the "ready" state again. Because $Rs \cdot Cd \ll Rq \cdot Cd$, the current rises more steeply before t_{max} then it falls off after t_{max}. Thus, the output current pulse has the characteristic asymmetric shape depicted in figure 1.51.

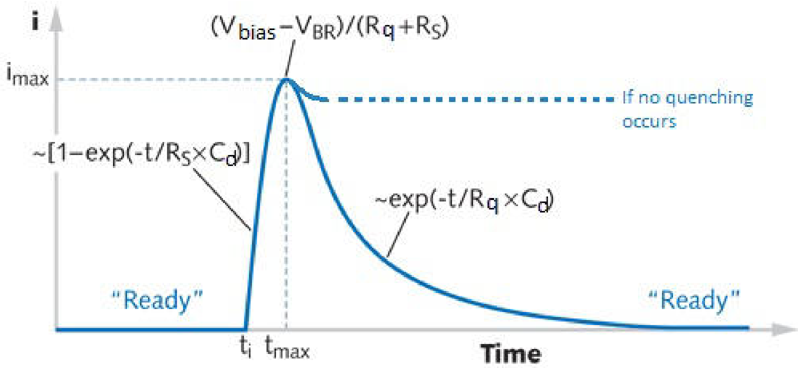

Figure 1.51: Current pulse produced by a micro-cell in response to photon absorption (single-cell signal), its amplitude is defined to be 1 p.e.

An integral of i(t) with respect to time from t_i to infinity is the area under this curve, which equals the net charge Q produced in the avalanche. A detailed analysis yields the following:

$$Q = Cd \cdot (V_{bias} - V_{BD}). \tag{1.70}$$

Since the charge Q is due to a single charge injected into the avalanche region, the gain M for this process can be defined by the following equation:

$$M \equiv \frac{Q}{e}. \tag{1.71}$$

For a fully-depleted junction, Cd is constant with respect to the applied voltage and, thus, equation above shows that M is linearly proportional to $V_{bias} - V_{BD} = V_{OV}$. The typical values of M range from 10^5 to 10^6. If more than one pixel developed an avalanche at the time t_i, the total charge generated by an SiPM is the following:

$$Q_{out} = N_f \cdot Q = N_f \cdot Cd \cdot (V_{bias} - V_{BD}). \tag{1.72}$$

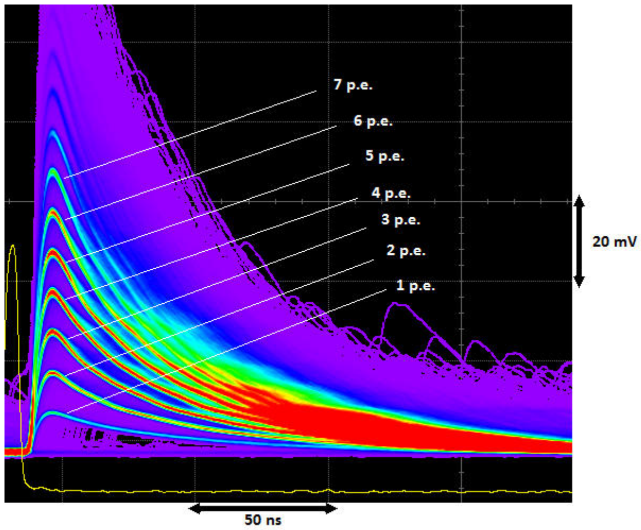

Figure 1.52: Waveforms for Hamamatsu S13360-4929 SiPM producing signal when 1, 2, 3, ... pixels fired simultaneously in response to low incoming light. The waveforms are for gain M = 1.8 x 10^6 and 20x linear amplifier, acquired with the Teledine LeCroy serial data analyzer mod. SDA 760Zi-A

Here, N_f is the number of pixels that nearly simultaneously "fired" or developed avalanches.
Figure 1.52 shows oscilloscope traces of waveforms produced by a SiPM in response to low-intensity light ($\sim$ 40 incident photons). From bottom up, the waveforms correspond to the outputs characterized by an increasing number of simultaneously "fired" independent pixels. The waveforms labeled 1 p.e. are for the outputs where only one pixel has fired in response to light. Note that if two or more photons were to be simultaneously absorbed by this same pixel, the output waveform would have been the same. Similarly, the waveforms labeled 2 p.e. are for two pixels firing simultaneously and so on. To obtain these cumulative waveforms, the oscilloscope is set to the persistence mode; thus, the color in the figure (from red to violet) corresponds to the frequency with which the events have occurred (from the most common to the rarest). There is a clear demarcation between waveforms labeled 1 p.e., 2 p.e., 3 p.e., etc. The 4 and 5 p.e. waveforms are linked to events that occur more frequently (red color), whereas the other events gradually become less frequent. Note that there are a few 1 and 2 p.e. waveforms that are lagging in time to the main events. They can be generated in three ways: dark noise, afterpulsing, and cross-talk.
Dark noise pulses occur randomly and are due to thermally-generated charge carriers reaching the avalanche region. If a pixel is in the "ready" state, the ensuing "dark" pulse is indistinguishable from one due to photon absorption. Such a pulse

would be labeled 1 p.e. in figure 1.52. If, however, the pixel is recovering from a primary avalanche, the "dark" pulse lags in time to the primary pulse but is not correlated with it.
The pulses due to afterpulsing and cross-talk are correlated to the primary avalanche, which can be due to photon absorption or dark noise. Afterpulsing occurs when lattice defects trap charge during an avalanche and then release the charge while the pixel recovers. The release triggers a correlated secondary avalanche whose gain M depends on V_{OV} at the time of release. Cross-talk occurs whe, during a primary avalanche in a pixel, electron-hole recombinations produce UV photons. If the same pixel reabsorbs the photon, the resulting secondary pulse would look like an afterpulse. However, if a nearby pixel absorbs the photon, the secondary correlated avalanche may be close enough in time to the primary that the resulting waveform would be labeled 2 p.e. in figure 1.52. The next section discusses in greater detail dark noise, afterpulsing, and cross-talk.
Beyond the single photon resolution, other advantages of G-APDs are summarized below:

- Work at low bias voltage ($\sim 50 \div 70$ V);
- Have low power cosumption $\left(< 50\frac{\mu W}{mm^2}\right)$;
- Are insensitive to magnetic fields up to 15 T;
- Are compact and rugged;
- Have a small sensitivity to charged particles traversing the device because of the very thin thickness of the silicon wafer (small nuclear counter effect);
- Tolerate accidental illumination;
- Have long lifetime.

So, because of its high internal gain and the additional features summarized above, SiPMs are the preferred alternatives to PMTs. Despite their many advantages they have also some drawbacks:

- The dark noise, that cannot be discriminated from the signal;
- Gain depends on temperature, since the breakdown voltage changes as a function of temperature;
- The size[21], that is limited by the dark noise. The thermal noise increases as the area increases, a good compromise between size and dark noise should be taken to obtain a device with reasonably good detection characteristics.

[21]SiPMs sizes can range between 1 mm^2 up to 16 mm^2

For all these reasons SiPM technology has recently achieved a very high level of performances but its application to astroparticle physics experiment is definitely compromised by its small sensitive surface available presently (typically not exceeding 10 mm^2).
In this context, an interesting solution is represented by the VSiPMT (acronym of Vacuum Silicon PhotoMultiplier Tube), a novel photodetector based on the combination of PMT and SiPM technologies.

1.9 Hybrid Photodetectors: HPDs

The hybrid photodetector's structure is similar yet different from a conventional PMT. Like PMTs, the HPD is a vacuum tube with a photocathode that detects light, an electron multiplier that multiplies electrons, and an output terminal that outputs an electrical signal. But unlike PMTs, which use multiple dynodes as electron multipliers, the HPD uses a solid state diode as electron detector with a multiplication stage obtained by electron bombarding instead. So the HPDs combine the sensitivity of photomultipliers with the spatial and energy resolution of silicon detectors, which leads to a very good photon counting capability. These devices, although developed more than 40 years ago (since the 70'), have received attention by the high energy physics community only in the more recent past.
At first, the solid state device used as electron multiplier was a p-i-n diode. The Dutch company DEP (Delft Electronic Products) worked in this direction providing a series of single and multipixel HPD's both electrostatically and proximity focused (fig. 1.53).

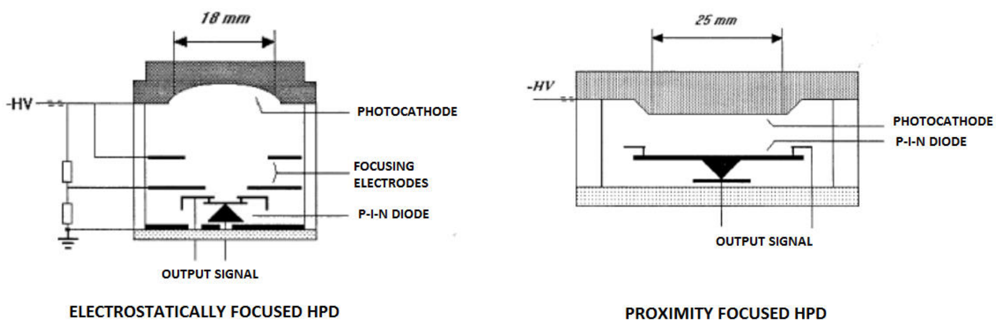

Figure 1.53: Schematic view of hybrid detectors using a p-i-n diode as electron multiplier electrostatically and proximity focused

Electrostatically focused design is chosen when high resolution imaging is required because the electrostatic lens effect largely compensates for the spread of the photoelectron velocity and emission angle at the photocathode. Small pin cushion

shape distortions at large distance from the optical axis are typical for this design. Proximity focused design leads to compact and, because of the small gap between photocathode and silicon sensor, highly B-field tolerant detectors. Because there is no demagnification, the photosensitive area of the detector is limited to the size of the silicon sensor.
These devices were not very successful, mainly because of their poor internal amplification. Indeed, as can be seen from figure 1.54, to obtain a 3.5 x 10^3 gain, 15kV power supply voltage is required.

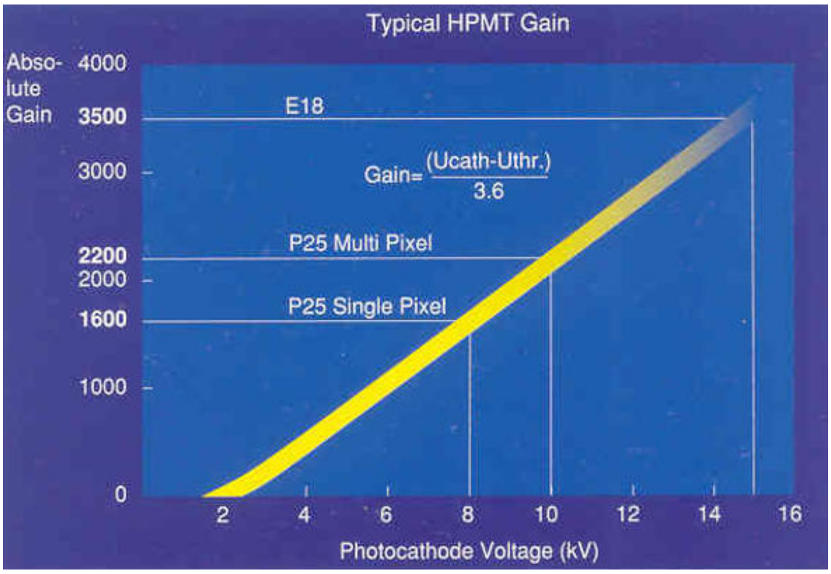

Figure 1.54: Typical HPD gain

Hamamatsu photonics provided an upgrade fabricating a proximity focused HPD equipped with an avalanche diode APD instead of a p-i-n diode (fig.1.55).
APDs are high-speed and high sensitivity silicon devices which consist of reverse biased p-n junctions, so the electron multiplication is generated by the avalanche process triggered by the arrival of photons on the device's surface, which generates electron-hole pairs that, drifting across the depletion region of the silicon bulk, create additional pairs. APDs have a low gain factor ($\sim$ 100) so in this device the electron multiplication is carried out in two steps (fig. 1.55):

- an electron-bombardment stage, where photoelectrons are accelerated towards the APD by a large voltage difference ($\sim$ 8 kV) and simultaneusly acquire high kinetic energy (gain = 3 x 10^3);
- an APD stage (gain = 50 x 100) where, because of the kinetic energy gained in the previous stage, each photoelectron produces many electron-hole pairs triggering a big avalanche that results in a total gain of about 10^5.

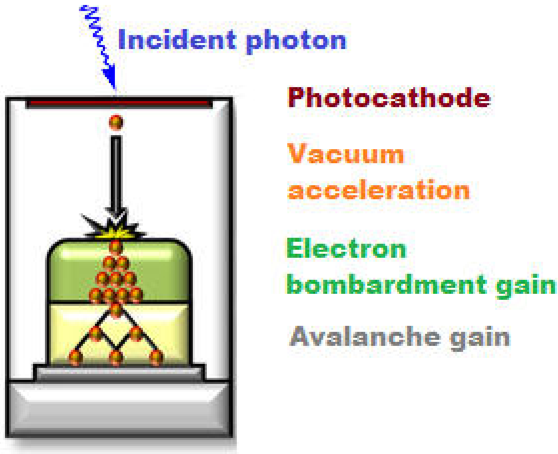

Figure 1.55: Schematic view of a hybrid detector using an avalanche diode as electron multiplier

The employment of the APD in substitution of the dynode chain leads to a huge improvement of the signal quality. Indeed the HPD advantages compared to the PMT are the following:

- it produces better pulse height resolution than PMTs due to the HPD's very high first gain stage. The first gain stage determines the signal-to-noise ratio of the electron multiplication, which determines the detector's ability to differentiate between one and multiple photons. This makes the photon counting possible;
- it is inexpensive in terms of power consumption;
- since only photoelectrons move in vacuum in HPDs, there is less chance to produce a feedback of ions, this results in a reduction of afterpulsing.

However it has several drawbacks:

- it has a low resolution photon counting capability because of the statistical fluctuations generated in the multiplication process, due to the fact that this is a proportional device;
- gain does not exceed $\sim 10^5$;
- because of the low gain of the APD an additional gain is required. It is obtained with an electron bombardement of the APD. To accelerate the

electrons towards the APD a very high voltage has to be supplied to the photocathode; this makes the gain instable since it depends on the stability of the HV;

- isolation is complicated due to its particular manufacturing.

The amplification factor of this detector is $\sim 10^5$, therefore it is much lower than that of the PMT ($\sim 10^7$). In many applications where high sensitivity is required at low light levels, this gain is insufficient, and that's the reason why PMT's are still the preferred device for low light detection.
So the innovative idea is to develop a new type of vacuum photomultiplier in which the photoelectron multiplication is performed using APDs operating in a high-gain regime in which a reverse bias voltage, above the breakdown voltage, is applied to the diodes, i.e. the Geiger mode. In this mode of operation the multiplication factor of the G-APDs reaches values $\sim 10^6$, and no more electron-bombardment is needed. This results in a superior gain stability since it depends only on the multiplication device (supplied at 70V) and not on the photocathode (supplied at 8kV); moreover, no fluctuations in photon counting occur since G-APDs give a boolean type answer (the photon is passed or not) and not a proportional answer.

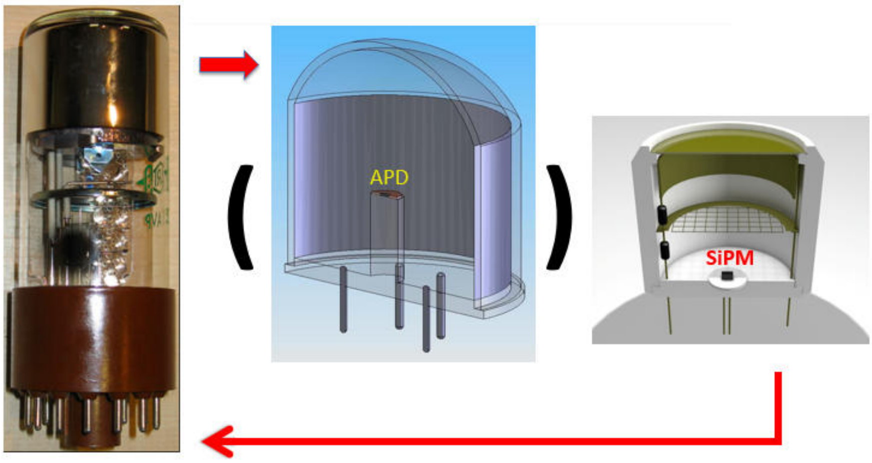

Figure 1.56: Evolution of vacuum tube detectors

This idea is, therefore, proposed to return to the concept of the PMT gain (there is not an intermediate amplification stage between the photocathode and the multiplication element) by exploiting the G-APD technology with its superior performances in single photon detection, no fluctuations in the multiplication phase, high gain with no high power supply required (fig. 1.56).

Chapter 2

The Idea Behind VSiPMT

To overcome all the problems listed before, Professor Giancarlo Barbarino from the University of Naples Federico II proposed the VSiPMT (Vacuum Silicon Photo-Multiplier Tube fig. 2.1): an innovative design for a revolutionary photon detector for Astroparticle Physics applications.
The VSiPMT has many attractive features. In particular, a low power consumption and an excellent photon counting capability [20].

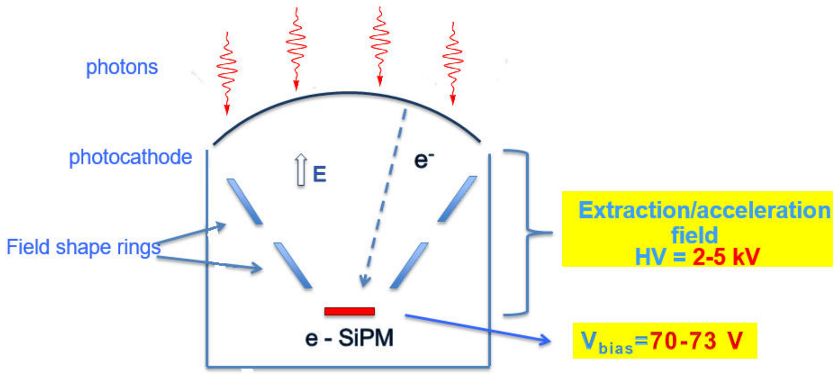

Figure 2.1: Schematic view of the VSiPMT

For these reasons, this project, aimed at creating new scientific instrumentation for future missions of Exploration and Observation of the Universe, was funded by the Italian Space Agency (ASI) and by the Italian National Institute for Nuclear Physics (INFN). After the feasibility test of the idea, in which the performance of a special non-windowed SiPM realized by the company Hamamatsu (SiPM) have been tested as electron detector and current amplifier, Hamamatsu realized also two VSiPMT industrial prototypes, that have been fully characterized. The encouraging results of this analysis convinced Hamamtsu Photonics to assemble a new 25 mm diameter VSiPMT. This prototype has been fully characterized too and the results of this characterization are collected in this thesis.

2.1 VSiPMT Description

In the previous chapter a comparison between three classes of photodetectors have been done. From this analysis emerges that different multiplication processes can entail substancial differences in the detection features.
Indeed, even if PMTs boast almost one century of history, they show many defects. The solid state photodetectors, APDs and SiPMs, represent a technological progress that goes beyond PMTs' limits. In particular, SiPM technology has achieved a very high level of performances that can meet the requirements of many experiments.
Despite all, SiPMs have a size limited by the thermal noise, so their application to astroparticle physics experiment is partially compromised. A big challenge is, therefore, to find a way to use SiPMs to detect photons from large surfaces and/or volumes, as typically needed in many astroparticle physics experiments.
An interesting option in this direction is represented by making a photon conversion by a photocathode which focuses photoelectrons on the small SiPM area.
The VSiPMT (Vacuum Silicon PhotoMultiplier Tube), an innovative design for a modern photodetector, is based exactly on the idea of combining of a SiPM with an hemispherical PMT standard envelope (fig. 2.2) [23].

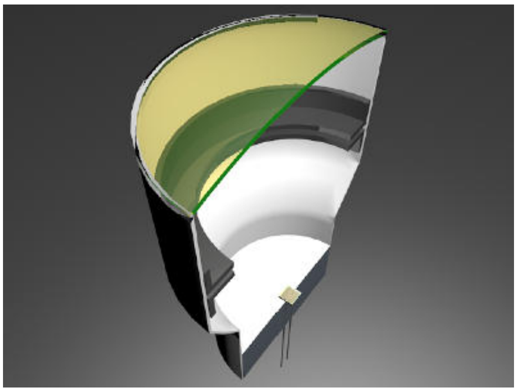

Figure 2.2: A cutaway of the VSiPMT showing the interior composition of the device. On the top there is the light entrance window, then a photocathode for the photons conversion into electrons. In the middle there is a focusing ring producing an electric field which accelerates and focuses the photoelectrons on the SiPM surface. Finally, on the bottom there is the SiPM acting in this configuration as an electron detector and current amplifier. Everything is assembled into and hermetically sealed container

The idea was born in Naples in 2007 with the goal to enlarge indirectly the SiPM sensitive surface, thus exploiting its good detection features also in large astroparticle physics experiments [24]. In this device the multiplication stage is provided by the SiPM that acts as electron detector and so as current amplifier.

2.2 Photocathodes

The VSiPMT design includes a photocathode to convert photons into electrons that will be than detected and thus multiplied by the SiPM.
Photocathodes are mostly made of compound semiconductors, consisting of alkali metals with a low work function[1], and can be operated both in reflection (opaque) and in transmission mode (semitransparent) [25]. In the former case, when the light enters and impinges on the photocathode a photoelectron is extracted in the same side of the incoming light and is driven on the multiplying sensor (fig. 2.3 right), while in the latter case when the light impinges on the photocathode a photoelectron is extracted on the opposite side with respect to the incoming light (fig. 2.3 left).

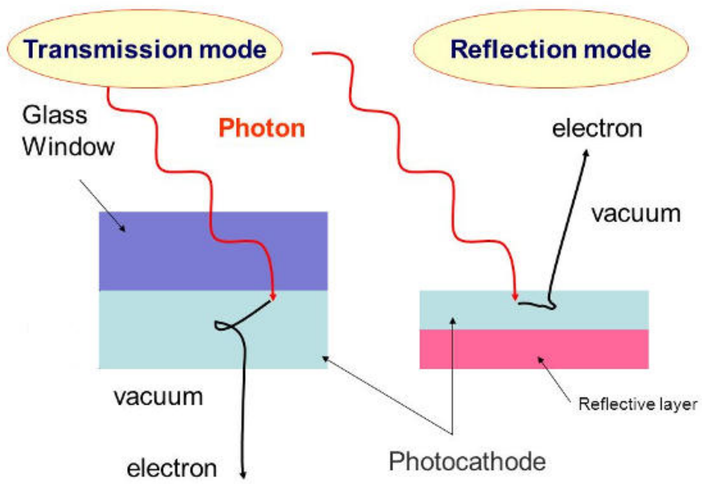

Figure 2.3: Reflective and transmission mode photocathodes operating principle

In both configurations, different materials can be used. The materials can be chosen depending on the spectral region of sensitivity and on the achievable quantum efficiency.

[1]In solid-state physics, the work function is the minimum thermodynamic work (i.e. energy) needed to remove an electron from a solid to a point in the vacuum immediately outside the solid surface.

The spectral response of several materials is showed in figure 2.4. Photocathodes operation can be described using the energy band theory expressed in terms of the energy gap (E_G), electron affinity (E_A), Fermi level (E_F), work function (ϕ), and so on.

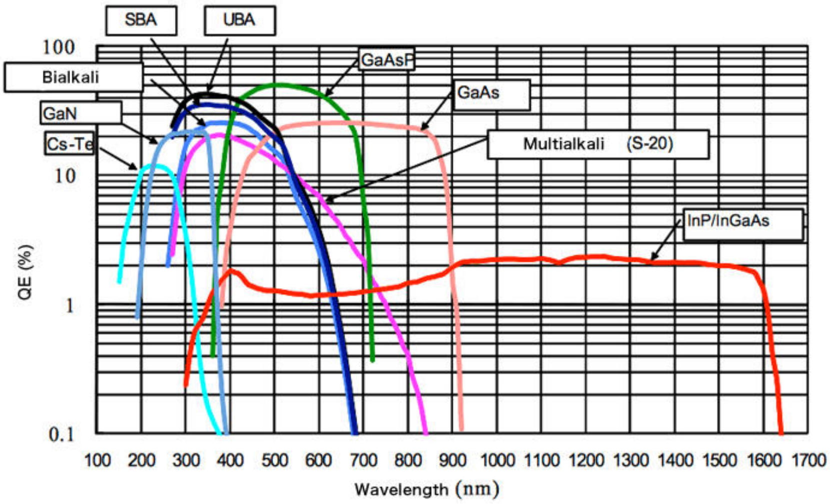

Figure 2.4: Spectral response of photoelectron emissive materials

When a photon strikes a photocathode, electrons in the valence band absorb photon energy (E_γ) and become excited to the conduction band, diffusing toward the photocathode surface.
If the energy of these electrons overcomes the vacuum barrier, then they are emitted into the vacuum. This electron emission process was expressed as follows by W. E. Spicer [26] by means of his three step model, which explains the photoelectron emission process using three steps: optical absorption process, electron diffusion process, and escape process [27]:

$$\eta = (1 - R) \cdot \frac{\alpha_{PE}}{\alpha} \cdot \frac{1}{1 + \frac{1}{\alpha L}} \cdot P_S \tag{2.1}$$

Where η is the conversion efficiency of the photocathode material (i.e. quantum efficiency, function of the photon frequency), R is the reflection coefficient, α is the full optical absorption coefficient for photons, α_{PE} is the absorption coefficient when electrons are excited to a level greater than the vacuum level, L is the diffusion lenght of electrons, P_S is the escape probability of electrons.
It is clear, from this expression that it is possible to enhance the quantum efficiency by extending the diffusion length L to improve the crystalline properties of the photocathodes and also reduce the electron affinity by increasing the P_S (NEA-photocathodes).

It has been studied that a crystalline photocathode when activated by depositing a few monolayers of cesium and a strong oxidizer (such as fluorine or oxygen) gain the NEA (Negative Electron Affinity) property. This means that the Cs-O activation causes the energy band in the surface to curve downward so that the electron affinity has a negative value, thus allowing electrons at the bottom of the conduction band to escape (fig. 2.5).

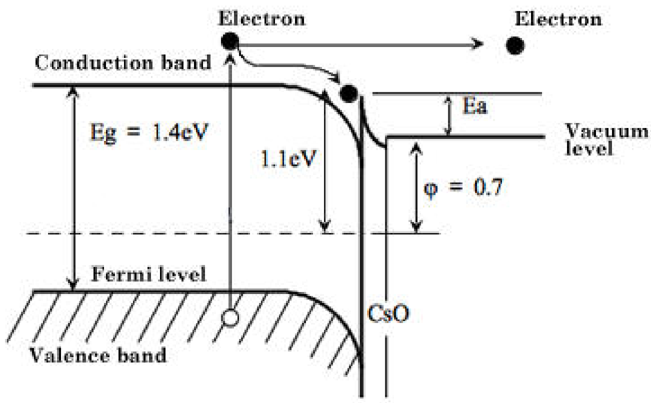

Figure 2.5: NEA photocathode band model

The most used photocathode materials are:

- **CsI**: cesium iodide is not sensitive to solar radiation and therefore often called "solar blind". Its sensitivity sharply falls off at wavelengths longer than 200 nanometers and it is exclusively used for vacuum ultraviolet detection.

- **Bialkali (Sb-Rb-Cs, Sb-K-Cs)**: Since two kinds of alkali metals are employed, these photocathodes are called "bialkali". The transmission type of these photocathodes has a spectral response ranging between ultraviolet and visible region. On the other hand, the reflection-type bialkali photocathodes are fabricated by using the same materials, but different processing. As a result, they offer enhanced sensitivity on the long wavelength side, achieving a spectral response from the ultraviolet region to around 700 nanometers.

- **Multialkali (Sb-Na-K-Cs)**: This photocathode uses three or more kinds of alkali metals. Due to high sensitivity over a wide spectral response range from the ultraviolet through near infrared region around 850 nm.

- **Ag-O-Cs**: Transmission type photocathodes using this material are sensitive from the visible through near infrared region, from 400 to 1200 nm, while the reflection type exhibits a slightly narrower spectral response region from 300 to 1100 nm. Ag-O-Cs photocathodes are chiefly used for near infrared detection.

2.3 Entrance Window

Each entrance window material transmit the incoming light in a different way depending on the wavelength. In particular, these materials tend to absorb ultraviolet light and, as a consequence, the choise of the window material determins the short wavelenght sensitivity limit of the whole device [28].
The most used window materials are:

- **MgF_2**: A magnesium fluoride crystal is used as a practical window material because it allows transmission of vacuum ultraviolet radiation down to 115 nm.
- **Synthetic silica**: It transmits ultraviolet radiation down to 160 nm.
- **Borosilicate glass**: This is the most commonly used window material. The borosilicate glass does not transmit ultraviolet radiation shorter than 300 nanometers. It is not suited for ultraviolet detection shorter than this wavelength.

A plot of the window material transmittance with respect to wavelenghts is in figure 2.6 together with table which summarizes a final overview about how the entrance windows usually matches the photocathodes (fig. 2.7).

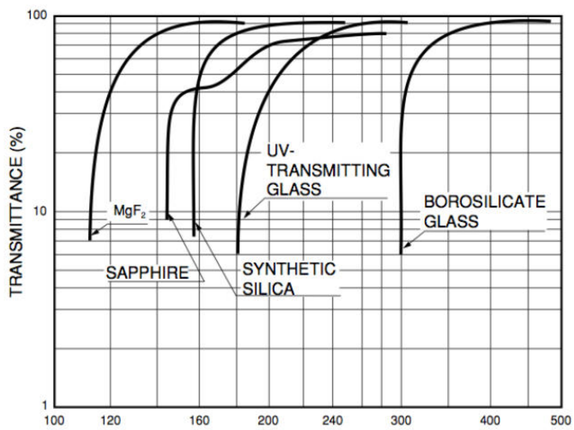

Figure 2.6: A plot of the transmittance of several window materials with respect to wavelenght

WAVELENGTH (nm)

Photocathode	Window	Spectral Range (nm)	QE (%)	λ (nm)
CsI	MgF_2	115-200	13	130
CsTe	Quartz	160-320	14	210
CsTe	MgF_2	115-320	14	200
Bialkali	Borosilicate	300-650	27	390
Bialkali	UV	185-650	27	390
Bialkali	Quartz	160-650	27	390
Multialkali	Borosilicate	300-850	20	375
Miltialkali	UV	185-850	25	280
Multialkali	Quartz	160-850	25	280
Ag-O-Cs	Borosilicate	400-1200	0.36	740

Figure 2.7: Reference for spectral response of transmission mode photocathodes

2.4 The SiPM as Electron Multiplier

As said above, the VSiPMT is a new configuration for an hybrid photodetector in which the dynode chain is replaced by a SiPM, which acts as **electron** detector and multiplier [29].
For this purpose a SiPM has to become a **SiEM** (Silicon Electron Multiplier).
Since photoelectrons produced by the photocathode need a certain energy to enter into the Silicon bulk starting the Geiger avalanche and so to give a signal, high voltage between photocathode and SiPM is required. A special windowless SiPM is necessary to minimize the threshold energy required. When an electron enters into the Silicon bulk it generates electron-hole pairs by ionization. In this case the Electron Detection Effciency, namely EDE, can be evaluated as follows:

$$EDE = FF \cdot (1 - \eta) \cdot (P_e + P_h - P_e \cdot P_h), \tag{2.2}$$

which says that the probability that an impinging electron is detected depends on three factors: FF, the fill factor of the SiPM; η the backscattering coefficient; P_e and P_h are respectively the probability that the geiger avalanche is generated by an electron or a hole.
Since the SiPM is a matrix of cells the separation between the cells is a dead area, the percentage of active area of the device is, thus, given by the fill factor, FF, that represents therefore the geometric factor. When an electron impinges the SiPM surface, the entrance probability scales with the geometric factor FF.
An electron hitting the SiPM surface has a probability η to be backscattered. Hence, the probability that an electron enters in the Silicon bulk is $(1 - \eta)$.
Finally, once the electron is entered, it produces an ionization track that generates electron-hole pairs. In such a device both electrons and holes can start the geiger

avalanche. The probability that the geiger avalanche is triggered by an electron, P_e, is double with respect to the probability that the geiger avalanche is triggered by an hole, P_h. As a consequence in order to maximize the EDE, the SiPM needs a p over n structure. A more clear outline of the situation can be done by looking at figure 2.8.

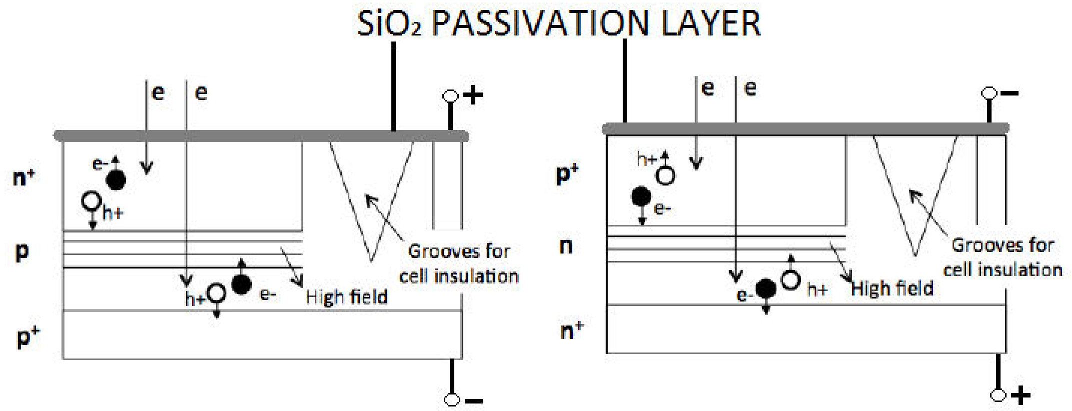

Figure 2.8: n-over-p internal structure of the SiPM (left). p-over-n structure of the SiPM (right)

On the left a scheme of the processes occuring in a n-over-p configuration are presented, while on the right picture there are those occurring in a p-over-n configuration of the SiPM.
The main difference between the two internal structures of the SiPM is that in the former case the incoming electron needs to cross the high field region in order to let the electron start the geiger avalanche, while in the latter case is not necessary. Actually, in a p-over-n SiPM the photoelectron ionization range lies in the p^+ region allowing electrons to cross the whole high-field zone p^+n, going to 0 voltage, and triggering the Geiger avalanche with high efficiency. This configuration is particularly suited for the VSiPMT application because allows to detect also electrons with a shorter range and so with a lower energy.
This simplifies far and away the operation of the VSiPMT making possible to achieve a relatively low operating voltage of the photocathode and focus ring ($\sim$ 3kV).
The reduction of the thickness of the entrance layer of the junction p^+nn^+, is an absolutely necessary condition to allow incident photoelectrons to create sufficient electron-hole pairs to induce the micro-pixel Geiger discharge at a fixed HV, and maximize the PDE.
Using a Silicon photomultiplier allows to reach a very high gain totally provided by the pixels working in geiger mode. This has many advantages:

- **Excellent photon counting**. The photocathode is only a passive intermediary. The photons are converted into electrons that are accelerated towards the SiPM surface. The electron entering into the Silicon bulk gives a standard output signal. So as for photons, the device shows an exellent resolution of the single electron allowing an easy photon counting.

- **High gain with low voltage**. Differently from a classical HPD, in this case the high gain is totally realized by the SiPM pixels operating in geiger mode. The electron crossing the geiger region gives an output standard signal with the typical gain of the SiPM $\sim 10^6$. This means that there is no need for an additional gain step provided by high energy photoelectrons. In such a device, indeed, the photoelectrons only need to enter into the Silicon bulk to produce a signal. Therefore it exists a threshold energy for the photoelectrons that is necessary to drive them in the geiger region of the device and is given by the voltage difference between the photocathode and the SiPM. The average voltage supplied to the photocathode in a VSiPMT is commonly $\sim$ 3 kV .

- **Negligible power consumption**. The absence of the dynode chain entails that also the voltage divider used to supply voltage to the dynodes is unnecessary. Removing the voltage divider means that in VSiPMT the power consumption is linked only to the photocathode and the SiPM. So thanks to this new configuration a substancial reduction in power consumption is achieved, thus resulting now $\leq$ mW. This is a great deal for such experiments operating in hostile environments (i.e. underwater, in ice or in space).

- **No gain dependence on the noise**. Since the SiPM operates in geiger mode, the gain is not anymore limited by the thermal noise, which is totally independent.

- **High speed**. The absence of a dynode chain means that the transit time is lower because it involves only the path from the photocathode to the SiPM. Moreover being the voltage difference between photocathode and SiPM much higher with respect to the one in a PMT ($\sim$ kV vs $\sim$ 100V) means that in VSiPMT the photoelectrons have a higher energy and so are faster than in PMTs. As for transit time, the spread in transit time (TTS) is due to the electron trajectories between the photocathode and the SiPM and so a certain reduction of the VSiPMT TTS with respect to a classical PMT TTS is expected.

- **Compactness and simplicity**. Using a SiPM allows to obtain a device very compact and mechanically simple, having a lower number of connection with respect to a PMT.

The various theoretical studies and feasibility tests that led to the design and implementation of this innovative device are not a subject of this thesis. We have characterized the latest industrial prototype manufactured by Hamamatsu.
The results of this work are given in the second part of this thesis.

Part II

Measurements and Data Analysis

Chapter 3

Characterization of SiPMs

Since 2006, Hamamatsu Photonics, a Japanese manufacturer of optical sensors (including photomultiplier tubes), electric light sources, and other optical devices and their applied instruments for scientific, technical and medical use [17], has begun production of a series of SiPMs called Multi-Pixel Photon Counters. The Multi-Pixel Photon Counter is becoming a popular choice of a photodetector in application where even single photons must be detected. Understanding how this detector operates and how its optical and electrical characteristics change with respect to the parameters of an experiment is critical for the proper interpretation of scientific data. In this chapter we are going to present the results of measurement performed on the latest generations of MPPCs produced by Hamamatsu Photonics in order to determine their basic optical and electrical characteristics.

3.1 Specifications of the Characterized SiPMs

In this section we will review the features of the devices characterized at our home lab. They all are manufactured by Hamamatsu and belong to different technologic generations.

3.1.1 The Latest Generation Series: S13360

The S13360 series are SiPMs for precision measurements (such as DNA sequencer, laser microscope and fluorescence measurements) because of their lower afterpulse, crosstalk and dark counts with respect to previous products as we will see later. They have an effective area of 3 x 3 mm^2, our sample had a ceramic package and was a special windowless device manufactured especially for Prof. Barbarino's group.
Tables below (fig. 3.1) summarize the specifications and the operating parameters

of this SiPM at 25°C.

Type no.	Pixel pitch (μm)	Effective photosensitive area (mm)	Number of pixels	Package	Fill factor (%)
S13360-1325CS	25	1.3 × 1.3	2668	Ceramic	47
S13360-1325PE				Surface mount type	
S13360-3025CS		3.0 × 3.0	14400	Ceramic	
S13360-3025PE				Surface mount type	
S13360-6025CS		6.0 × 6.0	57600	Ceramic	
S13360-6025PE				Surface mount type	
S13360-1350CS	50	1.3 × 1.3	667	Ceramic	74
S13360-1350PE				Surface mount type	
S13360-3050CS		3.0 × 3.0	3600	Ceramic	
S13360-3050PE				Surface mount type	
S13360-6050CS		6.0 × 6.0	14400	Ceramic	
S13360-6050PE				Surface mount type	
S13360-1375CS	75	1.3 × 1.3	285	Ceramic	82
S13360-1375PE				Surface mount type	
S13360-3075CS		3.0 × 3.0	1600	Ceramic	
S13360-3075PE				Surface mount type	
S13360-6075CS		6.0 × 6.0	6400	Ceramic	
S13360-6075PE				Surface mount type	

Type no.	Measurement conditions	Spectral response range λ (nm)	Peak sensitivity wavelength λp (nm)	Photon detection efficiency PDE*4 λ=λp (%)	Dark count*5 Typ. (kcps)	Dark count*5 Max. (kcps)	Terminal capacitance Ct (pF)	Gain M	Breakdown voltage VBR (V)	Crosstalk probability (%)	Recommended operating voltage Vop (V)	Temperature coefficient at recommended operating voltage ΔTVop (mV/°C)
S13360-1325CS	Vover =5 V	270 to 900	450	25	70	210	60	7.0×10^5	53 ± 5	1	VBR + 5	54
S13360-1325PE		320 to 900										
S13360-3025CS		270 to 900			400	1200	320					
S13360-3025PE		320 to 900										
S13360-6025CS		270 to 900			1600	5000	1280					
S13360-6025PE		320 to 900										
S13360-1350CS	Vover =3 V	270 to 900		40	90	270	60	1.7×10^6		3	VBR + 3	
S13360-1350PE		320 to 900										
S13360-3050CS		270 to 900			500	1500	320					
S13360-3050PE		320 to 900										
S13360-6050CS		270 to 900			2000	6000	1280					
S13360-6050PE		320 to 900										
S13360-1375CS	Vover =3 V	270 to 900		50	90	270	60	4.0×10^6		7	VBR + 3	
S13360-1375PE		320 to 900										
S13360-3075CS		270 to 900			500	1500	320					
S13360-3075PE		320 to 900										
S13360-6075CS		270 to 900			2000	6000	1280					
S13360-6075PE		320 to 900										

Figure 3.1: Summary of S13360 SiPM specifications (our sample is evidenced in purple)

In figure 3.4 is shown the dimensional outline of the photodetector (unit: mm). Metal electrodes, made in oxygen-free copper, provide a connection between internal electrodes (anode and cathode) and the external side of the ceramic package.

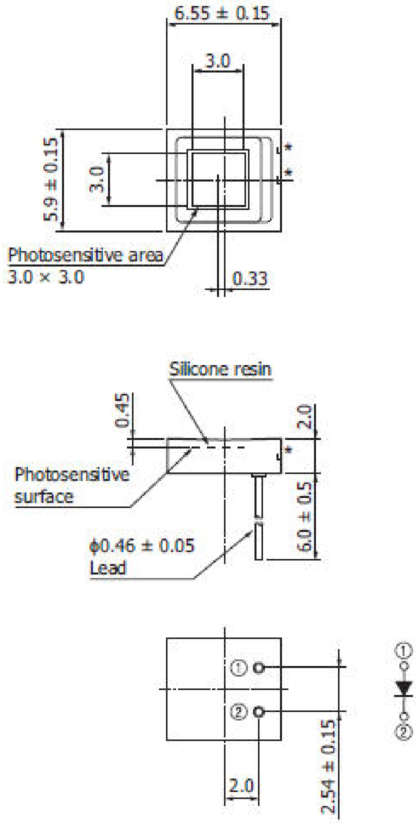

Figure 3.2: S13360 dimensional outline

3.1.2 The Relatively New Series: S10943

This is the special windowless version of another series (S10362) manufactured especially for Prof. Barbarino's group so there is not a commercial datasheet which summarizes its characteristics. The absence of the protective entrance window eases the entrance of the photoelectrons into the silicon bulk, indeed these devices where mounted on the very first home made VSiPMT prototype.
These SiPMs have an effective area of 3 x 3 mm^2 with 50 μm pixel pitch, our sample had a ceramic package, gain equal to M = 1.25 x 10^6 and dark counts rate DR = 1091 kcps at 25°C.

3.1.3 The Old Generation Series: S10931-100P

These MPPCs are the older generation devices, indeed their performance is worse than the other two series [33]. They have an effective area of 3 x 3 mm^2, our sample had a SMD package.
The table below (fig. 3.3) summarizes the specifications and the operating parameters of this SiPM at 25°C

Parameter	Symbol	S10362-33 series			S10931 series			Unit
		-025C	-050C	-100C	-025P	-050P	-100P	
Effective active area	-	3 × 3			3 × 3			mm
Number of pixels	-	14400	3600	900	14400	3600	900	-
Pixel size	-	25 × 25	50 × 50	100 × 100	25 × 25	50 × 50	100 × 100	μm
Fill factor *1	-	30.8	61.5	78.5	30.8	61.5	78.5	%
Spectral response range	λ	320 to 900			320 to 900			nm
Peak sensitivity wavelength	λp	440			440			nm
Operating voltage range	-	70 ± 10 *2			70 ± 10 *2			V
Dark count *3	-	4	6	8	4	6	8	Mcps
Dark count Max. *3	-	8	10	12	8	10	12	Mcps
Terminal capacitance	Ct	320			320			pF
Time resolution (FWHM) *4	-	500 to 600			500 to 600			ps
Temperature coefficient of reverse voltage	-	56			56			mV/°C
Gain	M	2.75×10^5	7.5×10^5	2.4×10^6	2.75×10^5	7.5×10^5	2.4×10^6	-

Figure 3.3: Summary of S10931-100P SiPM specifications (evidenced in purple)

In figure 3.4 is shown the dimensional outline of the photodetector (unit: mm).

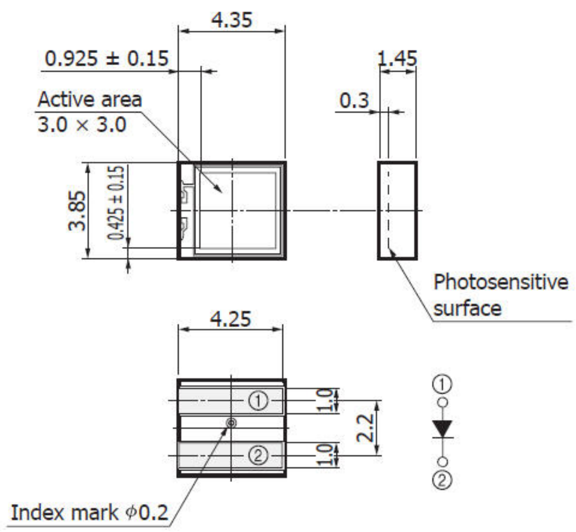

Figure 3.4: S10931-100P dimensional outline

3.2 Experimental Set Up and Measuring Procedure

Every measurement descripted in this chapter was performed between 20° and 22°C temperature, by means of the following experimental set-up:

- Dark box;
- Digital power meter Newport mod. 815, 1nW sensitivity;
- Hamamatsu Photonics picosecond light pulser (pulse duration = 47 ps) mod. M10306-04, with monochromatic emission in the visible blu/violet light (407 nm wavelenght);
- Electronic board made ad hoc for the SiPM's signal amplification on which the SiPM and a current voltage amplifier are mounted;
- DC voltage generator Agilent 0.1V sensitivity mod. E3612A used as a power supply for the SiPM;
- DC voltage generator Matrix mod. MPS-3005-L-3 used as a dual power supply for the signal amplifier mounted on the electronic board;
- A Newport optical beam splitter mod. 234607 with 2 outputs:
  - A, which outputs 1% of the input optical power;
  - B, which outputs 99% of the input optical power;
- A 1 meter ThorLabs 600 μm core multimode optical fiber mod. FT600UMT-0.39NA;
- Variable height support for the fiber optic;
- 3mm Edmundoptics opal diffusing glass;
- Digital Teledine LeCroy serial data analyzer mod. SDA 760Zi-A, 4 input channels, 6 GHz bandwidth with 40 GS/s sample rate.

For every measurement we will show the arrangement of this set-up, but the electronic board for SiPM's signal amplification deserves a separate discussion.
SiPMs are current sources with an high nominal internal gain ($\sim 10^6$). Neverthless, depending on the experiment requirements a voltage readout could be preferred with respect to a current readout. In this situation, a conversion of the SiPM output current to a proportional voltage is required. With this aim, a design for

a custom amplifier has been studied in order to find the best configuration. It is based on the current-to-voltage conversion made by an operational amplifier and forsees a current and a voltage feedback op-amp. The general design of this circuit is shown in figure 3.5.

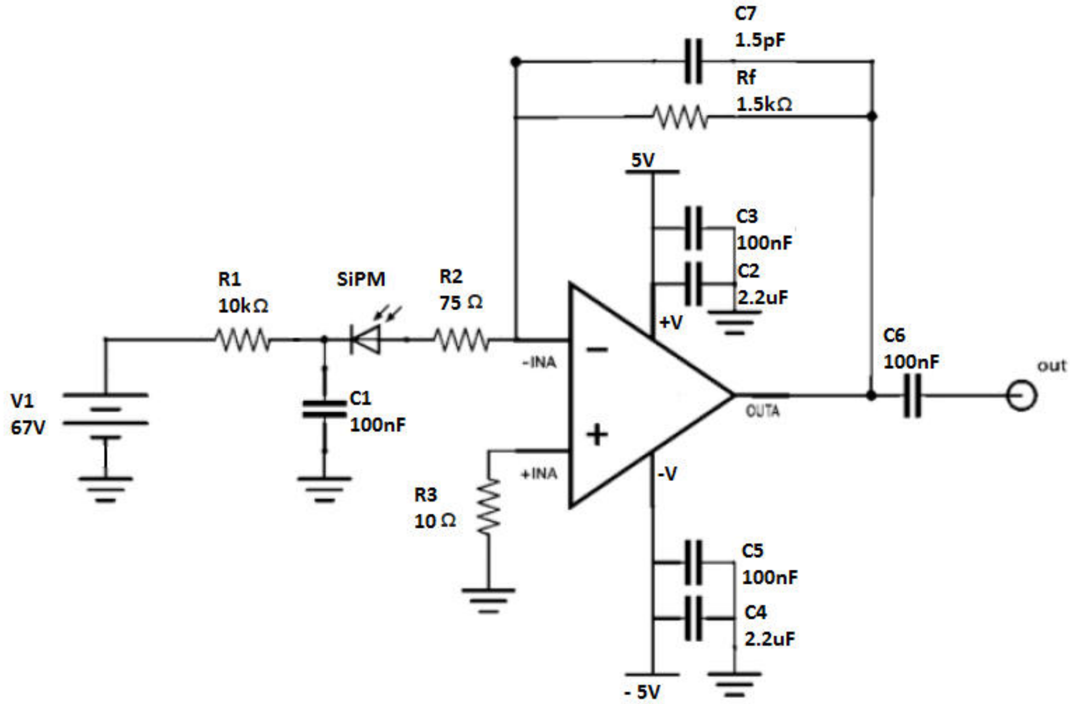

Figure 3.5: General scheme of the amplification circuit

A low noise circuit is necessary to properly analize the device features during the characterization phase that will follow. Since op-amps with high bandwidth integrate a large amount of noise, several op-amps have been considered with different bandwidth and slew rate. The amplified output SiPM signal shape of all the configurations has been compared and have been observed the electronic noise, the rise time and fall time. From this study emerges that the Texas Instruments LMH6624 op-amp is the best solution in terms of noise, timing and gain. It has 81dB open loop gain, 95dB common mode rejection ratio, 1.5 GHz gain bandwidth and operates from $\pm$ 2.5V to $\pm$ 6V in dual mode supply. With this amplification circuit, SiPM's signal's first peak had an amplitude of $\sim 10mV$.

3.2.1 Gain Measurement

The gain (M) is defined as the number of carriers contained in the single-cell current pulse, since this is the number of carriers generated during the avalanche in response to an absorbed photon. From the discussion about the equivalent circuit model for a GM-APD (fig. 1.48), the gain is given by the discharge of the capacitor Cd from $V_{bias} = (V_{BD} + V_{OV})$ to V_{BD} and therefore is given by the charge stored on Cd with a potential difference V_{OV}:

$$G(V_{OV}) = \frac{C_d \cdot V_{OV}}{e} \tag{3.1}$$

where e is the singol electron elementary charge. Assuming Cd constant for $V_{bias} > V_{BD}$, gain increases linearly with the overvoltage.
By means of the experimental set-up described at the beginning of this chapter and arranged as in figure 3.6, we performed a gain measurement on the latest generation SiPM S13360-4929 produced by Hamamatsu Photonics.

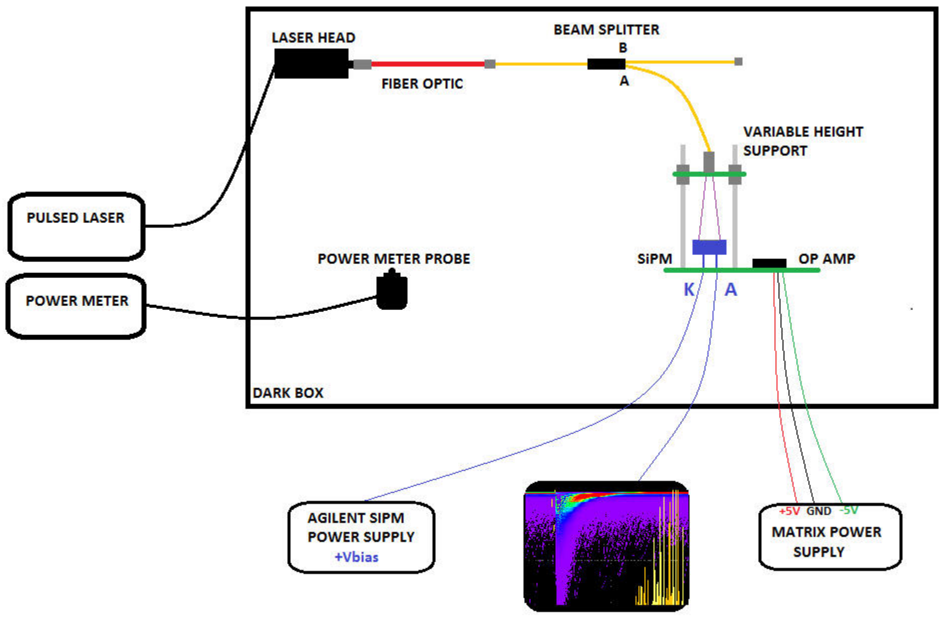

Figure 3.6: Schematic view of our experimental set-up

For this measure we placed the SiPM in very low light conditions. To implement this condition we had the need to interpose between the head of the laser and the SiPM both the ThorLabs 600 μm core fiber and the beam splitter whose output A (1% of the output power from the red fiber) was sent in input to the SiPM. With this set-up, we obtained that the optical power output corresponds to an average of 10 photons per pulse on the active surface of the detector. This system was calibrated using the power meter Newport mod. 815.
The laser at our disposal was equipped with an output which generates a signal of standard amplitude (2.5V) each time it sends a light pulse. We used this sig-

nal as trigger[1] for the oscilloscope to acquire the signals produced by the SiPM. Since SiPM's characteristics vary with the operating voltage (increasing the operating voltage improves the photon detection efficiency and time resolution, but also increases the noise), an optimum operating voltage must be selected to match the application; the device's datasheet provides a recommended operating voltage V_{OP}[2] with which we supplied it.
In these conditions, we were able to clearly distinguish the peaks 1, 2, 3 and 4 p.e. Integrating a waveform with respect to time gives the net output charge for the event. The amount of output charge is linearly proportional to the number of fired pixels, which, in turn, is proportional to the number of simultaneously absorbed photons. Therefore, this information after integrating each waveform can be expressed in the form of a histogram; figure 3.7 is an example of such a histogram built by means of our oscilloscope[3].
Assuming that all the SiPM's pixels are identical, the difference in area between a peak of the spectrum and the following provides a measure of the charge generated by the individual pixel.
By varying the value of the supply voltage V_{bias} between 54.7 and 55.8 V by 0.1V steps, we acquired, for every step, areas of the signals with 10000 measures runs. Then we measured the distances between these peaks (2 p.e. - 1 p.e.), (3 p.e. - 2 p.e.), (4 p.e. - 3 p.e.) and, for every value of V_{bias} we calculated their average with their errors.
Dividing this by the feedback resistance of the amplifier we get the time integral of the output current generated by the individual SiPM's pixel, that is its total charge. By dividing this total charge by the single electron charge we obtain the SiPM gain M as a function of the supply voltage.

$$M = \frac{1}{e}\int \frac{V_{mean}}{R_f}dt = \frac{1}{e}\int I_{1pixel}dt = \frac{Q_{tot}}{e}. \tag{3.2}$$

[1]Triggering is the means by which we can coax an oscilloscope into showing us what we're looking for in an input signal, and indeed even simply to display it in a stable fashion. Triggering type we used in this thesis is the Edge Trigger

[2]Typically $V_{OP} \sim V_{BD}$ + 5V but in this case it was $V_{OP} \sim V_{BD}$ + 3V

[3]The Teledyne LeCroy SDA 760Zi is provided with a function that allows the user to calculate automatically the area of a waveform

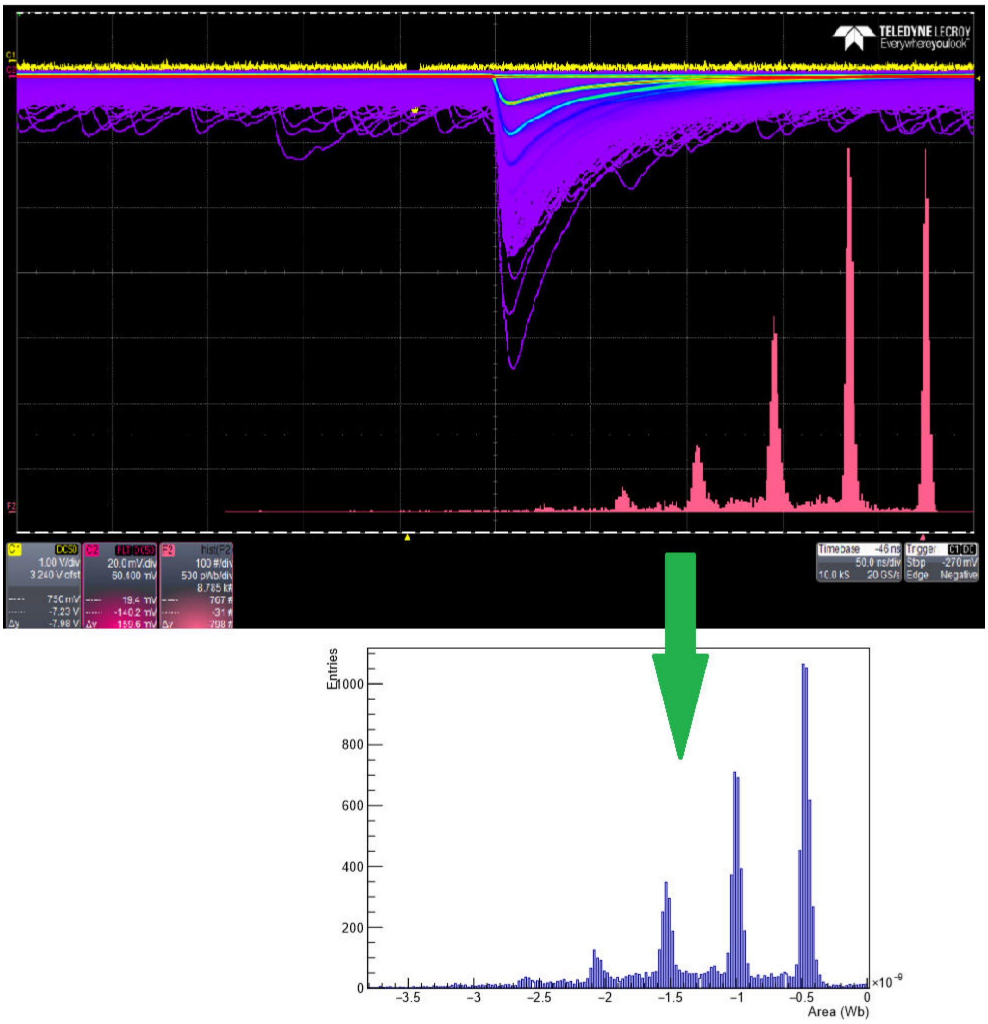

Figure 3.7: SiPM's output signal and the spectrum of areas beneath the peaks. Notice that waveforms corresponding to different numbers of fired pixels (and so the peaks in the spectrum) are extremely well separated

The results of this measurement are shown in figure 3.8 below.
As expected, the gain increases linearly with V_{bias}. On the documentation for this device the nominal gain is specified to be equal to:

$$M = 1.80 \cdot 10^6 \quad for \quad V_{bias} = 54.8V, \tag{3.3}$$

from the linear regression on the line of best fit:

$$M = p_0 + (V_{bias} \cdot p_1), \tag{3.4}$$

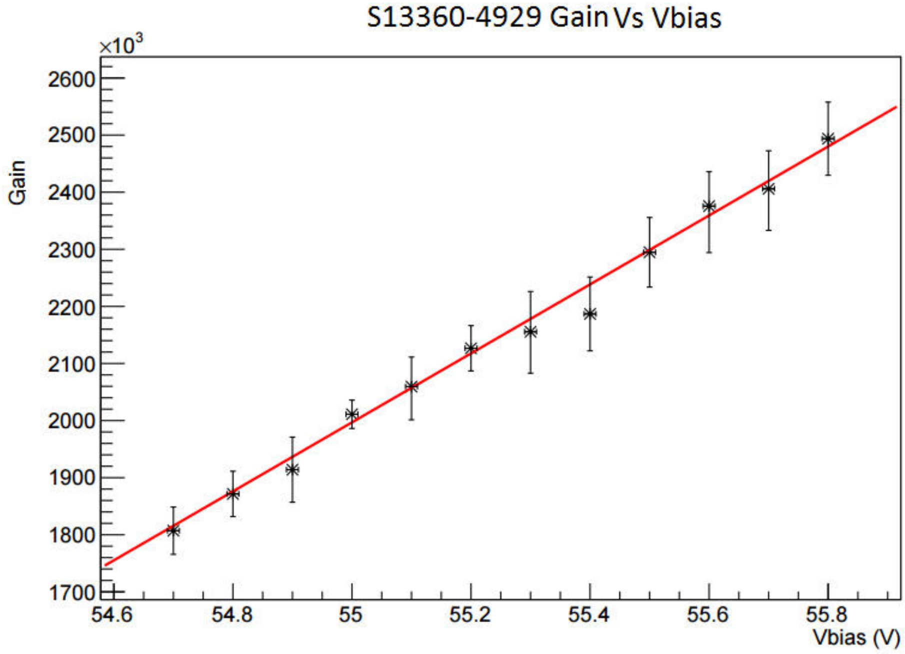

Figure 3.8: Graph of gain versus V_{bias} for the new generation SiPM S13360-4929

where p_0 is the intercept of the line and p_1 is its slope, we calculated the gain with its error[4]:

$$M = (1.8759976 \pm 0.0397718) \cdot 10^6 \; for \; V_{bias} = 54.8V, \tag{3.5}$$

in good agreement with the value provided by the manufacturer.

3.2.2 Dark Counts Rate and Other Noise Sources

Noise in SiPMs is represented by spurious output current pulses produced in absence of light. In silicon, there is a finite probability for carriers (electron and hole) to be generated by thermal agitation. During the quiescent mode, if an electron or hole originates inside the active region of a GM-APD an avalanche is initiated and an output pulse is observed. This is called a "dark event". The number of dark events per unit time is the **dark count rate** (DCR). In silicon photomultipliers, the thermal generation of carriers doubles approximately every 10°C, and so does the DCR. Moreover, the DCR scales according to the SiPM area, it is an increasing function of the overvoltage, depends on the pixel's size and even on the quality of

[4]The following formula has been used for errors propagation: $\Delta f = \sqrt{\sum \left(\frac{\delta f}{\delta x_i} \cdot \Delta x_i \right)^2}$, where f is a funcion of n variables $f = f(x_1, x_2 ... x_n)$ and Δx_i is the uncertainty on the i-th variable

the semiconductor wafer.
In a single GM-APD a dark event is indistinguishable from a photo-generated one. In both cases, the output pulse has 1 p.e. amplitude. In a SiPM, dark events still have 1 p.e. amplitude (neglecting direct optical crosstalk events, discussed below) while the useful signal may consists of more photons impinging on the detector at the same time producing signals with amplitude greater than 1 p.e. In this case, a threshold can be set to, e.g., 1.5 p.e. to discard the dark events.
Besides this primary noise, in SiPMs there are other two sources of noise, i.e., **afterpulsing** (AP) and **optical crosstalk** (OC). Both AP and OC events originate from an existing current pulse (which can be either a photonevent or a dark-event) and for this reasons they are referred as to "correlated noise". The probability of having an AP or OC event strongly depends on the current density in the original avalanche and on the triggering probability. Large micro-cells have large gain, hence a high number of carriers flowing during the avalanche and thus high AP and OC probability. To contain the correlated noise it is essential to implement SiPMs with small micro-cells [30].
Afterpulsing is due to the carriers trapped in silicon defects during the avalanche multiplication that are released later on during the recharge phase of the GM-APD. It occurs when a secondary avalanche forms in a pixel that is recovering from a photon- or dark-noise-induced primary avalanche. So this secondary avalanche occurs some time t_A after the primary avalanche starts.
The net effect is that we observed a new current pulse on the tail of the original current pulse (fig. 3.9). AP probability increases more than linearly with the overvoltage and quadratically with the cell size because of the corresponding increase in the gain.
The amount of charge generated in an afterpulse is proportional to the area under the secondary waveform (i.e. the afterpulse itself) with respect to the primary waveform. The amount of charge increases with t_A, and for sufficiently long t_A when the pixel completely recovers, the afterpulse waveform becomes indistinguishable from the 1 p.e. waveform. In this case, afterpulsing erroneously increases the number of 1 p.e. events in photon counting, which translates into an erroneous increase in Photon Detection Efficiency (PDE; described in greater detail below). Afterpulsing also increases the recovery time of the fired pixel, which degrades the time resolution characteristic of an SiPM.
The likelihood of afterpulsing increases with increasing V_{OV} because the stronger electric field in the avalanche region more effectively dislodges the trapped charges and also increases avalanche probability.

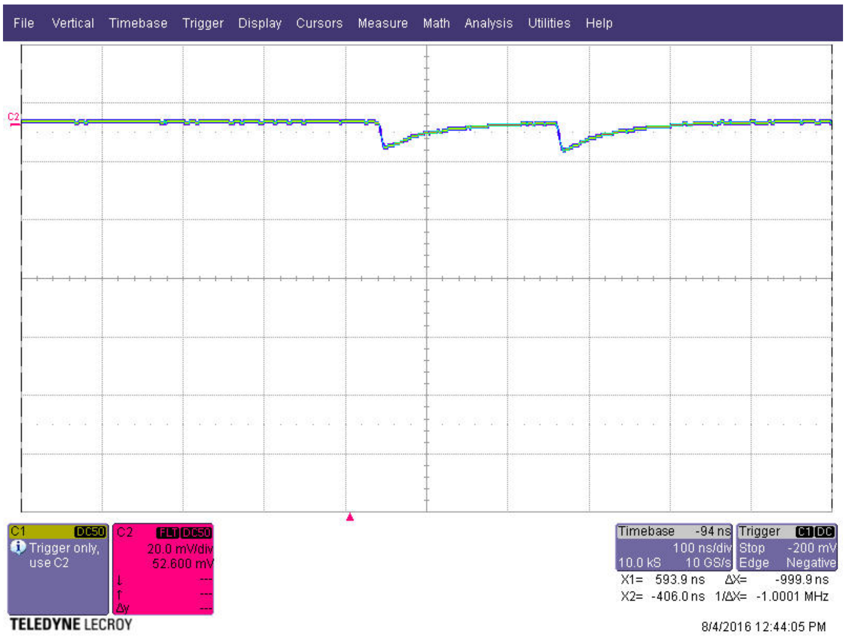

Figure 3.9: Example of afterpulse on the signal produce by the Hamamatsu SiPM S13360-4929-A00013 at its V_{OP} = 54.8V. Printscreen from the Lecroy Wave Runner 104 MXi 1GHz Oscilloscope

Optical crosstalk (fig. 3.10) involves photons emitted during avalanche multiplication and that are re-absorbed in neighboring cells or even in the inactive region of the same cell and causing additional current pulses. Three distinct processes for light emission contribute to the observed crosstalk. Indirect interband recombination between electrons and holes in strong electric fields is primarily responsible for the emission of photons with energy below ∼2 eV. Bremsstrahlung radiation due to scattering of conduction electrons from positive ions is mainly responsible for emission of photons of energy between ∼2 eV and ∼2.3 eV. Interband recombination between hot[5] conduction electrons and holes is responsible for the emission of radiation above 2.3 eV [37].
Direct OC occurs when an emitted photon reaches the active region of another cell triggering an additional avalanche practically at the same instant of the original avalanche (consider the speed of light in silicon and the very rapid avalanche ignition in GM-APDs).

[5]Hot carrier injection (HCI) is a phenomenon in solid-state electronic devices where an electron or a hole gains sufficient kinetic energy to overcome a potential barrier necessary to break an interface state. The term "hot" refers to the effective temperature used to model carrier density, not to the overall temperature of the device

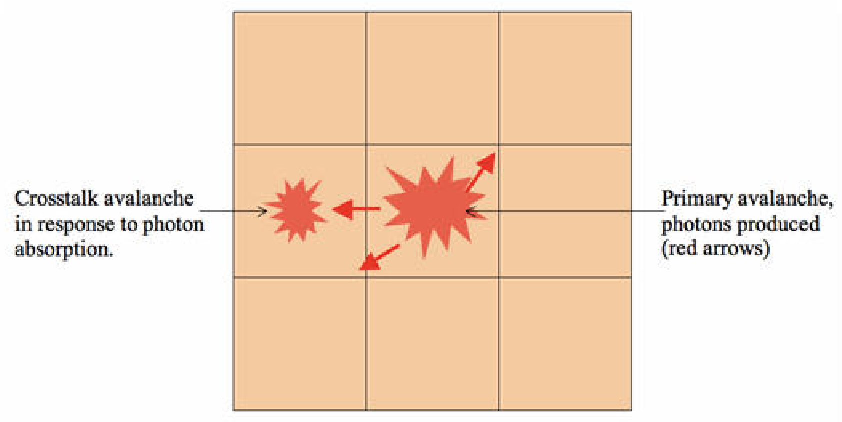

Figure 3.10: The mechanism of cross-talk. An avalanche in the central pixel produces photons energetic enough so that a correlated avalanche in a neighboring pixel can occur as a result of the photon absorption

The result is the multiple pulse in figure 3.11. Delayed-OC involves, instead, photons that are re- absorbed in the inactive regions of the SiPM.

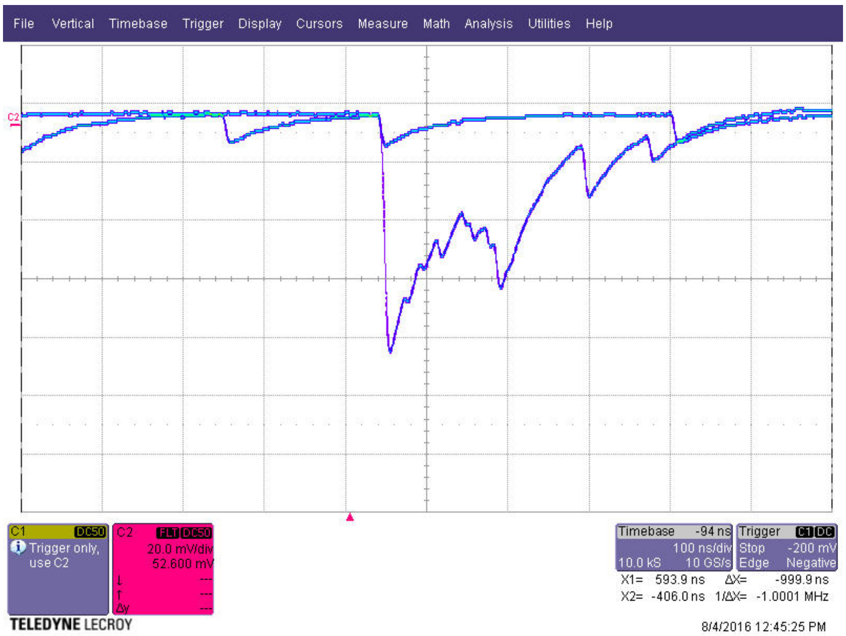

Figure 3.11: Example of the combination of afterpulse with optical crosstalk on the signal produce by the Hamamatsu SiPM S13360-4929-A00013 at its V_{OP} = 54.8V. Printscreen from the Lecroy Wave Runner 104 MXi 1GHz Oscilloscope

The generated electron (or hole) must then diffuse to the active region of a cell before being able to trigger an avalanche. The correlated pulse has therefore a certain time-delay (in the order of few ns) with respect to the original one.
Since the emission of photons is isotropic, this event has a small probability. Moreover, some fraction of the photons will be absorbed in the pixel from which they were emitted, possibly causing afterpulsing in the pixel. The time for a photon to cross a pixel of size d is

$$tc \sim \frac{n \cdot d}{c}, \tag{3.6}$$

where n is the index of refraction of the material. For silicon n = 3.96; thus, for d = 25 μm, tc = 0.33 ps. This crossing time is much shorter than pixel recovery time (typ. ∼15 ns) and, therefore, the SiPM would output at least a 2 p.e. waveform in response to a single external photon. The value of tc scales linearly with d, but even for a 100 μm pixel, it is still small compared to pixel recovery time. Nevertheless, the probability of cross-talk decreases with pixel size because the emitted photon has an increasing chance of being reabsorbed in the same pixel.
As for AP, in first approximation OP probability increases more than linearly with the overvoltage and quadratically with the cell size. The effect of both AP and OC is to produce additional charge with respect to the charge associated to an original SiPM pulse (photon-event or a dark-event). Recent technological innovations enabled us to drastically reduce the crosstalk, by means of the inclusion of optical insulation structures between one cell and the other (fig. 3.12).

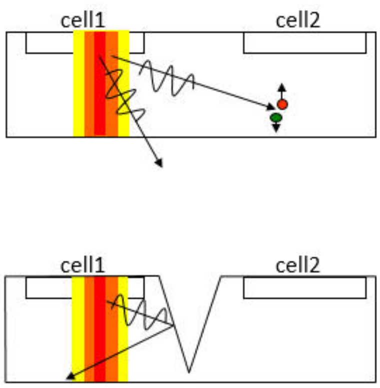

Figure 3.12: Optical insulation structure between cell 1 and cell 2. The secondary emission photon produced in cell 1 is reflected back in the cell 1

We measured the dark counts rate of the two SiPMs S10943-3360 and S13360-4929 as a function of the supply voltage in order to obtain a complete characterization of them both. The results of these measurement have then been compared.

The experimental set-up is the same shown in figure 3.6 keeping the laser off, so the SiPM was in dark. Then we sent the output signal to the oscilloscope and set the trigger on the signal itself. Our oscilloscope is equipped with a function that measures the elapsed time between a trigger event and the next ($\delta trig$), and a feature called "Trigger Holdoff" that lets the user ignore n trigger events, with n set as desired, and stabilize the display as though there were only one trigger event per acquisition. By fixing n and measuring the $\delta trig$ between the event 0 and the event n, the event rate R is obviously given by:

$$R = \frac{Holdoff}{\delta trig}. \tag{3.7}$$

We set the holdoff so that the elapsed time between a trigger event and the next was always ∼100 ms and then we varied the supply voltage between 66.7V and 68.1V for S10943-3360 SiPM and between 54.4V and 56.8V for S13360-4929 SiPM in steps of 0.1V; for each step we acquired 1000 measures for $\delta trig$ and calculated their mean and standard deviation. For each V_{bias} we performed measures setting 3 different trigger tresholds: 0.5 p.e., 1.5 p.e. and 2.5 p.e.; the results of these measurements are shown in figure 3.13.

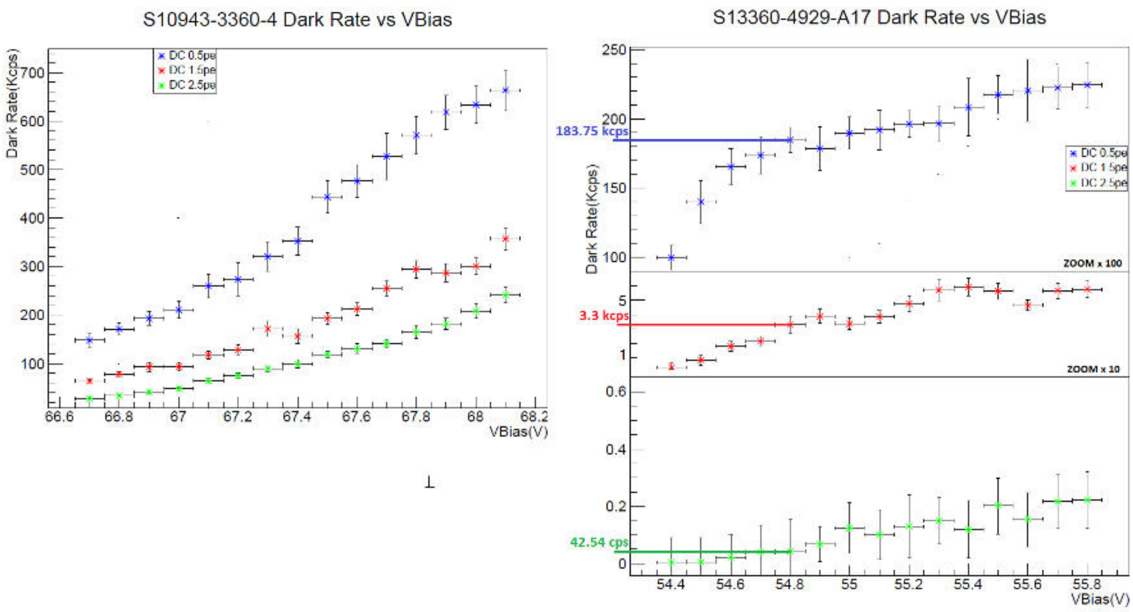

Figure 3.13: Comparison between S10943-3360 (left, old generation SiPM) and S13360-4929 (right, new generation SiPM) dark noise rate as a function of the overvoltage

Measurements performed at 0.5 p.e. threshold provide an estimate of the total noise rate, inclusive of dark counts and thermal crosstalk events.
Measurements performed at 1.5 p.e. treshold and low V_{bias} should provide an estimate of the rate of events due to cross talk only. This is because at 22°C temperature the probability that two pixels simultaneously generate a pair for thermal agitation should be low; and even if that happens, for small V_{OV}, the probability that both the electrons produced are able to trigger the Geiger avalanche is negligible. So in these conditions 2 p.e. magnitude dark signals should be almost exclusively due to cross talk.
Measurements performed at 2.5 p.e. treshold, finally, allowed us to verify that the rate of events of greater than or equal to 3 p.e. amplitude was only relevant at high voltages (but just for the S10943-3360).

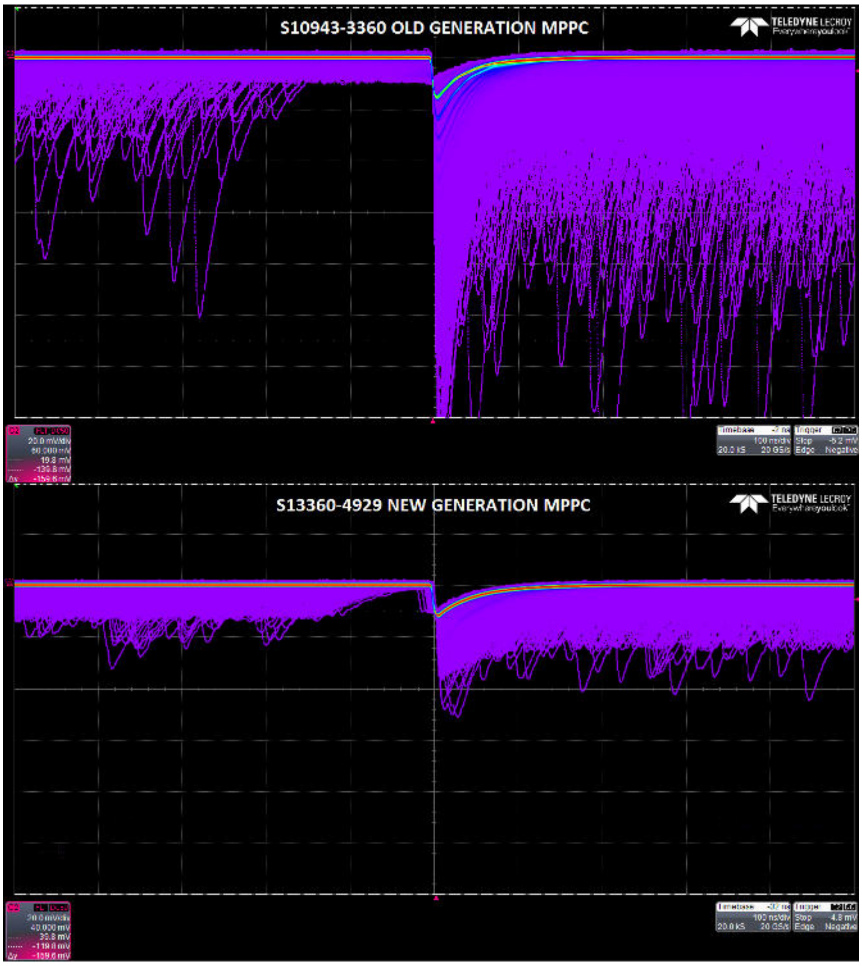

Figure 3.14: Comparison between S10943-3360 (up, old generation SiPM) and S13360-4929 (down, new generation SiPM) output signals in dark

From the comparison between the two generations SiPMs, is self-evident that with the new generation device Hamamatsu has broken down the rate of dark counts of almost an order of magnitude (fig. 3.14), despite the fact that the two devices have the same dimensions and the same number of cells. Indeed the contribution of secondary noise in S13360-4929 in the overall dark noise rate is practically negligible (a few tens of counts per second), even for high overvoltage values (V_{bias} = 1V over V_{OP}). This upgrade is due to the use of better quality materials and a more advanced bulk construction process for the new generation device.

3.2.3 Photodetection Efficiency Estimate and Linearity

The photon detection efficiency (PDE) is the probability that a photon arriving on the SiPM surface is detected producing an output pulse. It can be defined as the ratio between the number of detected photons over the number of incoming photons. In terms of device characteristics, the PDE is defined as the product of three factors: quantum efficiency, triggering probability, and geometric efficiency:

$$PDE(V_{OV}) = Qe \cdot Pt(V_{OV}) \cdot FF. \tag{3.8}$$

Quantum efficiency (Qe) expresses the probability that a photon impinging on the SiPM is actually transmitted to the silicon, absorbed in the silicon and finally converted in an electron/hole pair. Qe is a function of the wavelength and angular incidence of incoming photons.
The triggering probability (Pt) is the probability that the generated electron/hole pair successfully initiates a self-sustaining avalanche process and thus an output current pulse. Pt is a strong function of the overvoltage, and it increases with V_{OV} according to the electron and hole ionization rates dependence on the induced electric field [31]. Also Pt is wavelength-dependent since the avalanche initiation probability depends on the position inside the G-APD where the electron/hole pair has been generated and this, in turn, depends on the wavelength of the incoming photon. The geometric efficiency (or fill-factor, FF) accounts for the fact that each micro-cell in the SiPM has necessarily some dead area on its periphery to accommodate isolating structures and metal lines for signal routing. It is defined as:

$$FF = \frac{Active\ area}{Total\ area}. \tag{3.9}$$

The main limiting factor in the PDE is the fill-factor: for sufficiently high overvoltage, indeed, both Qe and Pt are closed to 1 and PDE eventually saturates to FF.
By definition, we have $0 < Qe, Pt, FF < 1$. To maximize PDE, each of its three

factors shall be optimized: improvements of the Qe are achieved by means of proper anti-reflecting coating layers deposited over the SiPM active area; Pt is maximized recurring to junction and electric field engineering [32]; to enhance cells fill-factor one must recur to advance lithography techniques with submicron feature size and clever device layout [34].
PDE is an indispensable factor in the determination of the linear response of a SiPM device. An ideal photodetector would produce an electrical output that is linearly proportional to the entire range of input light levels. This property, referred to as **linearity**, is a highly desirable feature in practical photodetectors but it is never realized for all signal levels. Noise inherent to a detector limits the lowest detectable light level, whereas a variety of phenomena that are unique to the detector, cause a non-linear behavior and eventually saturation at high light levels. Dynamic range is a ratio of the maximum light level that a detector can detect without saturation or deviation from linearity and of the minimum detectable light level, which would produce.
Each cell detects only whether or no (regardless) one or more photons have entered the detector, and hence the total number of the fired pixels does not directly correspond to the number of detected photons. If two or more photons are triggering one pixel then the photon detection linearity degrades because the number of incident photons is larger than the number of fired pixels [35].
A linear response of silicon photomultiplier (SiPM) devices depends on total number of pixels, their effective dead time and width of the detected light pulse [36]. For a light pulse shorter than the effective dead time, given the total number of available cells (N_{cells}) of the SiPM, the response of SiPMs (that is the number of fired cells (N_{pe}) as a function of the number of incident photons (N_{ph}) and of the PDE) is given by the following formula:

$$N_{pe}(N_{cells}, \lambda, V) = N_{cells} \cdot \left[1 - e^{\frac{-N_{ph} \cdot PDE(\lambda, V)}{N_{cells}}} \right]. \tag{3.10}$$

This exponential trend accounts for the fact that that the number of detected photons is proportional to the number of incident photons, but always less than it. Moreover the answer is linear in low light conditions, but begins to deviate from linearity when the number of incident photons becomes high; this is the obvious consequence of the fact that the pixels are finite in number and thus two or more photons can hit the same pixel.
In this section we will present the results of a linearity measurement performed on a latest generation SiPM: the S13360-4929. This measure is intented as a test to have a check of the phenomenology linked to the SiPM response with respect to variations in the number of input photons.
The experimental set-up for this measure is the same descripted at the beginning

of this chapter, arranged as in figure 3.15:

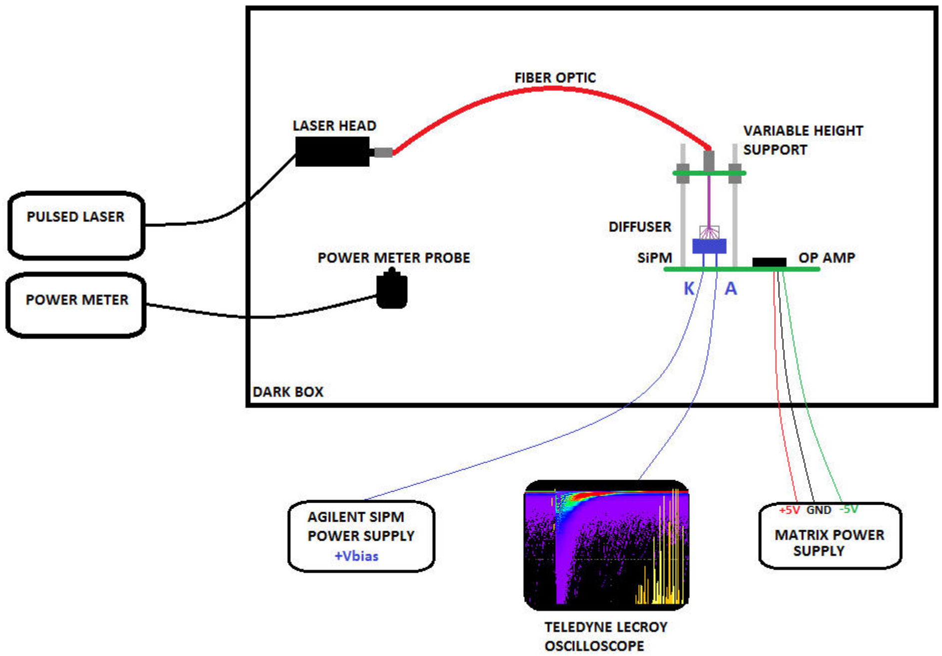

Figure 3.15: Schematic view of our experimental set-up

With this experimental set-up we first performed the calibration of the optical fiber used, by measuring the power of the light beam emitted from the laser through it with a power meter. This characterization was performed varying the power of the laser and at various distances between the output of the optical fiber and the entrance of the power meter probe.
Since the power meter probe has a circular entrance of 1 mm diameter (so πr^2 = 0.8 mm^2 area), but we were interested to know the power of the beam that reaches the area of the 3 mm diameter diffuser (so πr^2 = 7.1 mm^2 area), each power measured should be multiplied by a factor:

$$\frac{Diffuser\ area}{Power\ meter\ probe\ area} = 9. \tag{3.11}$$

This measure was necessary to know the number of photons that we were sending from time to time to the SiPM once fixed distances and power of the laser.
The number of photons $N_{photons}$ contained in a laser beam of known power P_{beam} and wavelength λ, and given frequency of the pulses ν_{laser} is:

$$N_{photons} = P_{beam} \cdot \frac{\lambda}{h \cdot c} \cdot \frac{1}{\nu_{laser}} \tag{3.12}$$

Our laser is Gaussian, so its intensity profile in a plane perpendicular to the propagation direction (or better its spot) follows a Gaussian distribution (fig. 3.16 left). This fact obviously limits our capability of focusing uniformly photons over the whole SiPM surface. To solve this problem we put a 3 millimeters diameter opal duffusing glass on the SiPM surface. This device have one surface flashed with a milky white opal coating which allows it to diffuse light evenly so it can be used to achieve a near Lambertian distribution[6] (fig. 3.16 right) so we were more or less guaranteed to illuminate the entire surface of the SiPM uniformly.

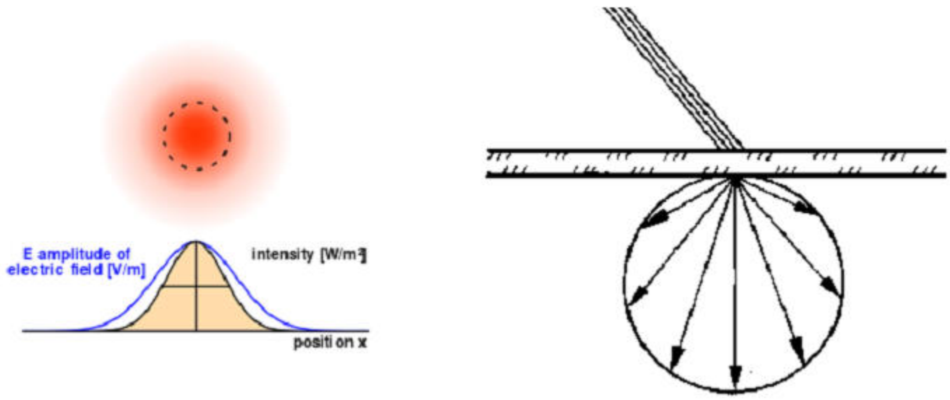

Figure 3.16: On the left: transverse intensity profile of a Gaussian beam that is propagating out of the page. Blue curve: electric (or magnetic) field amplitude vs. radial position from the beam axis. The black curve is the corresponding intensity. On the right: radiation pattern for diffuse photons passing through the diffusing glass

However, the level of diffusion in the opal glass causes a large amount of scattering loss. Indeed, using the power meter, we measured the optical power of a light beam with and without the opal diffusing glass placed in front of the entrance of the probe. From this test we found that the diffuser cuts $\sim 70\%$ of the initial beam, then only $\sim 30\%$ arrives on the SiPM surface.
Moreover, the diffuser area is 7.1 mm^2 but the SiPM's area is 9 mm^2 (fig. 3.17), so the diffuser does not cover the entire detection area of the SiPM.

[6]See appendix A for more details

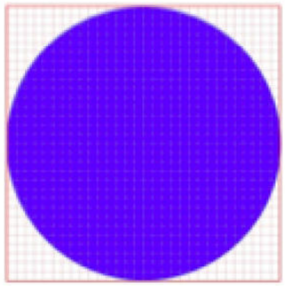

Figure 3.17: Area of the SiPM covered by the diffuser

From the following simple relation:

$$N_{cells} : Area_{SiPM} = x : Area_{diffuser}, \tag{3.13}$$

we calculated the actual number of cells stricken by photons = 2840.
Taking account of these considerations, we proceeded to the measurement of the SiPM response by targeting it with the light beam outgoing from the optical system described above, setting 100kHz frequency on the light pulser, for a range of incident photons that goes from a maximum of 23819 to a minimum of 155 for every pulse[7], suppliyng the SiPM with its operation voltage (V_{OP} = 54.8V) and setting the trigger on the laser output signal.
But, when we turned on the SiPM in high light levels conditions, another problem emerged: the output signals from the SiPM for a high number of incident photons (from 1000 incident photons) is greater than 5V. But 5V is the dual power supply voltage of the amplifier and of course it is impossible that the amplifier can produce on its output a voltage signal larger than its own supply voltage. Indeed the signal displayed on the oscilloscope appeared neatly cut close to 5V (fig. 3.18).
To remedy this other problem, we have lowered the gain of the operational amplifier replacing its feedback resistor (1500 Ω) with a lower value resistor (220 Ω). So, referring to figure 3.5, the new amplification factor is given by:

$$G = \frac{R_f}{R_2} = \frac{220\Omega}{75\Omega} = 2.93 \tag{3.14}$$

In this configuration the first peak amplitude is no more 10mV but 1.5 mV and, for the maximum number of incident photons in this set-up, the signal read from the oscilloscope have an amplitude of 4.114 V, so it was far enough away from the supply voltage of the operational amplifier as not to be cut.
At this point we were able to perform the measurement descripted above, so we have set the oscilloscope trigger on the signal coming from the laser and then we

[7]Thi aim was achieved by changing the output power of the light pulser

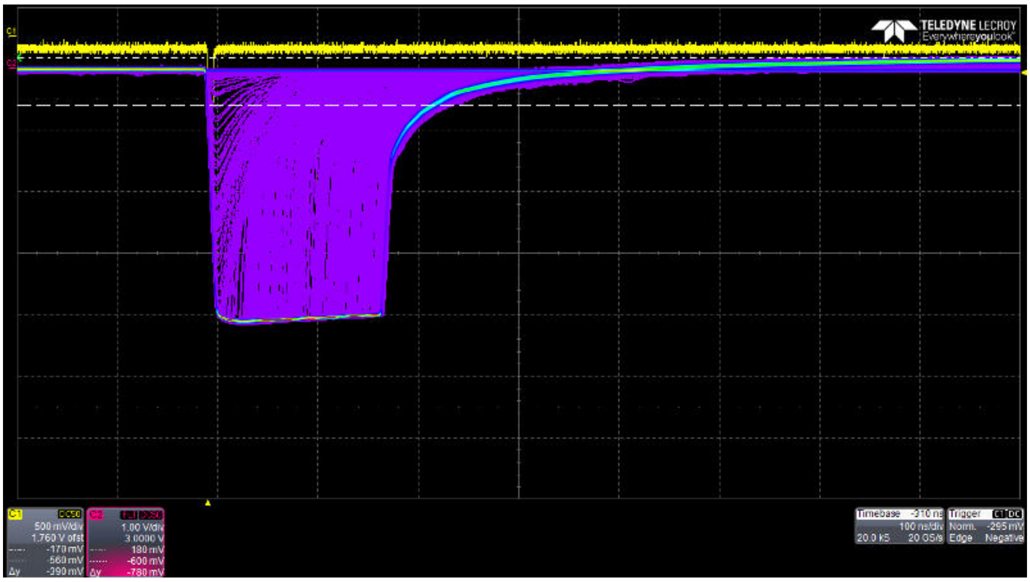

Figure 3.18: Saturated SiPM's output signal

measured the amplitude of the SiPM's output signal. We acquired 10000 measurements of the signal amplitude and we considered the average of these, with its standard deviation. This procedure was repeated varying the output power of the laser and, therefore, the number of photons per pulse sent on the SiPM. Assuming that all pixels SiPM have the same behavior, the number of pixels fired is given by:

$$N_{fired} = \frac{\textit{Signal Amplitude}}{\textit{1 p.e. Amplitude}}, \tag{3.15}$$

where the 1 p.e. amplitude, measured by means of the oscilloscope, is 1.5 mV. The graph in figure 3.19 shows the number of fired pixels versus the number of incident photons (so the SiPM response). The experimental data have been fitted with the following two parameters curve:

$$y = a \cdot \left(1 - e^{\frac{-b \cdot x}{a}}\right), \tag{3.16}$$

As we expected, for a large number of incident photons, the upper limit of the dynamic range has been reached, the response of the SiPM patently deviates from linearity and the saturation occurs.

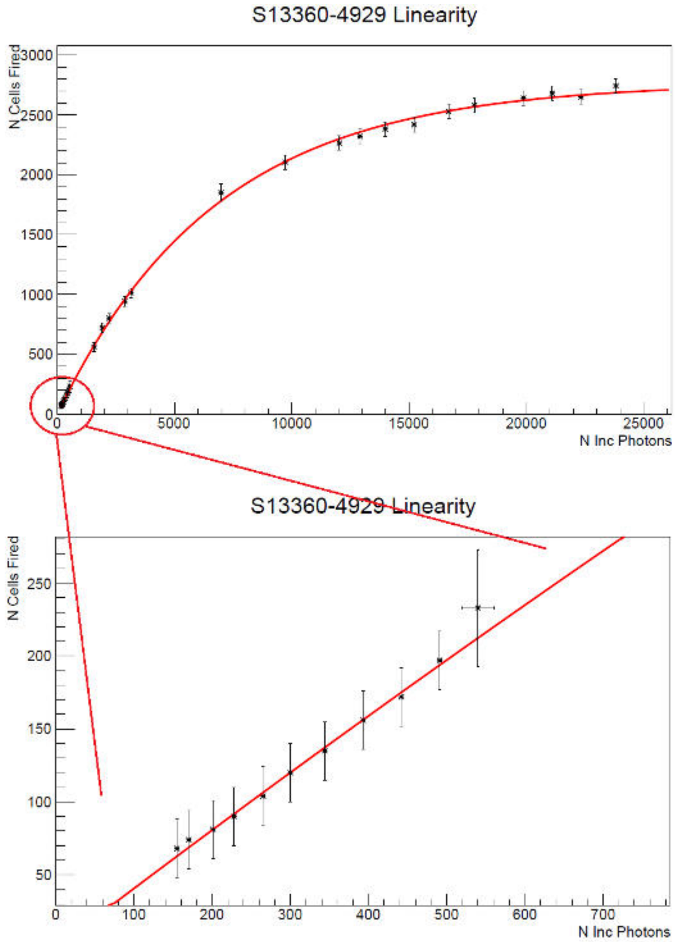

Figure 3.19: Number of fired pixels as a function of the number of incident photons with a zoom on the linear part of the curve

The two parameters a and b provide the total number of the SiPM cells and its PDE respectively:

$$a = N_{cells} = 2769 \pm 32 \tag{3.17}$$

$$b = PDE = (40.9 \pm 0.9)\% \tag{3.18}$$

The value of the parameter a is very near to the total number of illuminated cells (2840 as discussed above) and since the PDE provided by the SiPM's datasheet is 40% the value of the parameter b is in very in good agreement with the nominal value.

3.3 Final Considerations

The detailed analysis we have done is needed to describe the state of art for silicon detectors in order to choose the core device for the realization of the next VSiPMT prototype.
The SiPMs examined in this chapter are designed specifically to a correct operation of the VSiPMT, indeed they are windowless and p-over-n type. In particular we have seen that the latest generation devices, belonging to the S13360 series, offer superior performances in terms of dark rate and requires a lower operation voltage. Very recently further improvements have been made in this series, indeed by July 2016 the S13360-(x)VE are on the market (fig. 3.20).

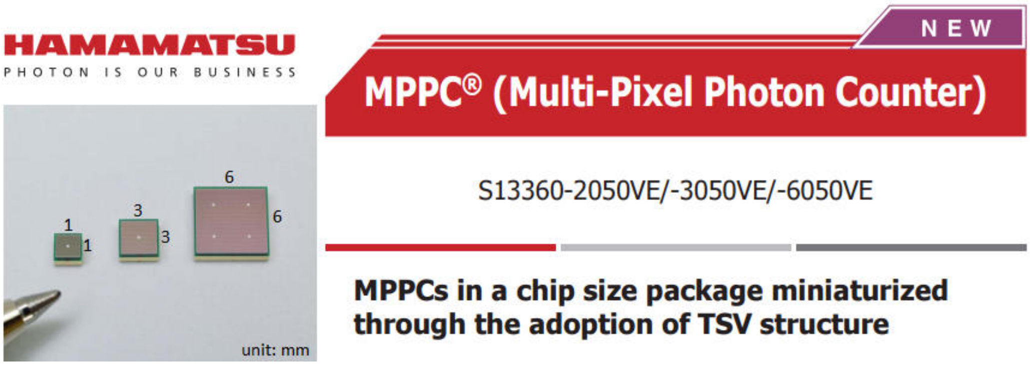

Figure 3.20: Very latest Hamamatsu MPPCs' datasheet

These are devices optimized for precision measurements miniaturized by the use of TSV (through-silicon via) and CSP (chip size package) technologies. The adoption of the TSV structure made possible to eliminate wiring on the photosensitive area side. Since no electrode space for wire bonding is needed, the gap between the package edge and the SiPM photosensitive area around the outer periphery is reduced to 0.2 mm on the four sides, allowing a four-side buttable arrangement. This results in a compact structure with little dead spaces compared to previous products. Moreover, this four side buttable structure allows multiple devices to be arranged side by side to fabricate **large area devices**.
In particular we are interested in the S13360-6050VE, that is optimized for medical imaging and high-energy particle detection, measurements which require photon counting in low light level conditions. Its characteristics are summarized in figure 3.21. It has a very large number of cells (14336) but at the same time a high fill factor (74%). This allows to greatly expand the dynamic range without affecting the PDE, which remains the same as the device had 3500 cells (40%).
The only drawback of this device is the high dark counts rate (2 Mcps at 0.5 p.e. treshold), obviously due to the large number of cells. However, in a realistic

Parameter		Symbol	S13360 -2050VE	S13360 -3050VE	S13360 -6050VE	Unit
Effective photosensitive area		-	2 × 2	3 × 3	6 × 6	mm
Pixel pitch		-		50		μm
Number of pixels		-	1584	3584	14336	-
Fill factor		-		74		%
Package		-		Surface mount type		-
Window		-		Epoxy resin		-
Refractive index of window material		-		1.55		-
Spectral response range		λ		320 to 900		nm
Peak sensitivity wavelength		λp		450		nm
Photon detection efficiency (λ=λp)*3		PDE		40		%
Dark count*4	Typ.	-	0.3	0.5	2	Mcps
	Max.		0.9	1.5	6	
Terminal capacitance		Ct	140	320	1300	pF
Gain		M		1.7×10^6		-
Breakdown voltage*5		VBR		53 ± 5		V
Recommended operating voltage		Vop		VBR + 3		V
Temperature coefficient of recommended operating voltage		ΔTVop		54		mV/°C

Figure 3.21: Electrical, optical and structural characteristics of the S13360-6050VE at 25°C evidenced in purple

experiment unlikely we would have to disclose a single photon. So we can choose a higher treshold for our trigger (4 or 5 p.e.) and cut away this noise.

Chapter 4

The Temperature Issue

As we have seen in the previous part, astroparticle detection in our area of interests is based on phenomena related to light emission. To obtain better measurement conditions facilities, experiments and laboratories involved in astroparticle physics have to be put in places that can ensure the lowest possible light pollution, such as:

- the top of a mountain (like the telescope MAGIC[1] that is situated on the Roque de los Muchachos on La Palma, one of the Canary Islands);
- the middle of a desert (like the High Resolution Fly's Eye or HiRes detector, in the western Utah desert in the USA);
- the space (like PAMELA[2], mounted on the upward-facing side of the Resurs-DK1 Russian satellite);
- under ice (like IceCube, a neutrino telescope constructed at the Amundsen-Scott South Pole Station in Antarctica, its thousands of sensors are distributed over a cubic kilometre of volume under the Antarctic ice);
- under the sea (like KM3NeT[3], a neutrino telescope located in the deepest seas of the Mediterranean).

These locations (especially the desert, the space and the mountain) are characterized by large temperature variations and, since the detectors of our interest are based on semiconductor devices technology, efforts must be devoted to temperature compensation issues.

[1]Acronym for: Major Atmospheric Gamma-ray Imaging Cherenkov Telescope
[2]Acronym for: Payload for Antimatter Matter Exploration and Light-nuclei Astrophysics
[3]Acronym for: Cubic Kilometre Neutrino Telescope

4.0.1 SiPM Characterization in Temperature With a Standard Power Supply

As we have seen in the first part of this thsis, semiconductor devices are extremely sensitive to temperature changes. In particular in a constant temperature environment, the overvoltage V_{OV} applied to a SiPM determines its operational characteristics such as gain and PDE. But, since temperature affects the opto-electrical characteristics of a p-n junction such as the width of the depletion region, the breakdown voltage, band-gap energy, resistivity, and more, the operation of a SiPM will be strongly affected by this parameter. An example of this dependence is the recovery time of a pixel from avalanche. The characteristic recovery time is the RC time constant determined by the values of the junction capacitance Cd and of the quenching resistor Rq. For a given V_{OV}, temperature affects the width of the depletion region and, thus, Cd. It also affects the resistance of the polysilicon quenching resistor Rq. Thus, the product of these two quantities can also change with temperature affecting the recovery time.
To verify the overvoltage's temperature dependence, we have performed a study on the SiPM family S10931-100P that consisted in a current-voltage characterization under temperature variations. The experimental set-up consists of the following instrumentation:

- Angelantoni's environmental test chamber;
- Keithley picoammeter;
- Agilent power supply;
- The SiPM S10931-100P;
- A program written in LabVIEW that interfaces with the picoammeter and with the power supply.

In order to perform this test we connected the SiPM's anode to the power supply and the cathode to the picoammeter (fig. 4.1). Since we wanted to show that the breakdown voltage of the SiPM depends on the temperature, we were interested in studying the behavior of the SiPM in the region of its characteristic V-I curve corresponding to the reverse bias region. So we sent a negative voltage to the anode with respect to the cathode, in order to have a reverse biased SiPM.
Since our SiPM datasheet do not provide the device's breakdown voltage but just a recommended operating voltage V_{OP}, we will refer to the latter characteristic quantity for the following analysis.
We set the environmental chamber so that its internal temperature varied from

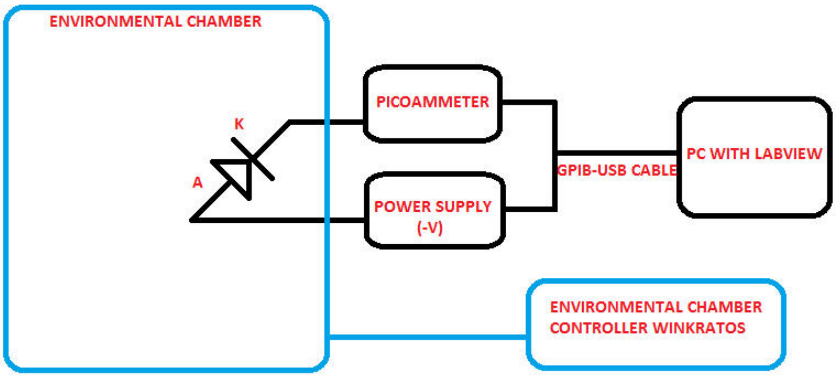

Figure 4.1: Schematic configuration of the experimental set-up for the V-I curve versus temperature test.

45°C to 5°C in steps of 5°C, and for every step we performed a V-I curve characterization in a voltage range that goes from 50V to 73.8V (so with a 2V overvoltage since the SiPM we have characterized had V$_{OP}$=71.8V).
Then we put all these curves on the same graph and the result of this characterization is shown in figure 4.2.
For all these measures the environmental humidity has been set to 20%.
Then, we considered the current level corresponding to the V$_{OP}$ of the characteristic curve at 25°C (it was 2.686279 μA) and we saw which were the values of the voltage corresponding to this current on the other curves tracing the orizontal intercept on the graph. We put these values in a graph where X-axis shows temperatures set from time to time in the environmental chamber and Y-axis shows voltage levels corresponding to 2.686279 μA current for each curve. The result of this operation is shown below (fig. 4.3)
The graph clearly shows what we already expected, i.e. the fact that the V$_{OP}$, or equivalently the SiPM's breakdown voltage, increases with temperature and, in the temperature range explored for this analysis, this increase is linear with a slope $\frac{\Delta V}{\Delta T}$= (55.5077 ± 0.5274) mV/°C, in good agreement with the nominal value provided by the datasheet ($\frac{\Delta V}{\Delta T}$= 56 mV/°C). The consequences of this behavior will affect the gain of the device. Indeed, as we saw in the previous part, the gain of a SiPM is given by the following formula:

$$G(V_{OV}) = \frac{C_d \cdot V_{OV}}{e} \tag{4.1}$$

Gain is directly proportional to V$_{OV}$. We just saw that, at a given fixed bias, the breakdown voltage increases with temperature so, since by definition V$_{OV}$ is given by:

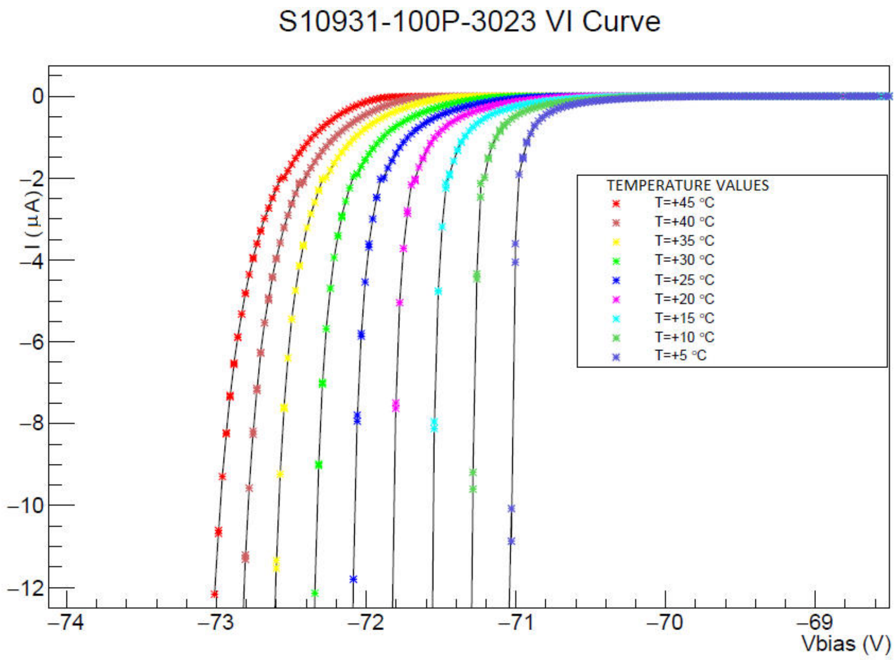

Figure 4.2: V-I curves of the SiPM S10931-100P-3023 performed under temperature variations

$$V_{OV} = V_{bias} - V_{BD}, \tag{4.2}$$

we expect that **the gain decreases with increasing temperature**. To verify this fact we have performed a study on the SiPM family S10931-100P that consisted in a gain characterization under temperature variations.
The experimental set-up consists of the following instrumentation arranged as in figure 4.4:

- Angelantoni's environmental test chamber;
- Electronic board made ad hoc for the SiPM's signal amplification on which the SiPM and a current voltage amplifier are mounted;
- DC voltage generator Agilent 0.1V sensitivity mod. E3612A used as a power supply for the SiPM;
- DC voltage generator Matrix mod. MPS-3005-L-3 used as a dual power supply for the signal amplifier mounted on the electronic board;
- Digital Teledine LeCroy serial data analyzer mod. SDA 760Zi-A, 4 input channels, 6 GHz bandwidth with 40 GS/s sample rate.

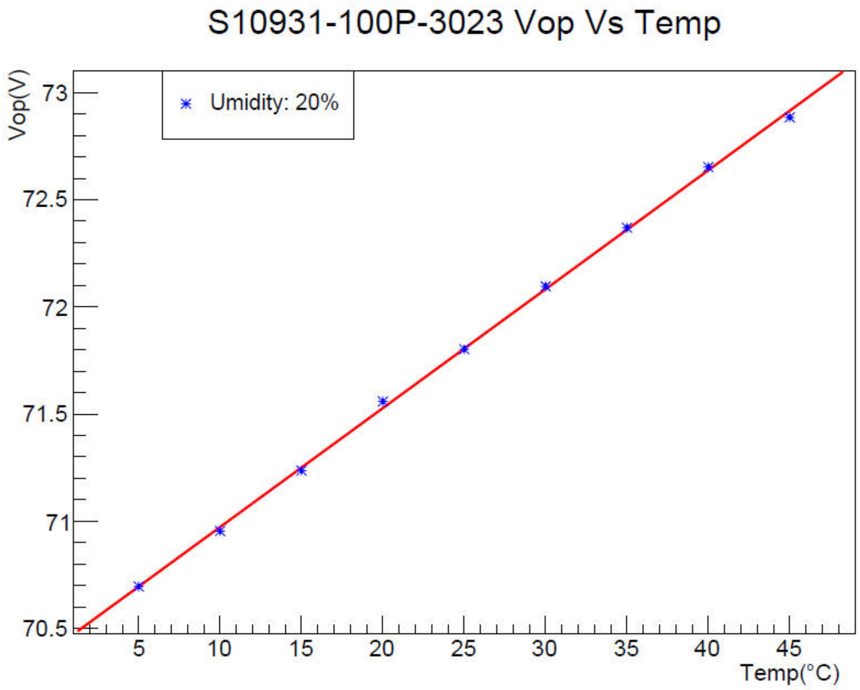

Figure 4.3: V_{OP} versus temperature variations

- The SiPM S10931-100P;

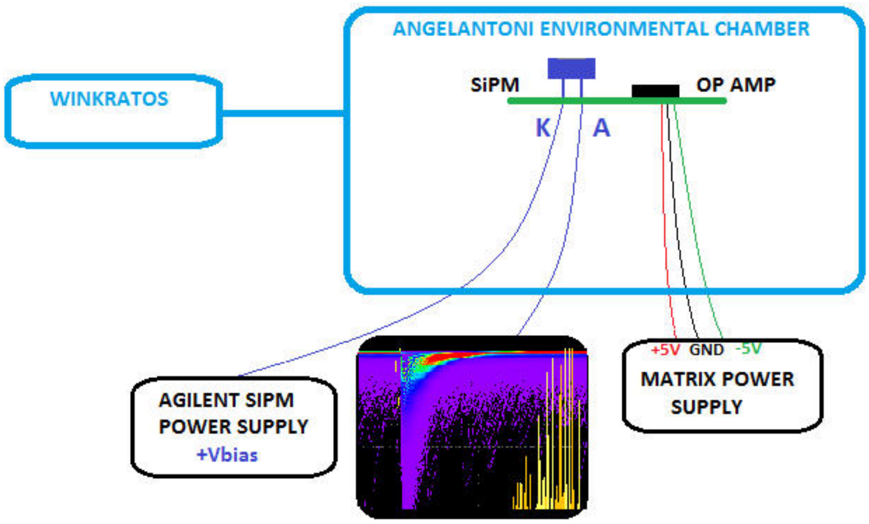

Figure 4.4: Schematic view of our experimental set-up

Fixed the V_{bias} at the device's V_{OP} (71.8V) this measurement was performed by varying the value of the environmental tempeature between 5°C and 45°C by 5°C steps by means of the environmental chamber. The data acquisition and analysis was performed following the same procedure described in section 3.2.1, with the difference that this time the SiPM was in dark so we set the trigger on the signal itself at 0.5 p.e. The results of this analisys are shown in the graph below (fig. 4.5).

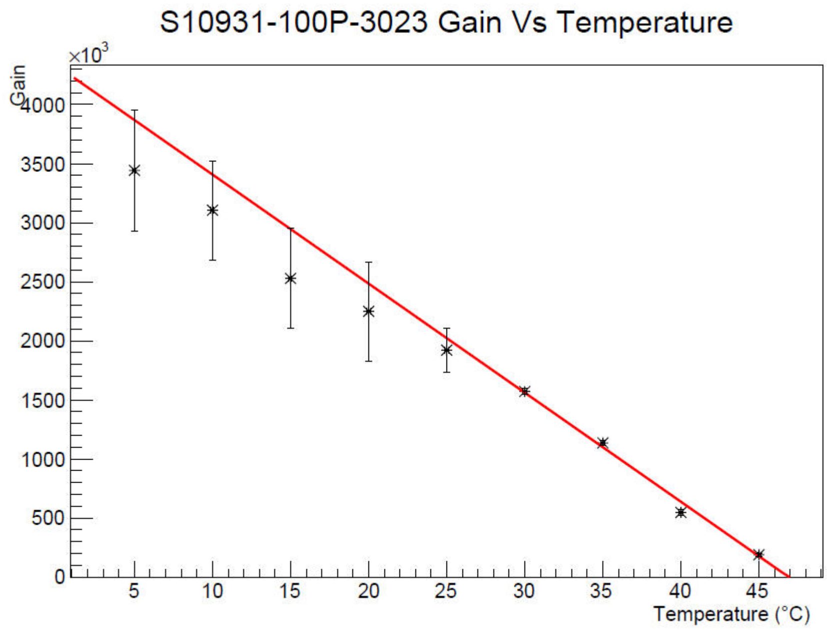

Figure 4.5: Gain of the SiPM S10931-100P as a function of temperature using a standard power supply

As expected, for a given bias voltage, the gain decreases linearly with increasing temperature.
Physically this phenomenon is explained by the fact that as the temperature increases, the Boltzmann distribution implies an increasing fraction of electrons in the conduction band and, thus, a decreasing resistivity of the semiconductor. Because the quenching resistor is made from polysilicon, Rq will decrease with increasing temperature. The junction capacitance, Cd, also varies with temperature. With zero bias, Cd $\propto \frac{1}{\sqrt{V_{BI}}}$, where V_{BI} is the p-n junction built-in voltage. Because V_{BI} decreases with temperature, Cd increases with temperature.
To solve the problem linked to temperature variations, which represents a serious limitation to the SiPM's performaces, and then to the VSiPMT's performances, we experienced a new electronic device manufactured by Hamamatsu which compensates the overvoltage at different temperatures.

4.1 C11204: a Power Supply Module for MPPCs

The C11204-01 high-voltage power supply is optimized for driving Hamamatsu multi-pixel photon counter (SiPM) series and can provide up to 90V output voltage. It looks like a 16 pin integrated circuit (size 19.4x17.0 mm) contained in a metal case (fig. 4.6)

Figure 4.6: Overview of the C11204 Hamamatsu power supply

The C11204-01 has built-in temperature compensation function: by connecting an external analog temperature sensor, the power supply adapts its output voltage to the envitronment temperature. In this way, the supplied SiPM can be operated optimumly even if an environment temperature is changed [38]. It also features a built-in the output voltage and current monitor; all functions can be controlled from a PC via serial interface. The main features of this device are summarized below:

- +5V supply required;
- Wide output voltage range: 50V to 90V;
- Low ripple noise: 0.1mVp-p typically;
- Good temperature stability: ±10 ppm/°C typically;
- High setting resolution: 1.8mV;
- Serial communication (UART);
- SiPM current monitor.

- Current absorption: 22 mA;

It also has many funtions such as the "Monitor", which provide output voltage +HV[V], output current Id[mA], and external temperature sensor value T[°C], the "ON/OFF switch" and the "Overcurrent protection", which stops the output of the high voltage when the current exceedes a 3mA threshold for more then four seconds.
But the most interesting feature is certainly the "Setup". This function can set the output voltage to any value by setting the reference voltage V_b[V], the reference temperature T_b[°C], the primary temperature coefficient $\frac{\Delta V}{\Delta T}$[mV/°C], and the secondly temperature coefficient $\frac{\Delta V}{\Delta T^2}$ [mV/°C^2]. In particular, by means of the latter two correction factors, a temperature compensation of the output voltage can be performed. More precisely, using the temperature T[°C] of the external temperature sensor, the output voltage +HV[V] is determined by the following formula:

$$+HV = \frac{\frac{\Delta V}{\Delta T^2} \cdot (T - T_b)^2 + \frac{\Delta V}{\Delta T} \cdot (T - T_b)}{1000} + V_b \tag{4.3}$$

Moreover, temperature coefficients can be set to four parameters: two for the high temperature (HT) side $(\frac{\Delta V}{\Delta T})_1$[mV/°C] and $(\frac{\Delta V}{\Delta T^2})_1$[mV/°C^2] (for temperatures higher than the reference temperature T_b) and two for the low temperature (LT) side $(\frac{\Delta V}{\Delta T})_2$[mV/°C] and $(\frac{\Delta V}{\Delta T^2})_2$[mV/°C^2] (for temperatures lower than the reference temperature T_b). So it is possible to set different correction factors for the output voltage above and below the reference temperature (fig. 4.7).

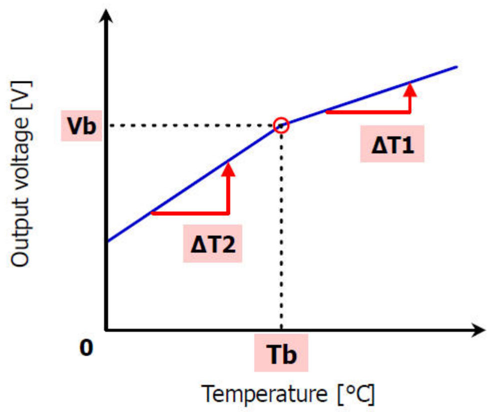

Figure 4.7: Output voltage versus temperature with different correction factors

4.1.1 Realization of the Circuit and Communication Specifications

Figure 4.8 shows the operating configuration of the chip by means of the schematic we have designed for the purpose:
Referring to the figure 4.8, the main components of the circuit are shown in green:

- C11204-01: is the power supply previously described;
- Temperature Sensor: is the Texas Instruments LM94021, a precision analog output CMOS integrated-circuit temperature sensor that operates at 1.5V supply voltage. While operating over the temperature range of -50°C to +150°C, the LM94021 delivers an output voltage that is inversely proportional to measured temperature with ± 1.5°C accuracy;
- Serial Output: is a RS-232 serial port which allows us to connect the device to a computer. RS-232 is an asynchronous serial protocol that defines the

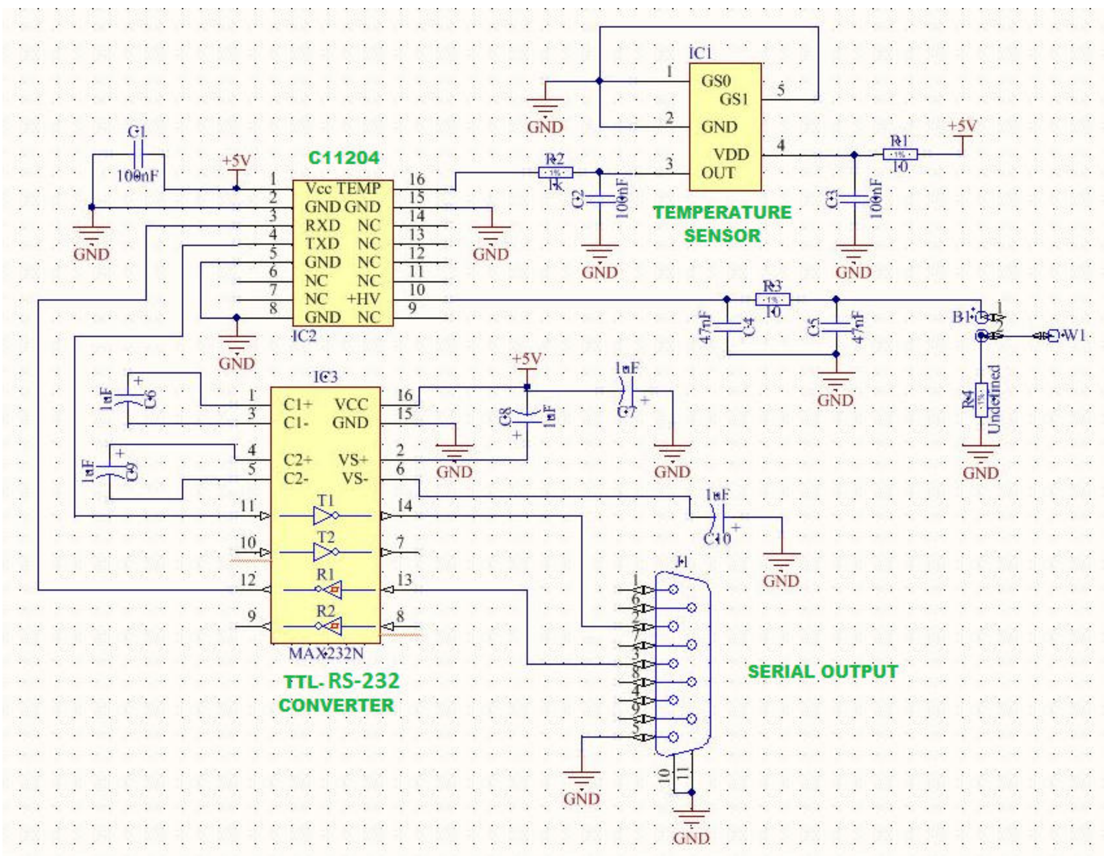

Figure 4.8: Schematic of the board designed for the C11204

voltage levels that correspond to logical one and logical zero levels for the data transmission and the control signal lines. Valid signals are either in the range of +3 to +15 volts or the range -3 to -15 volts with respect to the "Common Ground" (GND) pin, where the logical state LOW corresponds to the positive voltage values and the logical state HIGH corresponds to the negative voltage values.

- TTL-RS-232 Converter: is the ICL232, a dual RS-232 transmitter/receiver interface circuit that meets all ElA RS-232C and V.28 specifications. It requires a single +5V power supply, and features two onboard charge pump voltage converters which generate +10V and -10V supplies from the 5V supply. It was necessary to add this chip because the RX pin that acts as a receiver for the C112204-01 is a TTL port[4] whose signals are not directly compatible with the standard RS-232, whose control signals have opposite polarities.

After this first phase of schematic design of the circuit, we have designed the printed circuit board on which, then, we fitted the components by means of the PCB design software Altium. In figure 4.9 the PCB design and the final board are compared. The circuit has been assembled entirely at our home lab.

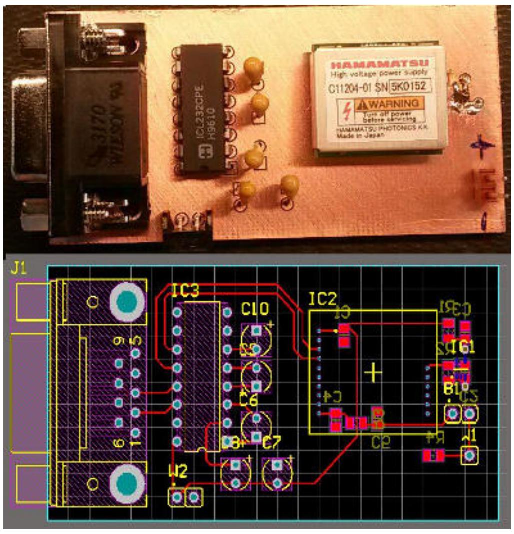

Figure 4.9: Final board versus PCB design

At this point the power supply was turned on and tested.

[4]Therefore, the voltage level that the pin interprets as a logical state HIGH corresponds to Vcc (5V in our case) and the voltage level that the pin interprets as the logical state LOW corresponds to 0V.

C11204-01 is communicated in UART communication protocol so, roughly speaking, it is provided with a universal asynchronous receiver/transmitter that takes bytes of data and transmits the individual bits in a sequential fashion by means of the pins RX and TX. At the destination, a second UART re-assembles the bits into complete bytes. Each UART contains a shift register, which is the fundamental method of conversion between serial and parallel forms. Regarding the receiver, all operations of the UART hardware are controlled by a clock signal which runs at a multiple of the data rate, typically 8 times the bit rate. The receiver tests the state of the incoming signal on each clock pulse, looking for the beginning of the start bit. If the apparent start bit lasts at least one-half of the bit time, it is valid and signals the start of a new character. If not, it is considered a spurious pulse and is ignored. After waiting a further bit time, the state of the line is again sampled and the resulting level clocked into a shift register. After the required number of bit periods for the character length (8 bits in this case) have elapsed, the contents of the shift register are made available (in parallel fashion) to the receiving system. The UART will set a flag indicating new data is available, and may also generate a processor interrupt to request that the host processor transfers the received data. Regarding the transmitter, operations are simpler as the timing does not have to be determined from the line state, nor is it bound to any fixed timing intervals.
Transmitting and receiving UARTs must be set for the same bit speed (or baud rate), character length, parity, and stop bits for proper operation; in particular UART communication specifications for C11204-01 are as follows:

- Baud Rate: 38400 bits per second;
- Data Bit: 8;
- Parity Bit: even;
- Stop Bit: 1;
- Flow Control: none;
- Data Order : LSB;

When C11204-01 receives the command from the host (our personal computer in this case), performs a process according to the command type (there always is a response to the command) and, by analyzing the contents of the command response, the exchange of data between the host and the power supply is performed. The command character code is ASCII[5], an example of sent and received command format is shown below (fig. 4.10), for more details about C11204-01 communication protocol refer to the device Command Reference [39].

[5]Acronym for American Standard Code for Information Interchange, is a character encoding standard

Example Send command)

	Command name						
STX	H	P	O	ETX	E	C	CR
0x02	0x48	0x50	0x4f	0x03	0x45	0x43	0x0D

Example Command response)

	Command			Status				Output voltage setting			
STX	h	p	o	0	0	0	9	B	D	8	7
0x02	0x68	0x70	0x6f	0x30	0x30	0x30	0x39	0x42	0x44	0x38	0x37

Output voltage monitor				Output current monitor				MPPC temperature monitor							
9	B	3	7	0	0	1	0	B	8	4	4	ETX	9	2	CR
0x39	0x42	0x33	0x37	0x30	0x30	0x31	0x30	0x42	0x38	0x34	0x34	0x03	0x39	0x32	0x0D

Figure 4.10: Example of sent and received commands, the characters that are not described in the figure are the header and delimiter of the string of characters (STX and CR), the end of the stecific command (ETX) and the error check (EC)

The commands were sent and received by means of the open source terminal Termite but, since each response that came from the power supply had to be translated from ASCII to Exadecimal and then from Exadecimal to dimensioned decimal numbers to have temperatures, voltages and currents, this way to control the device was found to be definitely cumbersome.
So we realized, thanks to the help of Dr. Riccardo de Asmundis, senior researcher at the INFN, a LabView interface (fig. 4.11) that would facilitate the communication. By means of this interface it is possible to easily set the four temperature compensation factors for HT and LT sides, the reference voltage, the reference temperature and the initial voltage level by directly entering their values in volts and degrees centigrade. The interface also provides a real time readout of the output voltage level, the current level and the temperature measured by the temperature sensor so we can check at any time the state of the system.
For this specific purpose the device drivers of C11204-01 were designed by Dr. Riccardo de Asmundis.

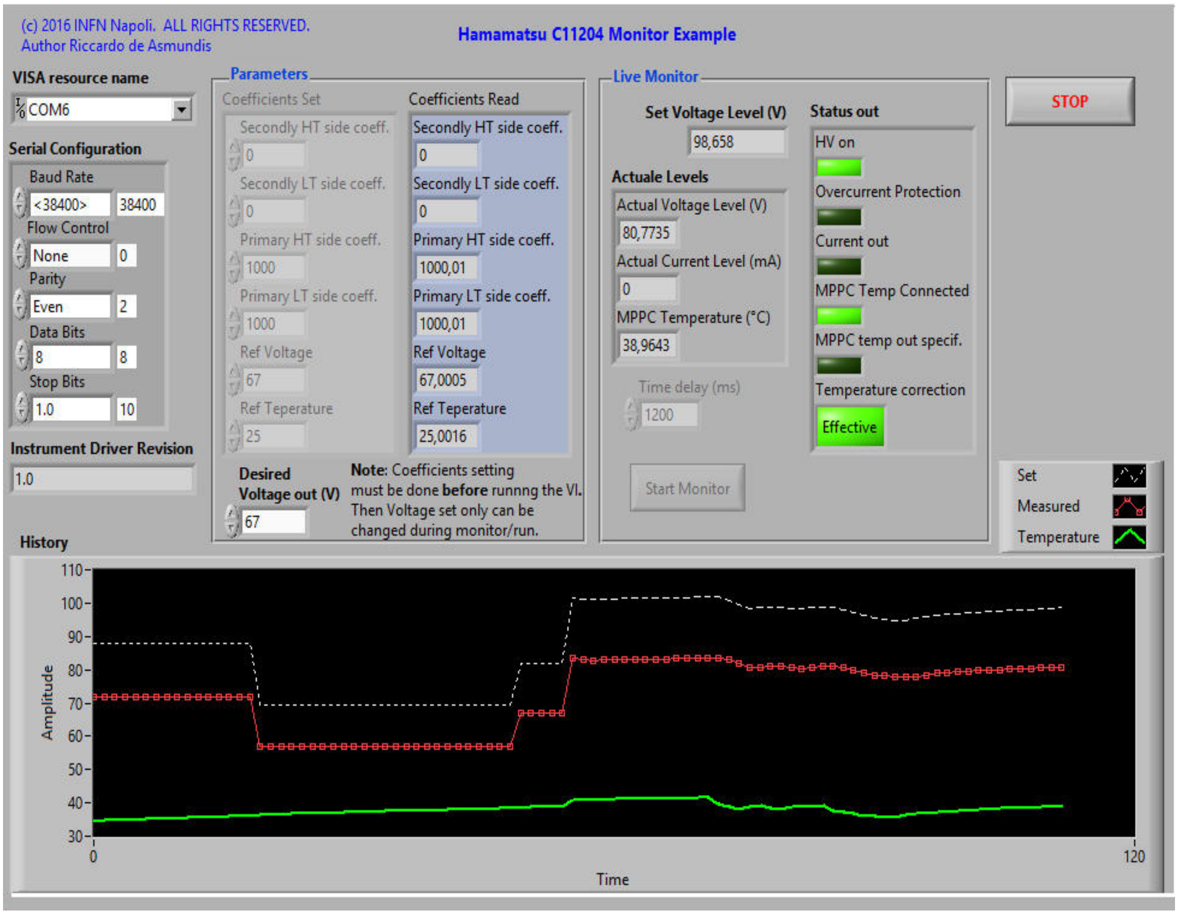

Figure 4.11: Screen of the LabVIEW control interface for C11204-01

4.1.2 C11204-01 Calibration and Test

To test the device we used the following experimental set-up, arranged as shown in figure 4.12:

- Angelantoni's environmental test chamber;
- Agilent power supply;
- The C11204-01 board;
- The LabVIEW control interface for C11204-01

We first verified that the temperature sensor was correctly calibrated. Then we set the environmental chamber so that its internal temperature varied from 45°C to 15°C in steps of 2°C, and for every step we read the temperature measured by the

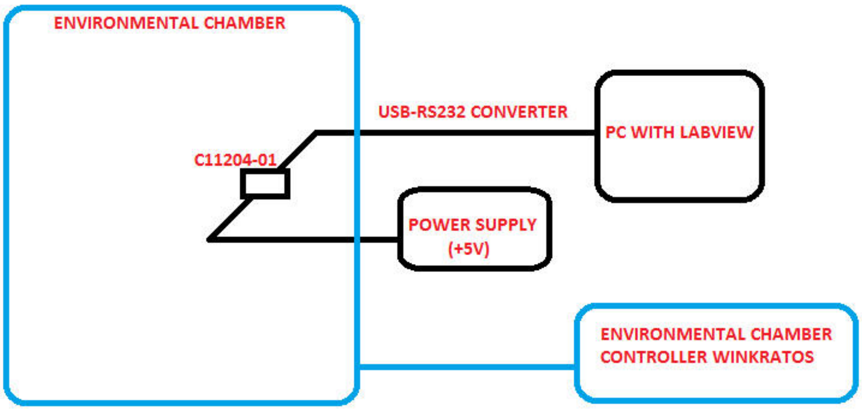

Figure 4.12: Experimental set-up for calibration and test of C11204-01

sensor. For all these measures the environmental humidity has been set to 17%. The results of this calibration are shown in the graph in figure 4.13, where X-axis shows temperatures set from time to time in the environmental chamber and Y-axis shows temperatures read by the sensor.

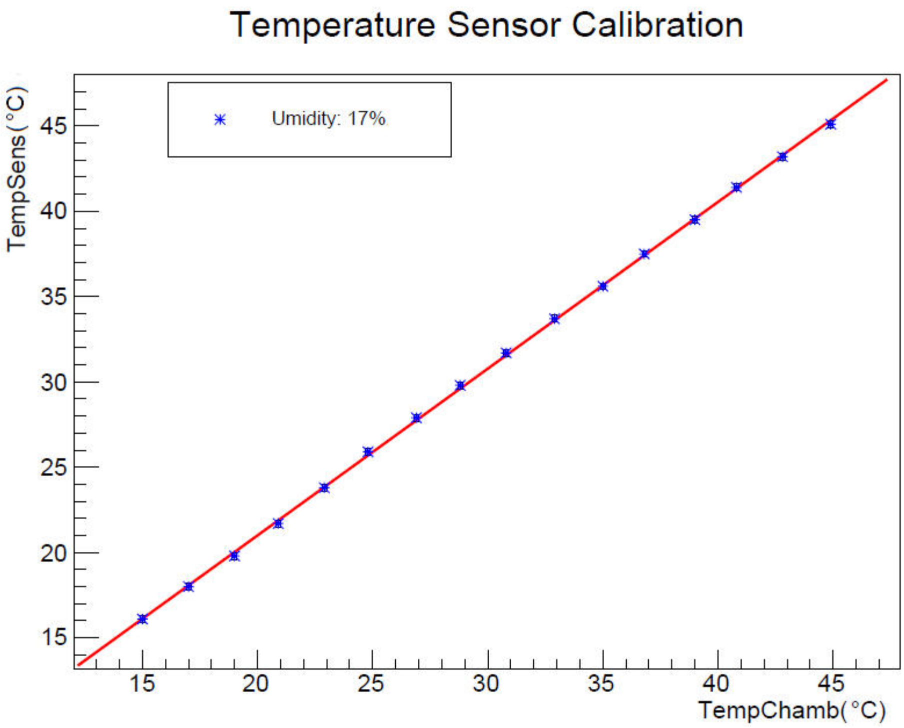

Figure 4.13: Trend curve of the temperature sensor calibration. $\chi^2 = 0.018$, slope = 1.0006 ± 0.0009

The linear trend of the temperatures read by the sensor with respect to those set in the environmental chamber shows that the sensor is well calibrated.
Finally, to verify that the power supply worked properly we set to 0 mV/°C^2 the value of the secondary temperature coefficient and to 1000 mV/°C the value of the primary temperature coefficient with 60V reference voltage and 25°C reference temperature. With this choice for the coefficients, the C11204-01 should modify the output power supply voltage of 1V for each 1°C temperature variation. So again we set the environmental chamber so that its internal temperature varied from 45°C to 15°C in steps of 2°C, and for every step we read the output voltage. For all these measures the environmental humidity has been set to 17%.
The results of this test are shown in the graph in figure 4.14, where X-axis shows temperatures set from time to time in the environmental chamber and Y-axis shows the output voltage.

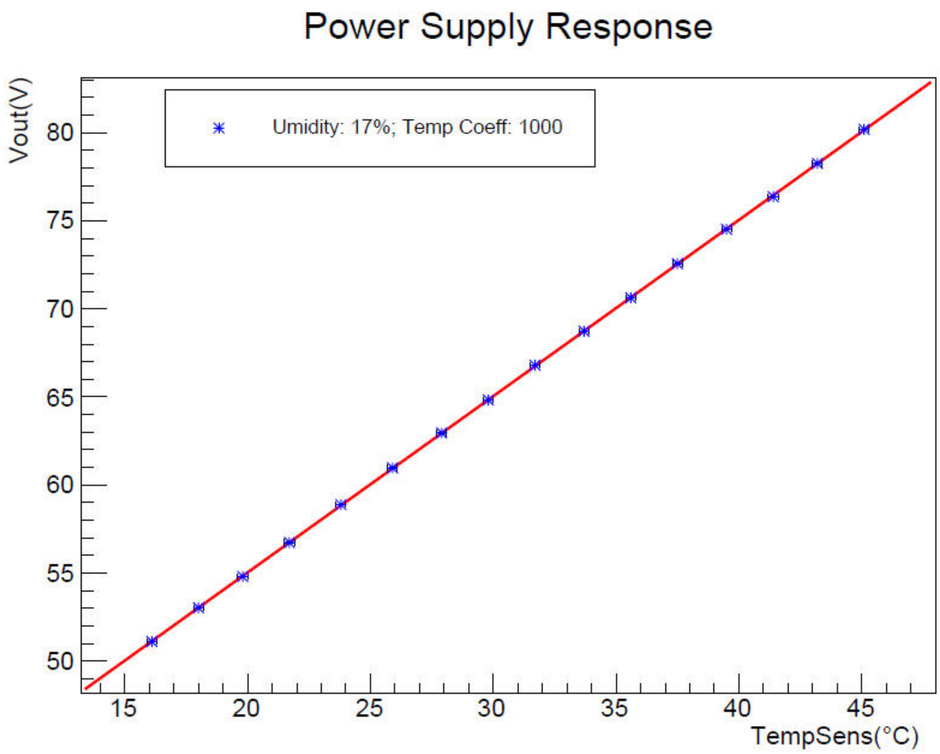

Figure 4.14: Trend curve of the power supply response. χ^2 = 0.31, slope = 0.977 ± 0.004

The linear trend of the output voltage with respect to temperature variations in the environmental chamber shows that the power supply is working as expected.

4.1.3 SiPM Characterization in Temperature With C11204-01

Found that the circuit was working properly, we performed a gain characterization in temperature for the SiPM S10931-100P using the C11204-01 as power supply (fig. 4.15).

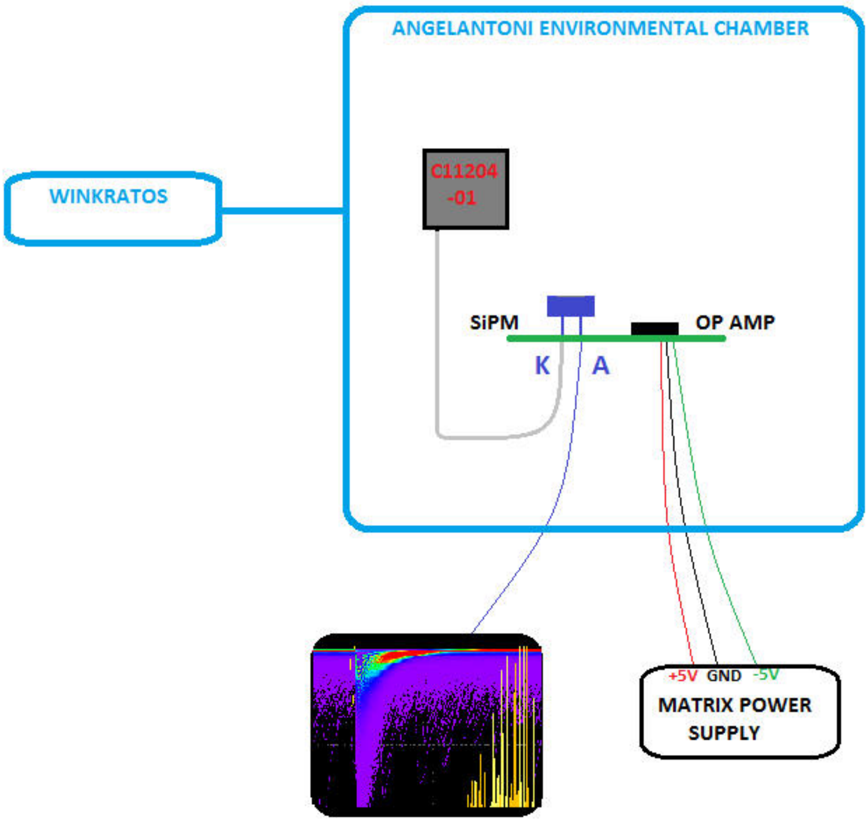

Figure 4.15: Schematic view of our experimental set-up

As seen in section 4.0.1, the breakdown voltage of the SiPM S10931-100P linearly increases of (55.5077 ± 0.5274) mV for every 1°C temperature increase. So we set the C11204-01 reference temperature to 25°, the reference voltage to 71.8V (that is the nominal V_{OP} at 25°C), the primary temperature coefficient $\frac{\Delta V}{\Delta T}$ to 56 mV/°C, and the secondly temperature coefficient $\frac{\Delta V}{\Delta T^2}$ to 0 mV/°C^2 to turn on the device's built-in temperature compensation function.
Then we performed measurements in the same way described in section 4.0.1 and the results are shown in the graph below (fig. 4.16).
From this graph it is evident that the gain in this case is always between M = 2 and M = 2.4, where the nominal gain of this device is M = 2.4. From the comparison

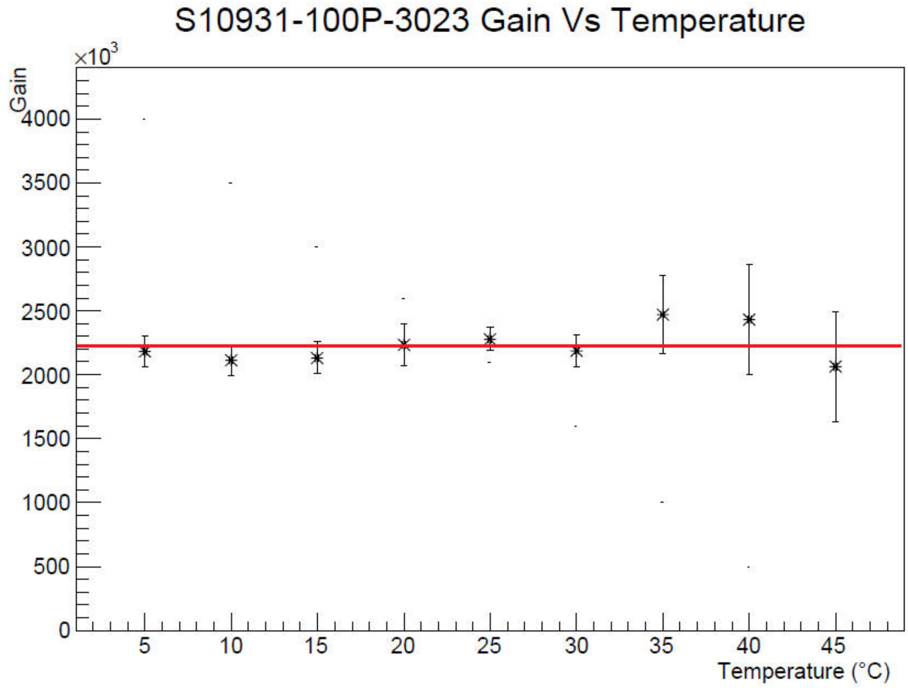

Figure 4.16: Gain of the SiPM S10931-100P as function of temperature using C11204-01 power supply

between the gain measurements as function of temperature variations, performed with a standard power supply and with the C11204-01, it is easy to see the clear improvement in SiPM's performances.
Indeed, with a standard power supply, as temperature increases, the gain decreases until the device turns off at 45°C; this is manifested by the gradual decrease in the amplitude of the SiPM's output signal, as we see in figure 4.17).

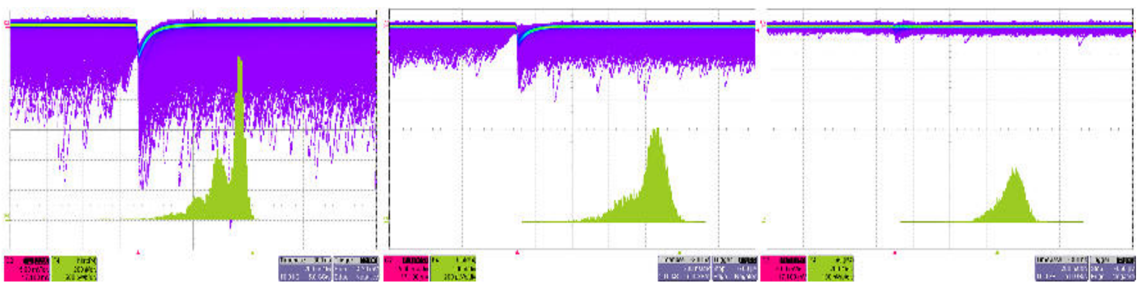

Figure 4.17: S10931-100P SiPM's output signals supplied with a standard power supply for (from left to right) 35°C, 40°C and 45°C environment temperatures. Notice that SiPM's signals have their amplitude significantly reduced as the environment temperature increases

While, with the C11204-01, as temperature increases the gain does not vary. Indeed, as evidenced by figure 4.18, the distance between the 1 p.e. peak and the 2 p.e. peak remains almost the same for all the waveforms.

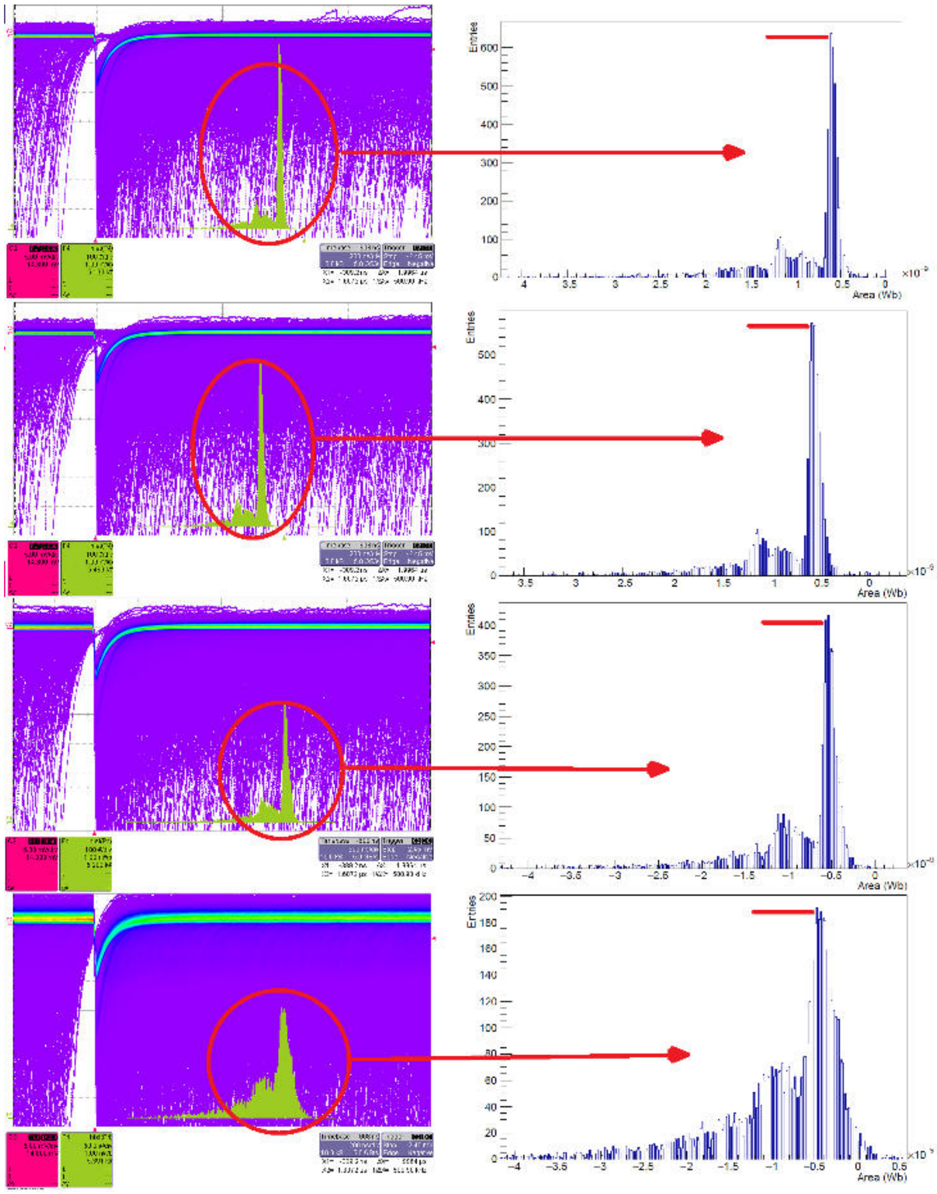

Figure 4.18: S10931-100P SiPM's output signals supplied with the C11204-01 power supply for (from high to low) 5°C, 10°C and 15°C and 20°C environment temperatures. Notice that SiPM's signals have their amplitude almost unvaried as the environment temperature increases

The only drawback of this device is that it can't clear the signal from thermal noise (the shrewd reader has certainly noticed the huge noise band that affects signals on the lower side of the figure 4.18). But it must be said that this analysis was performed on a very old generation SiPM with large pixels and high dark counts rate. The situation improves significantly if we use the latest generation SiPM.

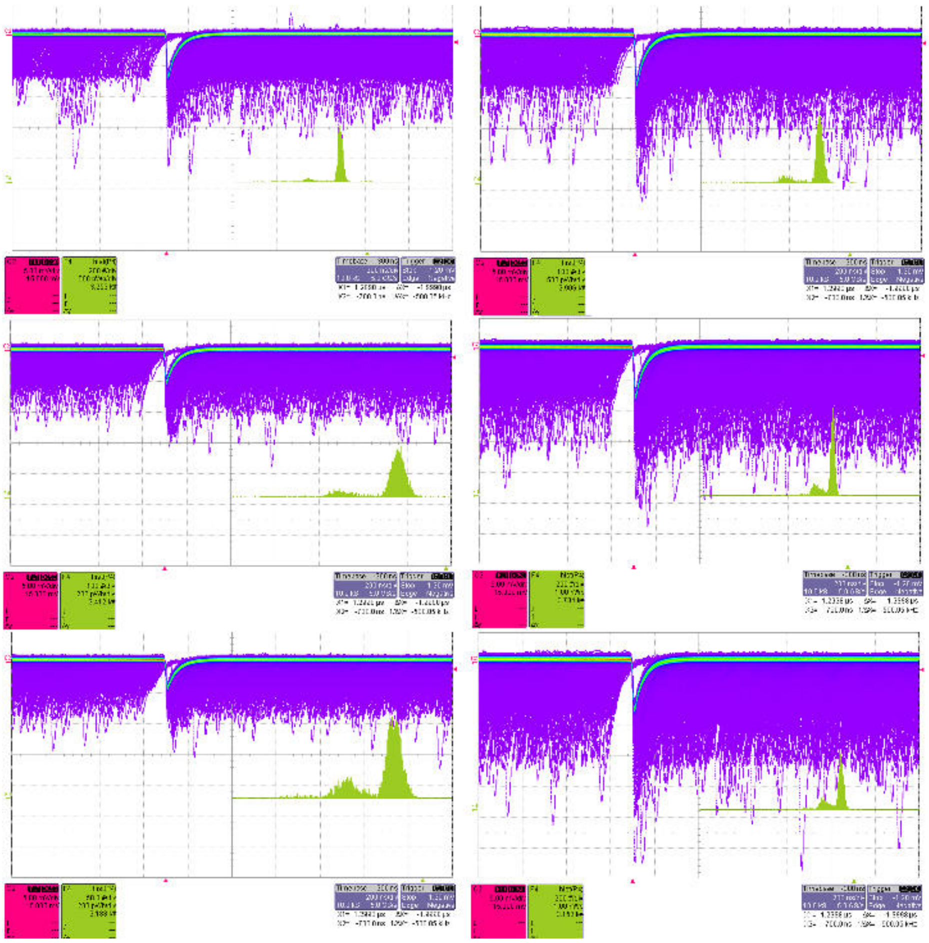

Figure 4.19: Comparison between S13360-4929 SiPM's output signals supplied with a standard power supply (left) and with the C11204-01 (right) for (from high to low) 35°C, 40°C and 45°C environment temperatures

Notice that the new generation SiPM's signals on the right have their amplitude not very significantly reduced as the environment temperature increases. This appens because of the small temperature coefficient and the better overall features of this device with respect to the old generation due to the improvement of material and wafer process thecnology. An interesting study could be performed in this direction.

Chapter 5

The Latest Usable VSiPMT Prototype

The VSiPMT project went on with a theoretical study of feasibility combined with Geant4-based simulations to find the range of the electrons in the SiPM. The first proof of feasibility [41] arrived in 2012, when the response of a special SiPM, as electron multiplier, was tested with an electron beam extracted at the TTT3 accelerator available in the Physics Department of the University of Naples.
The results obtained convinced Hamamtsu Photonics, a world leader company in photodetector manufacturing, to realize for professor Barbarino's research group two VSiPMT prototypes to start to explore the potentialities of the device: EB-MPPC050 (ZJ5025) and EB-MPPC100 (ZJ4991).
The characterization of these first two prototypes of VSiPMT put up really encouraging results [42]. The devices exhibit outstanding properties and performances beyond expectations, neverthless, they were no usable because of the small size (3 mm diameter photocathode) and the reduced dynamic range; these problems are due to the fact that these two prototypes were just testing devices, manufactured to verify the properties found during the feasibility tests. Anyway Hamamatsu improved these two features and assembled the device: **prototype EB-MPPC100 (XE2597) 1 INCH**, the first really usable VSiPMT prototype. A picture of it is shown in figure 5.1.
The absence of the dynode chain entails a visible consequence: the device is small.

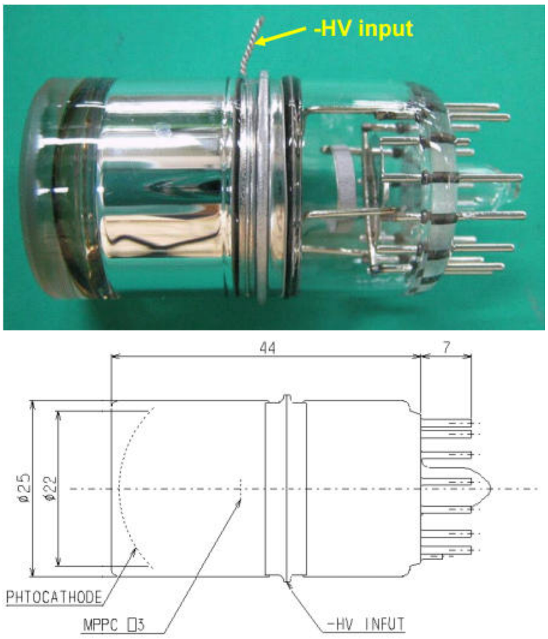

Figure 5.1: Picture of the VSiPMT prototype (side view) together with the dimensional outline of the device in mm

This prototype was made from a standard PMT, whereby all connections available (which originally served as connections for the dynodes) only two are used effectively: the one for the SiPM supply and the one for the readout signal (fig. 5.2).

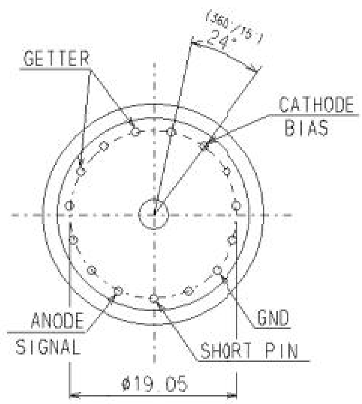

Figure 5.2: Detail of the connections

Under a Borosilicate Glass round window (Φ = 25 mm diameter) is deposited a circular Bialkali photocathode (22 mm diameter), where photo-electron conversion occurs. The Bialkali photocathode offers a good quantum efficiency optimized for the detection of Near Ultraviolet radiations (NUV 300÷400 nm wavelength). Indeed the photocathode spectral response (shown in figure 5.3) have the QE peak value (about 15%) for an incident wavelength $\lambda = 350$ nm. In our case (407 nm wavelenght) QE $\sim$ 12%.

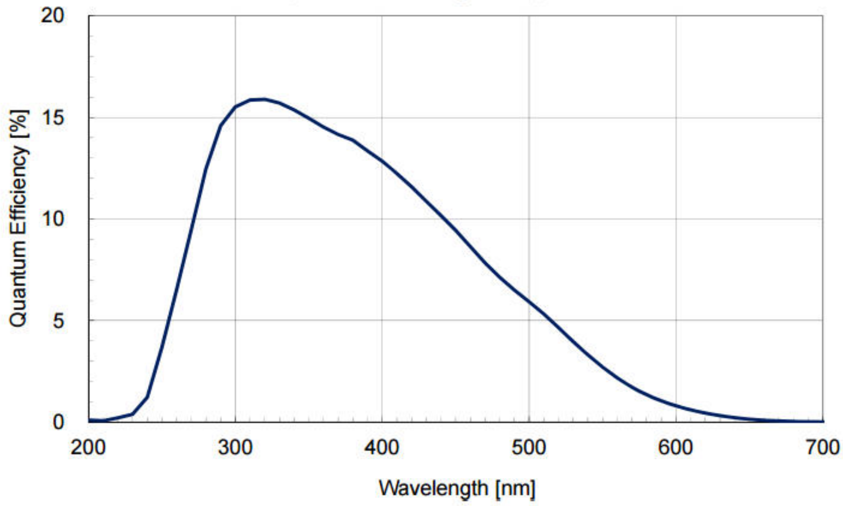

Figure 5.3: Photocathode spectral response

A single stage focusing system is present to drive the photoelectrons on the SiEM. It is composed by a focusing ring kept at the same potential with respect to the HV applied to the photocathode. The system is accomodated into a cylindrical glass case of 44 mm length.
In this prototype a special windowless SiPM is mounted, the absence of the protective entrance window eases the entrance of the photoelectrons into the Silicon. Moreover, the SiPM used is realized in a p^+nn^+ configuration for EDE optimization, as explained in the first part of this thesis (SiEM).
Characteristics and recommended work conditions are summrized below:

- SiEM area: 3 x 3 mm^2;
- number of pixels: 900 of size 100 x 100 μm^2;
- fill factor: 78%;
- optimized configuration: p^+nn^+;
- SiEM operation voltage: +71.5 V;
- photocathode power supply: -1.9 kV.

5.1 VSiPMT Characterization

The prototype underwent many tests summarized here below and discussed in the following sections, in order to achieve a full characterization of:

- signal quality stability and photon counting capability;
- detection efficiency;
- gain;
- photocathode omogeneity;
- Transit Time Spread;
- dark counts;
- linearity and dynamic range.

The experimental set up prepared for these measures is the same as described previously (section 3.2), with the difference that it was necessary to mount a suitable support for the VSiPMT connections on the board (fig. 5.4), and we chose a feedback resistor for the operational amplifier equal to 3 kΩ.

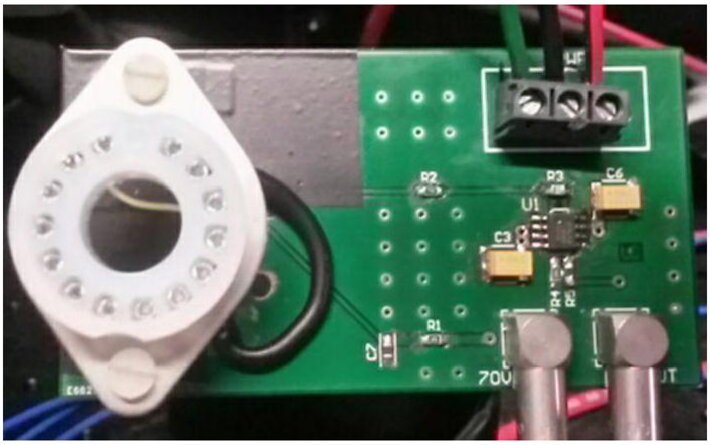

Figure 5.4: Picture of the amplification board for the VSiPMT prototype, the white circle is the special support for the VSiPMT connections

5.2 Signal Properties and Photon Counting Capability

First of all the VSiPMT signal properties have been studied. A typical output waveform of the device is shown in figure 5.5. As clear from the oscilloscope screenshot, the pulse duration is $\sim$ 100 ns with a rise time of $\sim$ 15 ns and a fall time of $\sim$ 90 ns. These vaues take account of the front end electronics delays even and not only of the device timing.

One of reasons of outmost importance that led to the VSiPMT design is the expectation of a remarkable single photon resolution. With this purpose, a study of the photon counting capabilities of the device has been done by illuminating the photocathode with a low intensity laser beam.

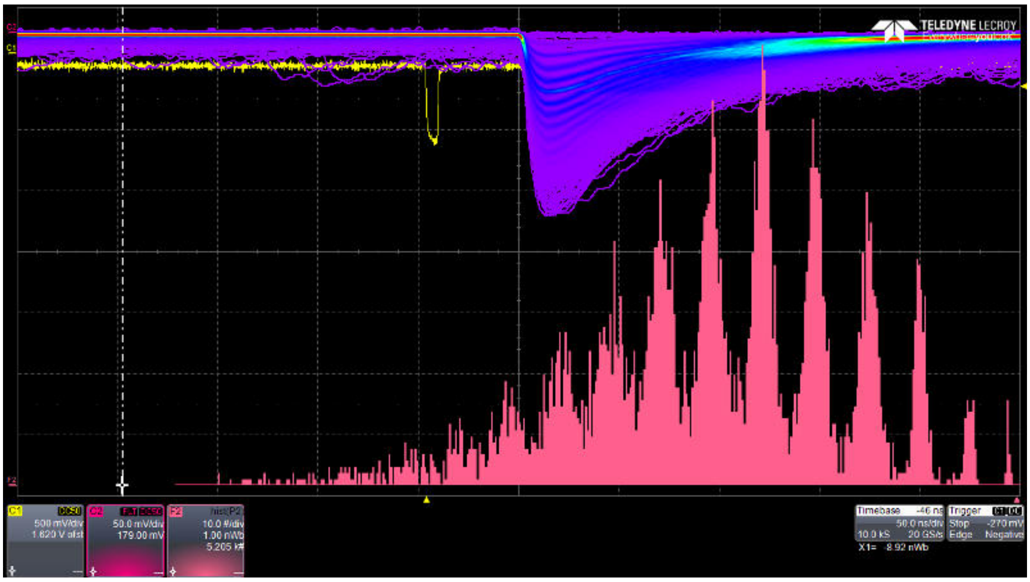

Figure 5.5: Printscreen of the VSiPMT output signal in response to 90 incident photons and the corresponding charge histogram

Figure 5.5 shows the output waveforms of the device and the corresponding charge spectrum. For this measurement the synchronization signal of the laser source has been used as trigger in the oscilloscope-based acquisition system and the responses for multiple triggers have been overlayed in an infinite persistency.

Looking at the oscilloscope printscreen it is undeniable that waveforms corresponding to different numbers of fired pixels are very well separated, the same goes for the area spectrum. This is a demonstration of the excellent photon counting capabilities of the VSiPMT prototype. In figure 5.5, as well as in the related spectrum it is possible to count separately the number of simultaneously fired pixels going from a single pixel up to twelve, a performance simply unreachable by standard PMTs (where photon counting is impossible as evident in figure 5.6) and even by the recently developed HPDs (where the single peak resolution is not so good because of fluctuations in photon counting, due to the fact that HPDs use junctions which work in proportional regime as electron detectors) .

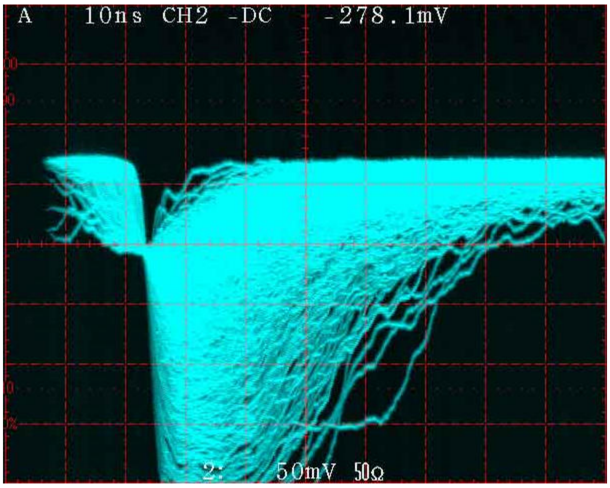

Figure 5.6: Printscreen of the output signal of the Photo multiplier tube TS-80000 series

5.3 Gain

In a VSiPMT the gain is obtained by the electrons crossing the Geiger region of the SiEM. Thus, a standard current signal is given for each fired cell. Therefore, for the prototype under test the gain coincides with the gain of the SiEM used.
According to the above description, the gain of the SiEM can be defined as the fraction between the charge of the pulse generated from each pixel during the breakdown process and the charge of the electron. The charge of a single fired pixel can be calculated as the difference between all the possible couples of adjacent peaks in the charge spectrum shown in figure 5.7.
A measure of the SiEM gain as a function of the applied bias voltage in the range [70.8, 71.5] V has been performed, keeping HV = -1.9 kV. The resulting curve (see fig. 5.8) exhibits a very linear trend, with values ranging between [1.3 x 10^6; 2.6 x 10^6], in fairly good agreement with expectations. The same measure has been performed keeping HV off, since the results where the same as if the HV was on they are not reported here.

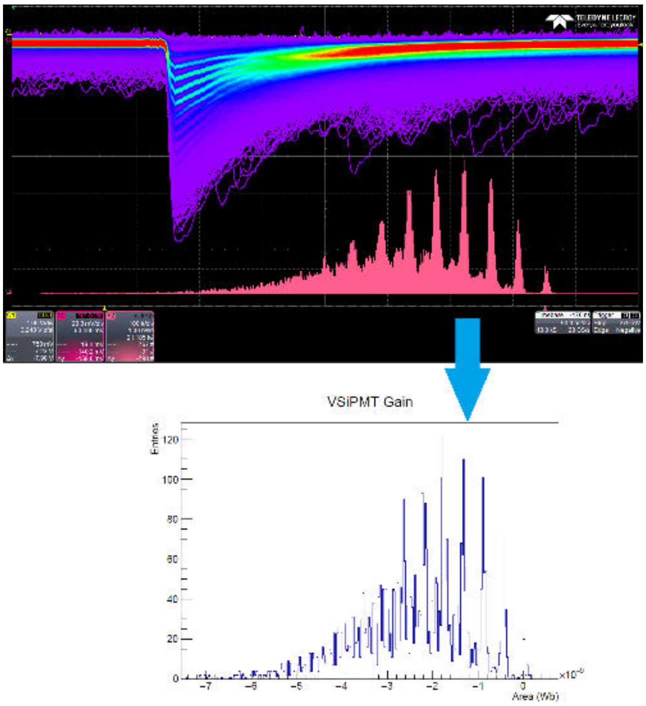

Figure 5.7: VSiPMT's output signal and its spectrum of charge (printscreen fro Teledyne Lecroy SDA 760Zi 6 GHz Serial data Analyzer). Notice that waveforms corresponding to different numbers of fired pixels (and so the peaks in the spectrum) are extremely well separated

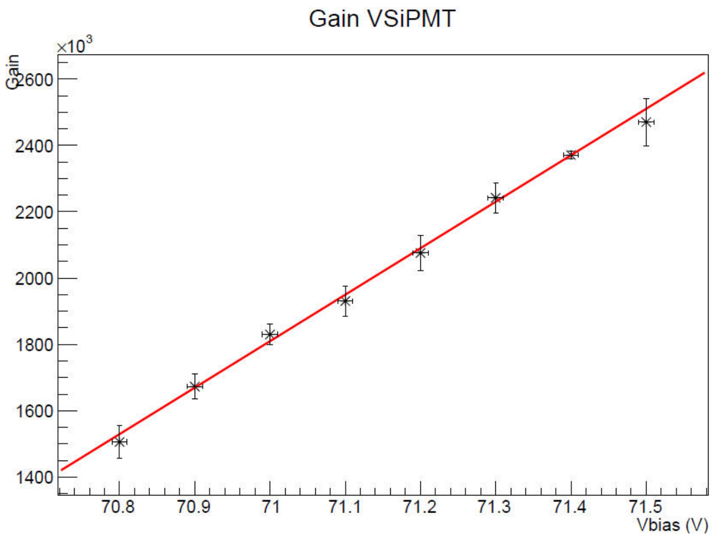

Figure 5.8: Graph of gain versus V$_{bias}$ for the VSiPMT

5.4 Noise

Three are the sources of noise in a VSiPMT: afterpulses, crosstalk and dark rate, widely explained in section 3.2.2.
In the first case, the combination of the vacuum tube and the SiEM gives rise to a double contribution: vacuum related afterpulses and SiEM afterpulses.
The former are produced by the ionization of residual gases left in the tube after evacuation or degased materials present in the vacuum silicon photomultiplier tube after the evacuation. In this case the arrival time of the afterpulse depends on the ion mass and on the HV applied between the photocathode and the SiEM, while the afterpulse amplitude depends only on the HV. The second class of afterpulses is intrinsically related to the SiEM technology [43]. In this case, secondary pulses are generated by charges carriers that are temporarily trapped by some impurities inside the crystal lattice and then released again after some delay which can last from few nanoseconds up to several microseconds.
The main noise source in a VSiPMT is represented by dark pulses and crosstalk. Two contributions can be taken into account: thermal electrons emitted at the photocathode and intrinsic SiEM noise. The latters represent the main contribution, since they have a typical rate ranging between few tens and some hundreds of kcps per mm^2 of active surface, depending on the applied bias voltage. In addition to the strong dependence on the bias voltage, SiPMs dark rate relies heavily on the pe threshold. For this reason, measurements of the dark count rate at different bias voltage and different thresholds have been done.
The photocathode voltage has been set to -1.9 kV and the bias voltage to different values: from 71.0 V to 71.6 V in 0.1 V steps. For each of those values has been measured the number of events with peak amplitude above 0.5, 1.5 and 2.5 photoelectrons threshold. The results are shown in figure 5.9 and are in excellent agreement with the expected dark count rate of the SiEM alone. In order to confirm the assumption that the main source of dark noise is the SiEM itself, the measure has been repeated in the same experimental conditions but with no high voltage applied to the photocathode. The results were absolutely unvaried; in the table below are collected the values of the dark rates with their errors for the three tresholds at $V_{bias} = V_{OP} = 71.5$ V and keeping HV on.

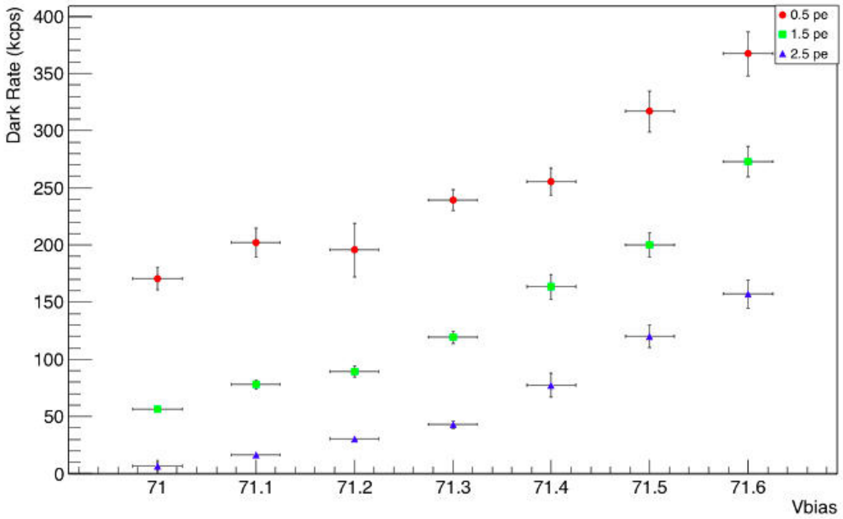

Figure 5.9: Dark noise rate as a function of the SiEM overvoltage for the VSiPMT

$0.5pe$	treshold	$(316, 907 \pm 0.564)$ kcps
$1.5pe$	treshold	(200.048 ± 0.215) kcps
$2.5pe$	treshold	(120.211 ± 0.176) kcps

This dark rate seem to be high, the reason lies in the choice of SiEM mounted in the VSiPMT. In the previous chapters several generations of SiPMs have been confronted, and we saw that the latest devices differ from the older ones for their superior performances in terms of dark rate. The core device of this VSiPMT prototype clearly belongs to an old generation series (section 3.1.3).
However, in a realistic experiment unlikely we would have to disclose a single photon. So we can choose a higher treshold for our trigger (4 or 5 p.e.) and cut away this noise, so we foresee an optimistic future in this direction.

5.5 Detection Efficiency: Operating Point

The Photon Detection Effciency (PDE or ϵ_{tot}) of the VSiPMT can be defined as the product of three factors:

$$\epsilon_{tot} = \epsilon_{PC} \cdot \epsilon_{geom} \cdot \epsilon_{trigger} \tag{5.1}$$

Where ϵ_{PC} is the photocathode's quantum efficiency, ϵ_{geom} is the geometrical efficiency which takes account of the focusing and the SiEM fill factor and $\epsilon_{trigger}$

is the trigger efficiency which takes account of the probability an electron have to trigger an avalanche[1]. The phenomenology correlated to this latter parameter is well explained by means of figure 5.10.

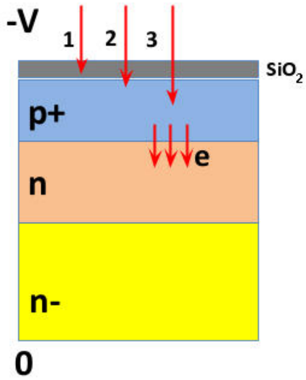

Figure 5.10: Schematic view of photoelectrons coming from the photocathode and impinging on the p-over-n SiEM inside the VSiPMT

Referring to the figure, photon n° 1 have no energy enough to enter in the p^+ region, indeed it stops into the SiO_2 insulating layer; photon n° 2 have enough energy to overcome the SiO_2 layer and enter in the p^+ region, but its drift is too short, the number of pairs produced is to few and the probability that one of them reach the depletion region is low because of the recombination; photon n° 3 has energy enough to enter in the depletion region and trigger the Geiger avalanche.
The range of photoelectrons (that depends on the photoelectron energy after the HV acceleration) inside the SiEM must to be enough to overcome the passivation layer of SiO_2 and a part of p region in such a way that a sufficient number of electron-hole pairs are produced.
At present we do not know the thickness of the passivation layer SiO^2 in front of the SiEM inside the prototype EB-MPPC100 (XE2597) 1 INCH, but we know that the SiEM's fill factor is ϵ_{geom} = 78% and the photocathode efficiency is ϵ_{PC} = 12%, so by measuring ϵ_{tot} (PDE) we can obtain $\epsilon_{trigger}$.
The PDE with respect to the high voltage supplied to the photocathode has been measured as follow.
The device has been illuminated with few photons per pulse ($\sim$ 70) by using an optical fibre, during the test the laser beam intensity has been monitored by the power meter. The PDE is experimentally defined as:

$$PDE = \frac{N_{pe}}{N_{ph}} \tag{5.2}$$

[1]In first approximation we can say that $\epsilon_{geom} \cdot \epsilon_{trigger}$ is equal to the EDE defined in section 2.4

where N_{pe} is the number of fired cells and N_{ph} is the number of photons per laser pulse hitting the photocathode. Once we set the light conditions, we tested the PDE as a function of HV, by varying the photocathode power supply in steps of 100 volts. The results of this test are showed in figure 5.11, where is evident that the maximum efficiency available is PDE = 2.4%.

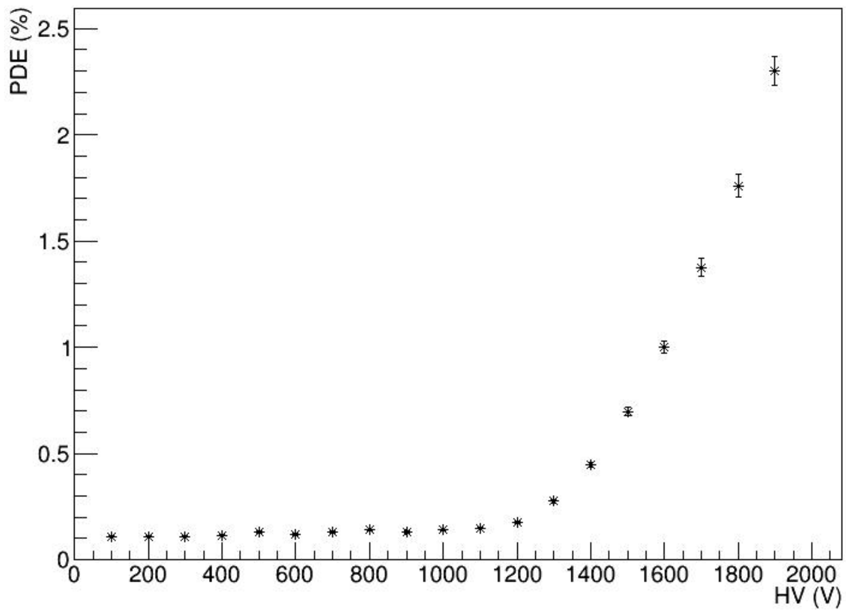

Figure 5.11: Results of the photon detection efficiency test in function of the HV

From this measure we expected that, for a certain HV level, the PDE of the device had to reach a plateau (a similar analysis has been performed on an old version of the VSiPMT prototype, a detailed description of this measurement can be found in Appendix B)
In such a device, the plateau region is linked to the energy threshold of the photoelectrons. Therefore, the high voltage is required only to drive photoelectrons to the SiEM surface and to give them the right energy. This is one of the biggest differences and advantages of the VSiPMT with respect to other photodetector categories. This behaviour comes from the different gain concept applied in the VSiPMT where, as already exstensively illustrated, the high gain is provided by the geiger avalanche occurring in the SiEM and therefore the PDE doesn't depend on the photoelectrons energy once they are over the threshold. This means that once the device is operated in the plateu region further stabilizations due to high voltage fluctuations are not necessary.
On the contrary, both for PMTs and HPDs the gain strongly depends on the photoelectron energy. For those devices the higher is the voltage supplied to the

photocathode and the higher is the gain, implying the necessity of frequent calibrations.
Unfortunately in this prototype the total efficiency does not reach the plateau (fig. 5.11). This means that the $\epsilon_{trigger} < 1$, indeed it results to be $\epsilon_{trigger} = 0.21$ from 5.1. If the trigger efficiency were 1, the total efficiency should be:

$$\epsilon_{tot} = \epsilon_{PC} \cdot \epsilon_{geom} \cdot \epsilon_{trigger} = 0.12 \cdot 0.78 \cdot 1 = 0.093 \tag{5.3}$$

The reason why the total efficiency does not reach the plateau is a manufacturing defect (fig. 5.12). The HV power supply connection is too close to the ground plate on which the SiEM lays. So it is strictly recommended to not exceed -2kV HV power supply or sparkles may occur which could break the device.

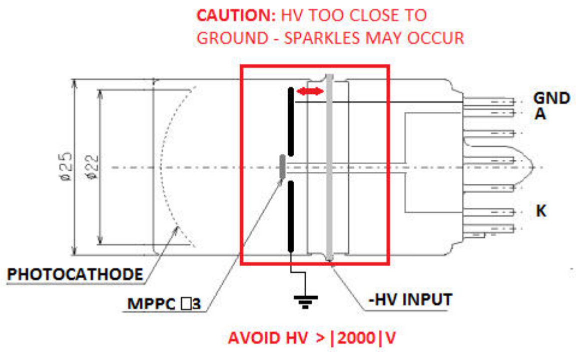

Figure 5.12: Schematic view of the VSiPMT internal structure

But this is as problem which very easily can be solved during the device assembly and, for sure, it will not occur in the next prototype.

5.6 Photocatode Scan X-Y

An x-y scan of the photocathode has been done with the HV on and off, to probe the uniformity on the entire sensitive surface by estimating the local PDE. For this measurement a micrometric x-y motorized pantograph has been used.

5.6.1 HV Off

As evident in figure 5.13, the scan performed with HV off shows a weak over-efficiency effect in correspondence of the SiEM, due to the photocathode transparency with respect to photons in that point. Anyway this is a negligible effect in all usual photodetection applications because the area affected by the phenomenon (9mm^2) is small with respect to the total photocathode area (2cm^2).

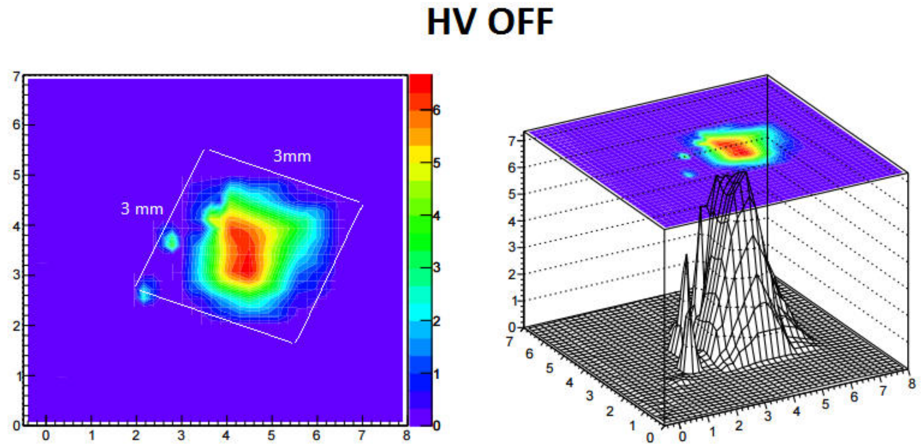

Figure 5.13: Results of the x-y scan of the photocathode of the prototype with HV off. The white square is a projection of 3x3 SiEM on the photocathode obtained by direct photon detection

To be more quantitative, we have a 4% over-efficiency (calculated by means of a weighted average of the colored areas in figure 5.13 left) in 1.7% of total 1 inch photocathode area. In 4% of cases at the center of the photocathode, in corrispondence of the SiEM, the photon is also transmitted and directly detected by the SiEM, without undergoing the photoelectric effect.
Assuming that a final device could have a 35% of total PDE (45% photocathode, 78% fill factor, 100% trigger efficiency), this over-efficiency in correspondence of the SiEM is considerable as a fluctuation[2] (fig. 5.14).

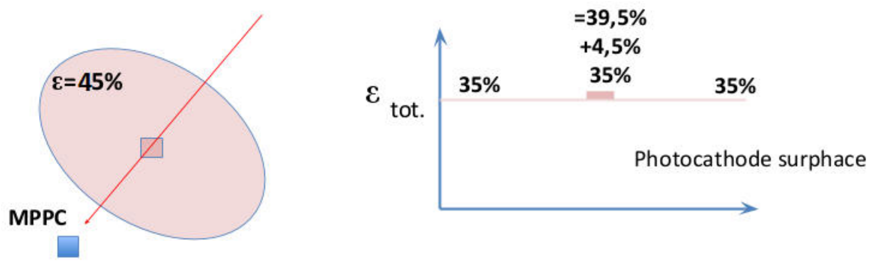

Figure 5.14: Photodetection efficiency in the hypothetical conditions 45% photocathode efficiency (instead of 12%) 78% fill factor and 100% trigger efficiency (instead of 21%)

Anyway, being this an over-efficiency and not an under-efficiency defect, it is not so much undesiderable.

[2]In the central region 3x3 mm^2 the efficiency will be 39,5%

5.6.2 HV On

Then we performed a x-y scan with HV on. Figure 5.15 shows xy efficiency scan of a quarter of photocathode when the previous weak 4% effect is subtracted.

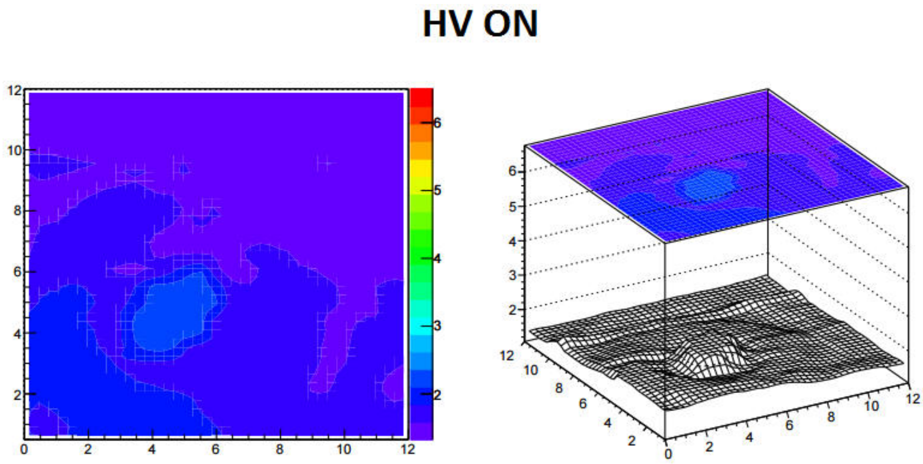

Figure 5.15: Results of the x-y scan of the photocathode of the prototype with HV on

The photocathode results to be homogeneous within 90% but its efficiency is very low over the 1 inch photocatode surface (as we expected):

$$\epsilon_{tot} \sim 2\% \tag{5.4}$$

This deficit of efficiency (it should be 9.3% and not 2%) is most likely due to the defect mentioned in section 5.5, so the majority of photoelectrons can't reach the minimum energy to enter into the silicon bulk and, consequently, to produce a signal.

5.7 Transit Time Spread

The interval between the arrival of a photon at the photocathode and that of the corresponding SiEM's 1 p.e. output current pulse is called the **transit time**. Transit-time fluctuations are observed when photons strike different parts of the photocathode (fig. 5.16). The **transit-time spread (TTS)** (also called jitter, or time resolution) is defined as the FWHM of the probability distribution of these fluctuations. It would be practically proportional to $\frac{1}{\sqrt{n_p}}$ and to $\frac{1}{\sqrt{HV}}$, where n_p is the number of photoelectron per pulse and HV is the cathode power supply, if the photons's trajectories were the same. In our case the electrons generated by photoelectric effect on the phtocathode are focused on the active surface of the SiEM following different paths.

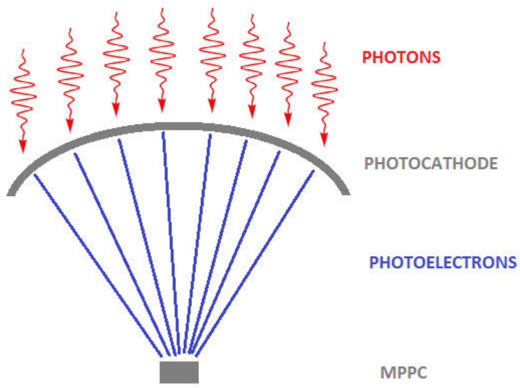

Figure 5.16: Schematic view of photons incident on the photocathode's surface

The timing plays a crucial role in all those experiments and techniques where particle direction has to be reconstructed with high accuracy, like water Cherenkov neutrino telescopes for astroparticle physics and PET for medical equipments. From this point of view, a short TTS is mandatory to disentangle different events and to reconstruct the particle direction with a good resolution.
In all the vacuum photodetectors (PMTs, HPDs, VSiPMTs) the main contribution to TTS is given by the spread in electron path length. Neverthless, in VSiPMT (and HPDs too) the TTS is expected to be systematically lower with respect to that measured in a standard PMTs, since the former lacks the contribution provided by the spread generated in the dynode chain. In a VSiPMT, indeed, the electron multiplication obtained bymeans of a breakdown is a very fast process with negligible time spread.
The TTS measurement has been performed by using the experimental setup shown in fig. 5.17, in extremely low ligh conditions (we put the laser at low power and far from the photocathode, so for every pulse we had an average of 1 photon hitting a casual point on the photocathode surface).
The synch pulse of the laser is used as trigger, while the output signal of the VSiPMT is fed as stop signal via a discriminator.
By means of a specific function of our oscilloscope called "Dtime@level", we have been able to measure the time interval elapsed between the single electron output signals and the laser pulses. We acquired such a data for a almost 200 x 10^3 measures run, this information have been expressed in the form of a histogram (fig. 5.18).

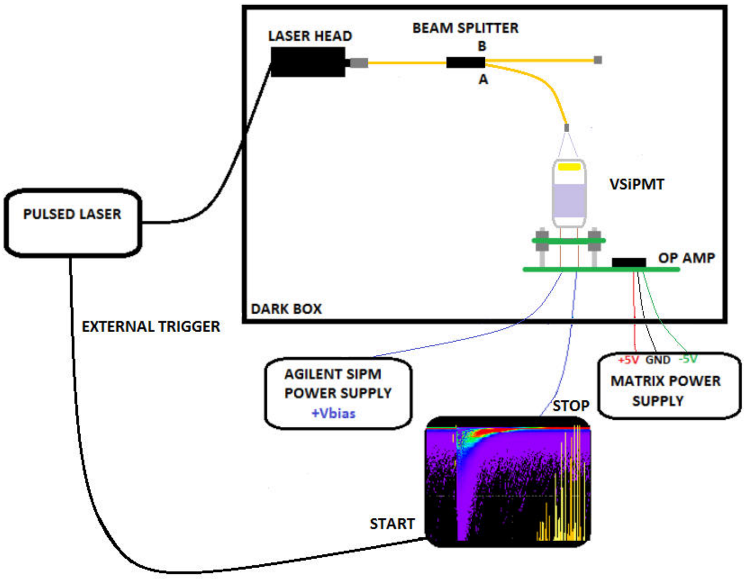

Figure 5.17: Experimental setup scheme for the TTS measurement

This histogram have a gaussian shape and its full width at half maximum is the Transit Time Spread we were looking for. A preliminary evaluation of the Transit Time Spread made by our oscilloscope provides a value equal to 2.5 ns (lower side of figure 5.18).

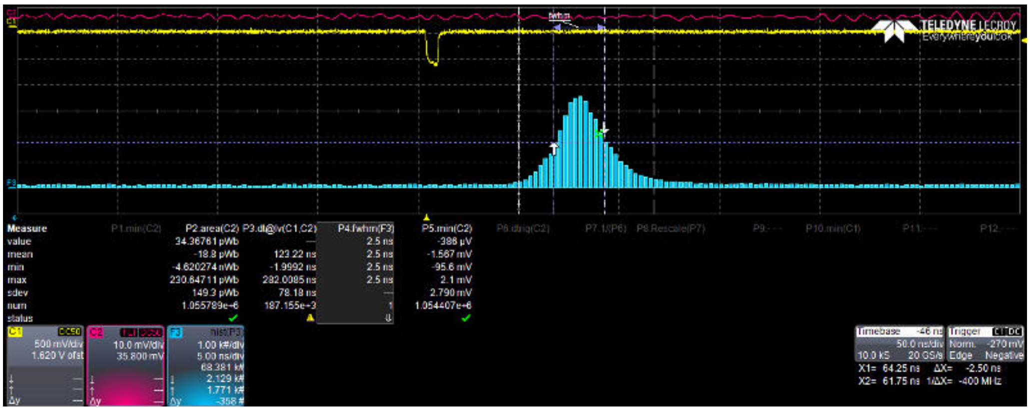

Figure 5.18: Printscreen of the VSiPMT output signal and Dtime@level acquisition. The yellow squarewave is the trigger signal from the oscilloscope. The red waveform is the VSiPMT spe signal. The histogram is the distribution of the arrival time of the VSiPMT signal with respect to the laser trigger.

With a more accurate analysis made by means of the data analysis tool Root (fig. 5.19), that provides the values of the mean = (6.205 x 10^{-8}) s and the standard deviation = (1.093 x 10^{-9}) s of the time intervals gaussian distribution, we calculated this parameter as follows:

$$TTS = FWHM^{3} = 2 \cdot \sqrt{2 \cdot ln2} \cdot \sigma \sim 2.355 \cdot \sigma = (2.576 \pm 0.008)ns. \tag{5.5}$$

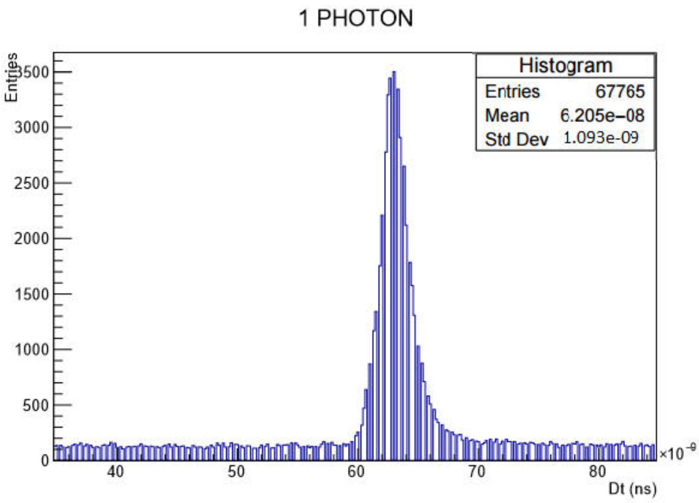

Figure 5.19: Gaussian distribution of the time intervals between the single electron signals and the laser pulses made by means of the data analysis tool Root for 1 photon per pulse

Then we performed the same measure with a higher number of photons (100) and we obtained (fig. 5.20):

$$TTS = FWHM = 2 \cdot \sqrt{2 \cdot ln2} \cdot \sigma \sim 2.355 \cdot \sigma = (1.653 \pm 0.001)ns. \tag{5.6}$$

Is evident that this TTS doesn't scale as $\frac{1}{\sqrt{n_p}}$ (for 100 incident photons we should have $TTS = \frac{3.5}{\sqrt{100}} = 350ps$). This is obviously due to the fact that photoelectrons follow different pahts between the photocathode and the SIPM. Anyway this TTS can be reduced enhancing the HV.
So we evaluated the difference between one path and another. To perform this measure we used a collimated laser beam that sent an average 100 photons per pulse close to the photocathode. We focused the beam once directly on SiEM and once on a point away from SiEM; in both cases we acquired Dtime@level with 10000 measurements runs.

[3]For a gaussian distribution

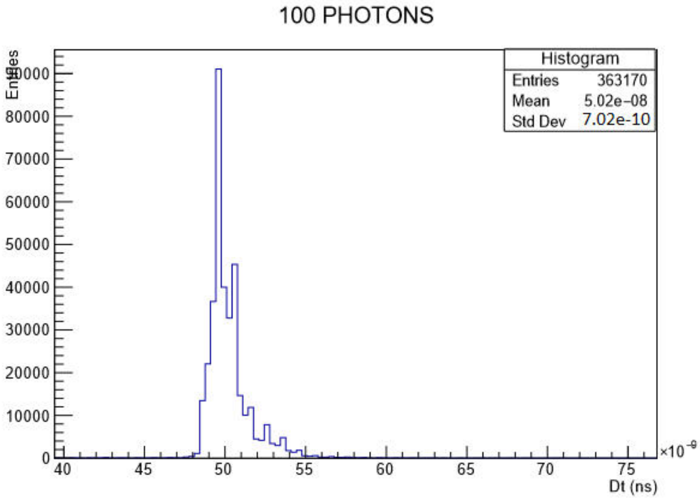

Figure 5.20: Gaussian distribution of the time intervals between the single electron signals and the laser pulses made by means of the data analysis tool Root for 100 photons per pulse. The little bulge on the right side of the distribution is due to afterpulses

The difference between one path and another will be given by the difference between the means of the two distributions (fig. 5.21):

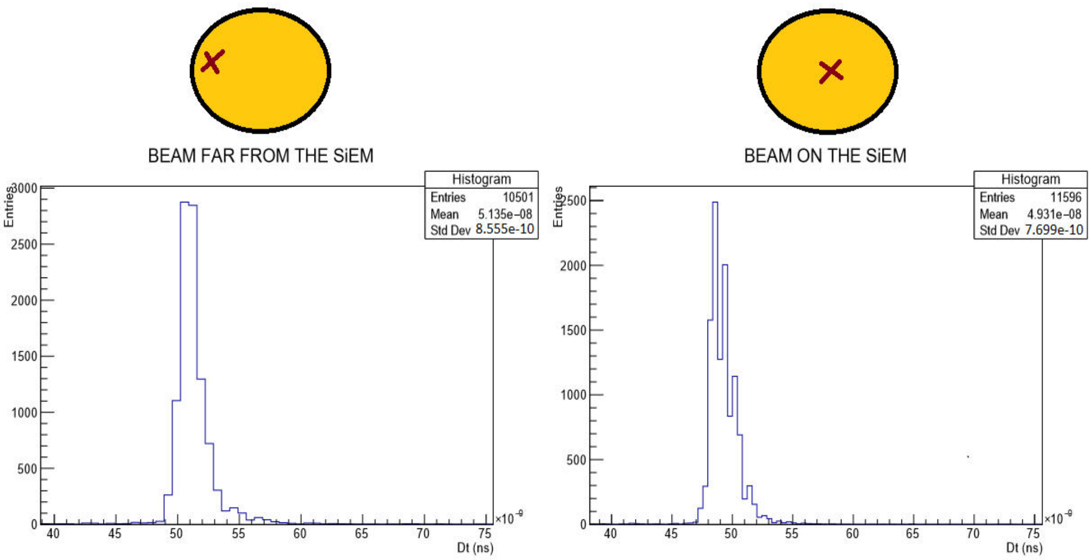

Figure 5.21: Gaussian distribution of the time intervals between the single electron signals and the laser pulses made by means of the data analysis tool Root in the two cases. The little bulge on the right side of the two distributions is due to afterpulses

From this analysis results:

$$Time\ Difference\ Between\ Paths = (1.7966 \pm 0.0003)ns \tag{5.7}$$

Since the differences between the paths of electrons which come from different points of the photocathode are on the order of a nanosecond, in these conditions the TTS can not be reduced to a value lower than the nanosecond.

5.8 Focusing

The capability of focusing uniformly photoelectrons over the SiEM surface is a crucial feature for the good operation of the VSiPMT.

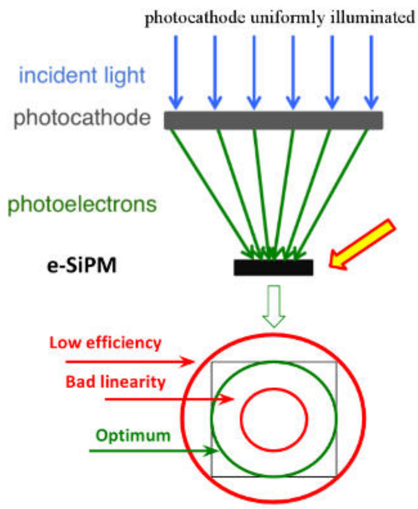

Figure 5.22: Focusing in a VSiPMT

The photocathode of the VSiPMT prototype has a circular shape. Therefore, taking into account the axial symmetry of the electric field generated by the focusing ring, an approximately circular photoelectron spot is reasonably expected.
Referring to figure 5.22, a too strong focusing makes the photoelectron spot smaller than the SiPM active surface. This solution is deleterious because a too squeezed photoelectron spot means that a fraction of the SiPM pixels is not involved, this therefore drastically reduces the linearity of the device.
However, a too weak focusing causes a photoelectron spot larger than the SiPM surface. This means that a fraction of the photoelectron is sistematically missed, thus implying a reduction of the photon detection efficiency of the device.
An optimal focusing condition is achieved if the photoelectron beam spot is perfectly inscribed in the SiPM square target. In this case, no more than the 85% of

the total number of cells of the SiEM can be fired. This is the configuration that exploits the maximum number of pixels leading to an optimized use of the device. To prove the focusing of our prototype, we have the targeted with a laser beam at maximum power available to ensure that the SiEM reached the saturation (fig. 5.23).

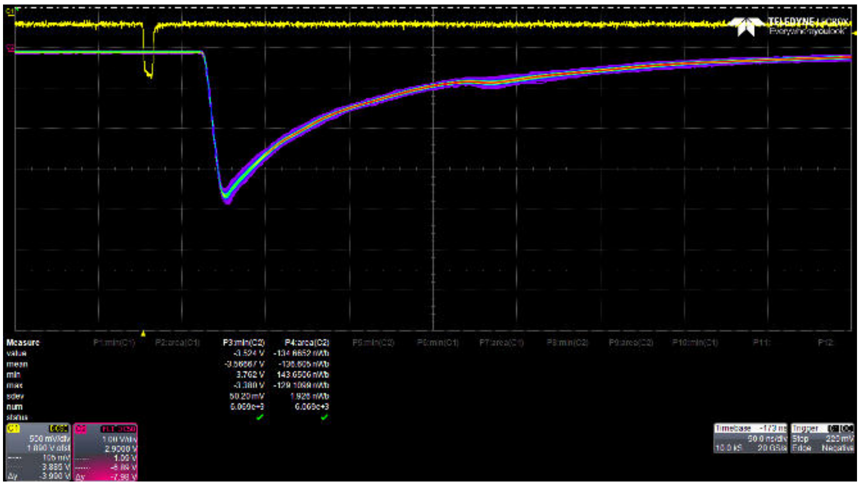

Figure 5.23: Saturated SiEM signal. By varying the laser power, above a certain threshold, the amplitude of this signal remains unchanged. This means that it has reached saturation

The maximum number of cells we fired was obtained by dividing the average value of the charge contained in the saturated signal to the charge contained in the single cell signal (these values have been acquired with their error), the result was 900 ± 15 . This means that the optimum solution for the focusing has not been reached. To have the optimum, we should have 700 fired cells, which correspond to a circular spot inscribed in the SiEM surface of 7.1 mm^2 area and 1.5 mm diameter (fig. 5.24).

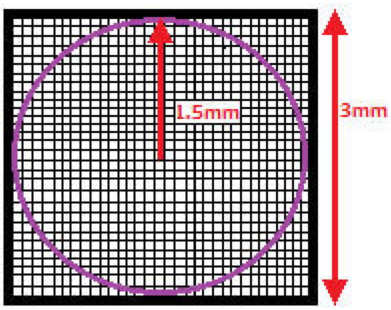

Figure 5.24: Optimum focusing in our VSiPMT prototype

In our case the spot contains the SiEM, so it is under-focused and we are in the low efficiency condition (fig. 5.25). This problem is probably linked to the low HV available (max 2kV), as explained in section 5.5. By solving this problem during the device assembly we expect an improvement of the focusing in the next prototype.

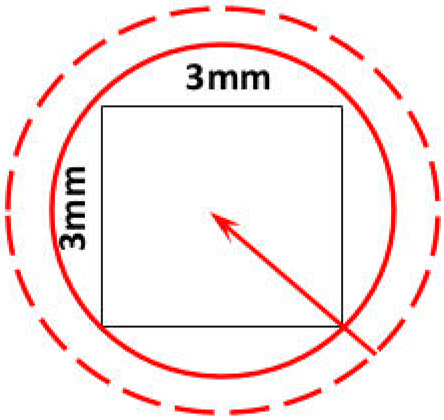

Figure 5.25: Actual focusing in our VSiPMT prototype. Radius of photoelectron focusing area circumsbribes the SiEM square shape

To make the focusing less complicated and ensure the total illumination of the SiEM, a solution would be to do round devices instead of square. Current technology allows to manufacture round SiPMs, this would also lead the further advantage of eliminating the thermal noise due to the unused cells in the corners.

5.9 Linearity And Dynamic Range

The dynamic range of a VSiPMT depends on the total number of cells of the SiEM, so what we said in section 3.2.3 about SiPM's linearity still holds: given the total number of available cells (N$_{cells}$) of the SiEM, the response of SiEMs (that is the number of fired cells (N$_{pe}$) as a function of the number of incident photons (N$_{ph}$) and of the PDE) is given by the following formula:

$$N_{pe}(N_{cells}, \lambda, V) = N_{cells} \cdot \left[1 - e^{\frac{-N_{ph} \cdot PDE(\lambda, V)}{N_{cells}}}\right]. \tag{5.8}$$

Another major contribution to the dynamic range of the VSiPMT is provided by the focusing (fig. 5.22) which, as seen in the previous section, has not reached the optimum.
Measurements of the dynamic range of the prototype have been performed in the

same conditions and modality described in section 3.2.3 for a number of incident photons that goes from a maximum of 28777 to a minimum of 195 usign various filters (fig. 5.26). The experimental points are plotted in figure 5.27.

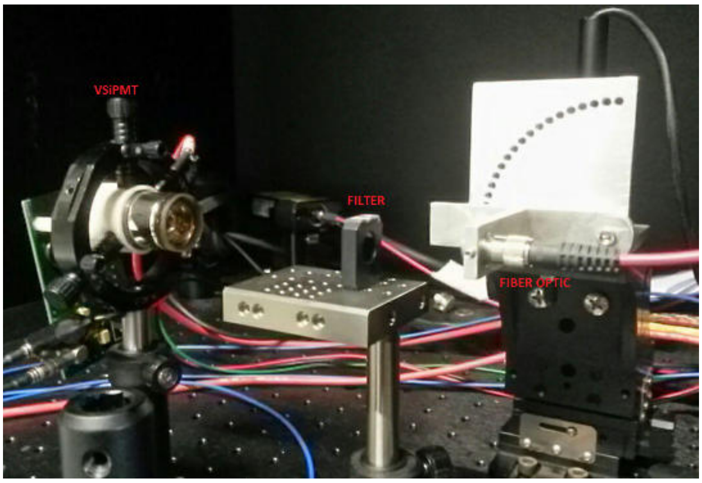

Figure 5.26: Experimental set up for dynamic range measurement

The graph in figure 5.27 shows the number of fired pixels versus the number of incident photons (so the VSiPMT response).

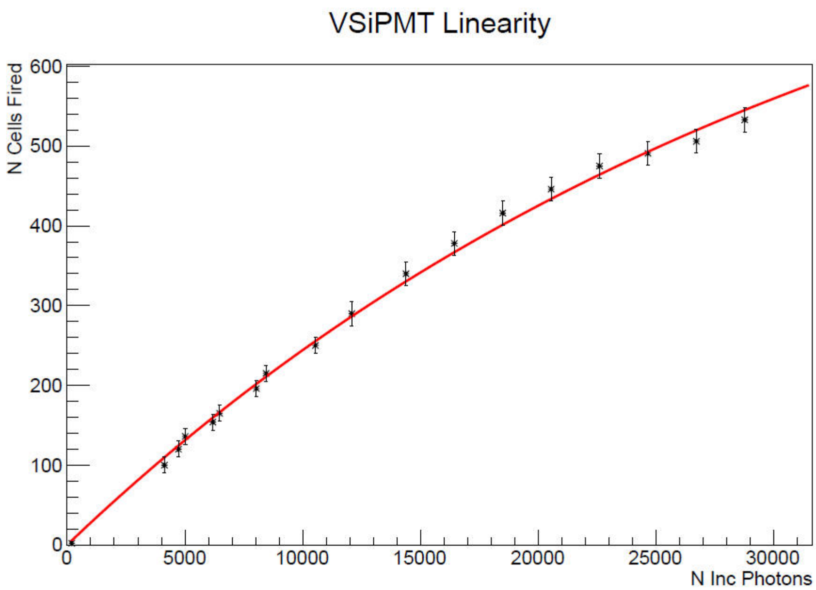

Figure 5.27: Number of fired pixels as a function of the number of incident photons for the VSiPMT prototype

The experimental data have been fitted with the following two parameters curve:

$$y = a \cdot \left(1 - e^{\frac{-b \cdot x}{a}}\right), \tag{5.9}$$

For $\sim$ 20000 incident photons the upper limit of the dynamic range has been reached, the response of the VSiPMT begins to deviate from linearity and the saturation occurs.
The two parameters a and b provide the total number of the SiEM cells and total photodetection efficiency of the device:

$$a = N_{cells} = 945 \pm 100 \tag{5.10}$$

$$b = PDE = (2.77 \pm 0.12)\% \tag{5.11}$$

The value of N_{cells} (the parameter a) is, within the error, equal to the total number of the SiEM's cells (900 as discussed above) as we expected. Since the total PDE results to be $\sim$ 2% from the previous discussion, we see that the value of the parameter b is in agreement with the same value which comes out independently from other considerations.

Chapter 6

Conclusions and Perspects

In this thesis we performed a detailed characterization of the latest generation SiPMs in order to describe the current semiconductor detector's technology state of art with the final aim to choose the better core device for the realization of the next VSiPMT prototype. Moreover a further improvement has been proposed with respect to the SiPMs characterized here.
Then we performed a temperature characterization of a non so recent generation SiPM in order to test the C11204-01 high-voltage power supply which is the solution to SiPMs gain reduction with increasing temperature proposed by Hamamatsu. In the future it might be interesting to perform a similar study on the VSiPMT to achieve an amplification circuit which also includes the C11204-01 high-voltage power supply; the aim should be to realize a even more compact device with even less power consumption, since the C11204-01 requires just 5V power supply to generate the voltage needed to supply the SiPM inside the VSiPMT (50 to 90 V).
Finally we performed an extensive characterization of the latest usable VSiPMT prototype. This analysis provided first-rate results: the VSiPMT offers very attractive features and unprecedented performances, definitely superior to every other photodetector of the same sensitive surface.
Negligible power cosumption, excellent SPE resolution, easy low-voltage-based stability, very good time performances, high gain and wide dynamic range are among the most outstanding achievements, counterbalanced by few drawbacks like a still high dark noise, a not so high PDE and a focus that has not yet reached the optimum condition. However these are easily upgradeable design features which certainly will not appear again in the next prototype
In this thesis are presented, for the first time ever, the results of tests performed on a novel technology manufactured by the world's greatest photodetector company. A device which represents the truly usable realization of an idea born ten years ago, with a sketch on a piece of paper.

The development of this new detector has opened a new frontier in the field of astroparticle physics, a field dominated for more than one century by PMT technology. Even if new materials, new layouts and new solutions led to an incredible improvement of PMT performances, this technology suffers of some intrinsic drawbacks that strongly affect its performances, limiting its current field of application and even strongly compromising its secular leading role.
By now the world of experimental physics is ready for the development of alternative solutions to PMTs. Indeed, in the last decades, the strong development of silicon devices have boosted detector's technology towards a new generation of solid-state photodetectors, passing through PIN photodiodes (with no internal gain), Avalanche PhotoDiodes (APDs, operating in linear region with internal gains of up to a few hundreds) and avalanche photodiodes in Geiger-Mode (GAPDs or SiPMs, operating in Geiger regime with gains ranging between 10^5 and 10^6).
These devices exhibit important advantages over PMTs, namely higher quantum efficiency, lower operation voltages (and hence strongly reduced power consumption), weak sensitivity to external magnetic fields, robustness and compactness.
In particular, the SiPM technology, introduced in the first years of 21st century, has known a whirling evolution, that led current devices to reach an extremely challenging level of performances, in terms of quantum efficiency, gain, photon counting capabilities and time response. However, the small sensitive surface achieved by the current generation of SiPMs (due mainly to thermal dark currents and Silicon wafer costs) sets a strong limit to their possible field of application, making them weak photodetector candidates for most of the next generation astroparticle physics experiments based on scintillation phenomena, Cherenkov or fluorescence radiation.
This is the framework in which the concept of VSiPMT was born. This solution is expected to bring several important advantages in the comparison with standard PMTs even because, while the PMT technology is not further improved, semiconductor's technology is going through its golden age. The real impact of semiconductors on everyday people's lives is huge, so research and development in this area proceeds at a very high pace making potentially infinite improvements, which will involve the detectors that are based on this technology. Indeed, since Hamamatsu already showed a great interest in the VSiPMT project and the related R&D path, could be interesting to arrange a consortium of european companies (PMT, SiPM and getters producers) to start a mass production for the next generation of astroparticle physics experiments both in space and on heart.
In conclusion, from the results that we have gathered, it is clear that this invention is expected to represent a real breakthrough in the field of photodetectors, destined to revolutionize several research fileds (such as astroparticle physics, medical applications, material science and environment applications) and to change our

way of seeing the world, which now appears with a higher resolution.

Appendix A

Lambertian Distribution

Lambertian reflectance is the property that defines an ideal "matte" or diffusely reflecting surface. The apparent brightness of a Lambertian surface to an observer is the same regardless of the observer's angle of view. More technically, the surface's luminance is isotropic, and the luminous intensity obeys Lambert's cosine law: the radiant intensity or luminous intensity observed from an ideal diffusely reflecting surface or ideal diffuse radiator is directly proportional to the cosine of the angle θ between the direction of the incident light and the surface normal [40]. The situation for a Lambertian surface (emitting or scattering) is illustrated in figure A.1.

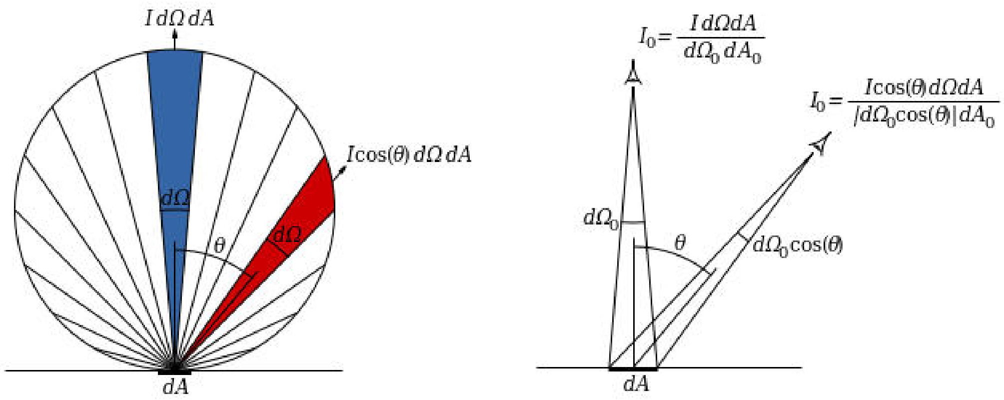

Figure A.1: Left: Emission rate (photons/s) in a normal and off-normal direction. The number of photons/sec directed into any wedge is proportional to the area of the wedge. Right: Observed intensity ($\frac{photons}{s \cdot cm^2 \cdot sr}$) for a normal and off-normal observer; dA_0 is the area of the observing aperture and $d\Omega$ is the solid angle subtended by the aperture from the viewpoint of the emitting area element.

We will think in terms of photons rather than energy or luminous energy. The

wedges in the circle each represent an equal angle dΩ, and for a Lambertian surface, the number of photons per second emitted into each wedge is proportional to the area of the wedge.
It can be seen that the length of each wedge is the product of the diameter of the circle and $cos(\theta)$. It can also be seen that the maximum rate of photon emission per unit solid angle is along the normal and diminishes to zero for $\theta = 90°$. In mathematical terms, the radiance along the normal is $I \cdot \frac{photons}{s \cdot cm^2 \cdot sr}$ and the number of photons per second emitted into the vertical wedge is $I \cdot d\Omega \cdot dA$. The number of photons per second emitted into the wedge at angle θ is $I \cdot cos(\theta) \cdot d\Omega \cdot dA$.
Figure A.1 (right) represents what an observer sees. The observer directly above the area element will be seeing the scene through an aperture of area dA_0 and the area element dA will subtend a (solid) angle of dΩ_0. We can assume without loss of generality that the aperture happens to subtend solid angle dΩ when "viewed" from the emitting area element. This normal observer will then be recording $I \cdot d\Omega dA$ photons per second and so will be measuring a radiance of:

$$I_0 = \frac{I \cdot d\Omega \cdot dA}{d\Omega_0 \cdot dA_0} \cdot \frac{photons}{s \cdot cm^2 \cdot sr}. \tag{A.1}$$

The observer at angle θ to the normal will be seeing the scene through the same aperture of area dA_0 and the area element dA will subtend a (solid) angle of $d\Omega_0 \cdot cos(\theta)$. This observer will be recording $I \cdot cos(\theta) \cdot d\Omega \cdot dA$ photons per second, and so will be measuring a radiance of:

$$I_0 = \frac{I \cdot cos(\theta) \cdot d\Omega \cdot dA}{d\Omega_0 \cdot cos(\theta) \cdot dA_0} = \frac{I \cdot d\Omega \cdot dA}{d\Omega_0 \cdot dA_0} \cdot \frac{photons}{s \cdot cm^2 \cdot sr}, \tag{A.2}$$

which is the same as the normal observer.

Appendix B

Detection Efficiency of the Previous VSiPMT Prototypes EB-MPPC050 (ZJ5025) and EB-MPPC100 (ZJ4991)

The fill factors of the SiPMs used for the ZJ5025 and the ZJ4991 prototypes are 61% and 78%, respectively, and the quantum efficiency of the photocathode is 38% at $\lambda = 407$ nm. Taking into account these values, the expected PDE for the two prototypes are $\mathrm{PDE}_{ZJ5025} = 23\%$ and $\mathrm{PDE}_{ZJ4991} = 30\%$. The PDE with respect to the high voltage supplied to the photocathode has been measured with the same procedure described above and its behaviour is shown in figure B.1.
PDE of the device becomes stable around $\sim$3 kV , with a plateau till $\sim$ 5 kV . The operating point for the high-voltage supply has been fixed to -3.2 kV , corresponding to $\sim$ 23% PDE value, as we expected. Even lower operating points can be achieved by simply reducing the SiO_2 layer of the SiEM. In this case the total efficiency at the plateau (where the trigger efficiency is effectively 1) has been calculated as follows:

$$\epsilon_{tot} = \epsilon_{PC} \cdot \epsilon_{geom} \cdot \epsilon_{trigger} = 0.38 \cdot 0.61 \cdot 1 = 0.23 \tag{B.1}$$

In these prototypes, unlike the EB-MPPC100 (XE2597) 1 INCH, the high voltage is able to drive photoelectrons to the SiEM surface and to give them the right energy to enter into the silicon bulk and produce the signal. Indeed if we calculate the detection efficiency out of the plateau, we obtain:

$$\epsilon_{tot} = \epsilon_{PC} \cdot \epsilon_{geom} \cdot \epsilon_{trigger} = 0.38 \cdot 0.61 \cdot 0.39 = 0.09 \tag{B.2}$$

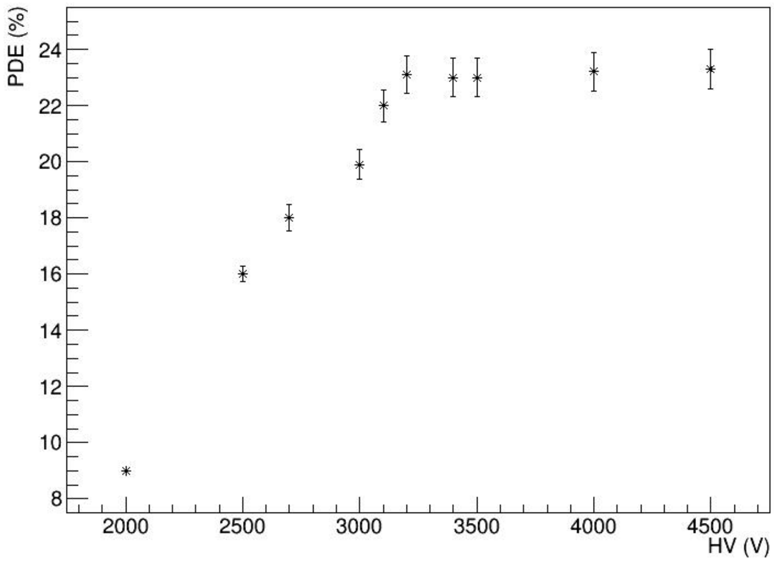

Figure B.1: Results of the photon detection efficiency test in function of the HV. The PDE errors are obtained by the propagation of the errors on N_{pe} and N_{ph}.

Bibliography

[1] A. Einstein, Ann. Phys. 17 (1905) 132

[2] D. Renker, Geiger-mode avalanche photodiodes, history, properties and problems, Nuclear Instruments and Methods in Physics Research A 567 (2006) 48-56

[3] Saleh B. E., Teich M. C. Semiconductor photon detectors. Fundamentals of Photonics, pages 644, 695, 2007

[4] Miller S. Ionization rates for holes and electrons in silicon. Physical Review, 105(4):1246, 1957

[5] K. Seeger, Semiconductor Physics, Springer-Verlag (1973)

[6] W. B. Burford III, H. Grey Verner, Semiconductor Junctions and Devices, McGraw-Hill (1965)

[7] S. O. Kasap, Optoelectronics and Photonics: Principles and Practices, Prentice-Hall (2001)

[8] J. Singh, Electronic and Optoelectronic Properties of Semiconductor Structures, Cambridge University Press (2003)

[9] J. Millman, Circuiti e Sistemi Microelettronici, Bollati Boringhieri (1985)

[10] R. A. Greiner, Semiconductor Devices and Applications, McGraw-Hill (1961)

[11] G. F. Knoll, Radiation Detection and Measurement (3 ed.), John Wiley and Sons (2000)

[12] W.R. Leo, Techniques for Nuclear and Particle Physics Experiments, Springer-Verlag (1987)

[13] K. G. McKay, Avalanche Breakdown in Silicon, Phys. Rev. 94, 877 (1954)

[14] R. J. McIntyre, Theory of Microplasma Instability in Silicon, J. Appl. Phys. 32, 983 (1961)

[15] U. Marini, B. Marconi, A. Puglisi, L. Rondoni, A. Vulpiani, Fluctuation-Dissipation: Response Theory in Statistical Physics, Physics Reports vol. 461, p. 111 (2008)

[16] Hamamatsu Photonics K., et al. Opto-semiconductor handbook

[17] Simon, Hermann (June 10, 2009), Hidden Champions of the Twenty-First Century: The Success Strategies of Unknown World Market Leaders, London: Springer Science, Business Media.

[18] Avalanche photodiode, a user guide, understanding avalanche photodiode for improving system performance

[19] McKay K., McAfee K. Electron multiplication in silicon and germanium. Physical Review, 1953.

[20] G. Barbarino, F. C. T. Barbato, et al., A new generation photodetector for astroparticle physics: The VSiPMT, Astroparticle Physics 67, July 2014

[21] Winston R., O'Gallagher J. Nonimaging concentrators (optics). In Meyers R. A., editor, Encyclopedia of Physical Science and Technology (Third Edition), pages 507 - 522. Academic Press, New York, third edition edition, 2003

[22] Piemonte C. Sipm technology at fbk. IPRD10, Siena, 2010.

[23] BARBARINO G. Single-photons count device based on photocathode and geiger solid-state technology for the multiplication of photoelectrons, January 15 2015

[24] Barbarino G., De Asmundis R., De Rosa G., Fiorillo G., Gallo V., Russo S., A new high-gain vacuum photomultiplier based upon the amplification of a geiger-mode p-n junction. Nuclear Instruments and Methods in Physics Research Section A: Accelerators, Spectrometers, Detectors and Associated Equipment, 594(3): 326-331, 2008

[25] Sommer A. H. Brief history of photoemissive materials. In SPIE's 1993 International Symposium on Optics, Imaging, and Instrumentation, pages 2-17. International Society for Optics and Photonics, 1993

[26] Spicer W. E., Herrera-Gomez A. Modern theory and applications of photocathodes. In SPIE's 1993 International Symposium on Optics, Imaging, and Instrumentation, pages 18-35. International Society for Optics and Photonics, 1993

[27] Spicer W. Negative affinity 3-5 photocathodes: Their physics and technology. Applied physics, 12(2):115-30, 1977

[28] Sommer A. H. Photoemissive materials. preperation, properties and uses. Huntington: Krieger, 1980, 1, 1980

[29] G. Barbarino, F. C. T. Barbato et al: Vacuum Silicon PhotoMultipliers: recent developments. Nuclear Instruments and Methods in Physics Research Section A: Accelerators, Spectrometers, Detectors and Associated Equipment, 718: 582-583, 2013

[30] C. Piemonte, A. Ferri, A. Gola, A. Picciotto, T. Pro, N. Serra, A. Tarolli, N. Zorzi, Development of an automatic procedure for the characterization of silicon photomultipliers, Conference Record of NSS/MIC 2012, IEEE, 2012

[31] S. Sze and K. Ng, Physics of Semiconductor Devices, 3rd ed. Hoboken, NJ: Wiley-Interscience, 2006

[32] N. Serra, A. Ferri, A. Gola, T. Pro, A. Tarolli, N. Zorzi, C. Piemonte, Characterization of new FBK SiPM technology for visible light detection, in "JOURNAL OF INSTRUMENTATION", vol. 8, n. P03019, 2013

[33] Hamamatsu SiPM Multi Pixel Photon Counters S10931-100P series datasheet, september 2010

[34] C. Piemonte, A. Ferri, A. Gola, T. Pro, N. Serra, A. Tarolli, N. Zorzi, Characterization of the First FBK HighDensity Cell Silicon Photomultiplier Technology, in "IEEE TRANSACTIONS ON ELECTRON DEVICES", vol. 60, n. 8 2013

[35] M. Grodzicka, Member, IEEE, M. Moszynski, Fellow, IEEE, T. Szczesniak, Member, IEEE, M. Szawlowski, D. Wolski , K. Lesniewski, Effective dead time of APD cells of SiPM IEEE Nuclear Science Symposium Conference Record, 2011

[36] M.Grodzicka, M. Moszynski, T. Szczesniak, M. Szawlowski, D. Wolski, J. Baszak. "2x2 SiPM Arrays in Gamma spectrometry with CsI(Tl), LSO:Ce(Ca), LaBr3, BGO" in IEEE Nuclear Science Symp. Conf. Rec., Valencia, CF, Oct. 2011

[37] N. Akil, S. E. Kerns, D. V. Kerns, Jr., A. Hoffmann, and Jean-Pierre Charles, "A Multimechanism Model for Photon Generation by Silicon Junctions in Avalanche Breakdown" IEEE Trans. on Electron Devices vol. 46, No. 5 (1999)

[38] Power Supply module for SiPM C11204-01, Operation Manual

[39] Power Supply module for SiPM C11204-01, Command Reference

[40] Modern Optical Engineering, Warren J. Smith, McGraw-Hill

[41] Barbarino G. et al., Proof of feasibility of the Vacuum Silicon PhotoMultiplier Tube (VSiPMT), Journal of Instrumentation, Volume 8, Issue 04, article id. P04021 (2013)

[42] Barbarino G., Barbato F. C. T. et al., A new generation photodetector for astroparticle physics: The VSiPMT, Astroparticle Physics, Volume 67, p. 18-25, 2015

[43] Engstrom R. et al. Rca photomultiplier manual. RCA Electronic Components, Harrison, NJ, 1970

Ringraziamenti

Quando mi sono laureata alla triennale avrei dovuto scrivere i ringraziamenti nella tesi ma non l'ho fatto, perché ero immatura, perché ero delusa... Ho sbagliato.
C'erano tantissime persone che avrebbero meritato di essere rigraziate, perché ognuna di loro ha contribuito a suo modo alla mia crescita come persona e come scienziato. Stavolta non commetteró lo stesso errore, a queste persone dedico l'ultimo capitolo della mia tesi magistrale, il culmine di un perscorso durato anni, che mi ha reso la persona che sono.
Il primo e piú importante ringraziamento va fatto al Professor Barbarino, che mi ha accolto nel suo gruppo di ricerca e mi ha coinvolto nel suo progetto piú bello, che ha sempre creduto in me dandomi la possibilitá di confrontarmi con la reale hard research e che mi ha gratificato con la sua stima e la sua fiducia.
Ringrazio la Dottoressa Barbato, Felicia, che é stata dal primo momento il mio punto di riferimento, oltre che un'amica e un supporto nei momenti di difficoltá. Senza di lei non sarei stata in grado nemmeno di mettere piede in un laboratorio.
Ringrazio Antonio (Vanzanella), Nicola e Marco per la loro squisita disponibilitá e validissima competenza elettronica. Il successo nella stesura di questa tesi é in grossa parte anche merito loro.
Ringrazio inoltre il Professor Guarino per i suoi consigli, il Dottor de Asmundis per le consulenze LabView, il Dottor Di Capua, il Professor Campajola, la Dottoressa De Rosa, il Dottor Mollo e il Dottor Vivolo per l'aiuto che mi hanno dato.
Un percorso come questo non si esaurisce nel solo lavoro di tesi. La tesi é solo l'ultimo di una serie di ostacoli che ognuno di noi deve superare per crescere. É impensabile affrontare queste difficoltá da soli, per cui i miei sentiti ringraziamenti vanno a coloro che mi hanno accompagnato nel mio percorso e che mi hanno aiutato a superarle, a coloro che hanno gioito con me dei miei successi, che mi hanno incoraggiato nei miei fallimenti, che sono stati in ansia per me quando dovevo affrontare prove difficili e che ci sono sempre stati.
A mia madre e mio padre, che con i loro sacrifici mi hanno dato la possibilitá di arrivare fino a questo punto, a mio fratello Giovanni e a Nunzia, che mi hanno dato il loro sostegno incondizionato in ogni momento e a mia sorella Ludovica, per tutti gli abbraccini, che non sempre ho ricambiato. Il conforto delle nostre chiacchiere

a tavola mi ha dato spesso la forza di andare avanti e superare anche i momenti piú bui.
A nonno Umberto e nonna Maria, che mi hanno insegnato la dedizione al lavoro e la tenacia, le due qualitá su cui ho basato il mio intero percorso universitario.
A Italo, Rosaria, Diego ed Emanuela che mi hanno accolta in casa loro con calore, e mi amano come un membro della famiglia.
Al mio Maestro Sergio e alle mie ballerine Maria, MariaPia, Francesca e Diana, perché senza di voi e senza la danza i problemi sarebbero sembrati piú grandi e la vita piú triste.
L'universitá é una fase transitoria della vita, una fase che si esaurisce in fretta, ma alcuni dei legami che si creano in questo frangente sono destinati a durare. Un ringraziamento affettuoso va quindi ai miei colleghi, che hanno visto da vicino la mia evoluzione e mi hanno dimostrato in molte occasioni il bene che mi vogliono.
A Giulia, per essere, senza saperlo, un esempio di grande forza per me; ad Anna, per essermi stata vicina in un momento molto delicato; a quella pazza della Fiore, per aver messo le mani nel ciaccio insieme a me; a Fabio (Mele) per la nostra gag della finestra; a Federica, per aver condiviso con me l'ansia da Santorelli; a Maria per tutte le nostre chiacchierate da corridoio; a Davide, perché senza il suo aiuto un intero capitolo di questa tesi non sarebbe stato scritto; a Mario, che ha placato la mia ansia interrogandomi prima di svariati esami, e a Vincenzo che cosí si é fatto una cultura di elettronica; a Mariano, a cui chiederó senza dubbio di organizzare il mio matrimonio; a Luca (Buonocore), per tutto l'affetto che mi ha sempre dimostrato; a Fabio (Formisello) e Giovanni, per quell'epica maratona del Signore degli Anelli, per il Jazz e per tutti i discorsi da ora del té; a Luca (Tortorelli), per quell'indimenticabile mattinata all'Osservatorio di Capodimonte; a Martina e Carmen, le mie particellari preferite; a Giorgio, Daniele, Felice e Mauro, per tutti i discorsi da ora di pranzo (quelli seri e quelli meno seri); a Fiammetta, Pierpaolo, Silvia, Lollo e Antonio (Bellotta), per tutti i consigli e il sostegno che non mi hanno mai fatto mancare, anche a distanza; al Principe, per tutte le risate, le cene messicane, i ribaltamenti e i giovedí misogini; a Sandrone, per essere sempre e comunque il mio migliore amico.
Dulcis in fundo, il mio ringraziamento piú vivo va ad una delle persone piú straordinarie che abbia avuto la fortuna di incontrare, alla persona che ha dato il maggiore contributo alla mia carriera, alla persona che ho scelto come compagno di vita.
A Marco, perché da quando ci sei tu io non mi sento mai sola; perché mi hai incoraggiato fino a farmi prendere coscienza delle mie reali potenzialitá; per tutto l'aiuto e il supporto concreto che mi hai dato, senza il quale non avrei fatto una carriera magistrale cosí brillante; perché hai reso la mia vita migliore.